

**MATHEMATICAL MODELING AND STOCHASTIC SIMULATION OF
SOFT MATERIALS**

by

Yun Zeng

A dissertation submitted to the Faculty of the University of Delaware in partial fulfillment of the requirements for the degree of Doctor of Philosophy in Applied Mathematics

Fall 2014

© 2014 Yun Zeng
All Rights Reserved

UMI Number: 3685163

All rights reserved

INFORMATION TO ALL USERS

The quality of this reproduction is dependent upon the quality of the copy submitted.

In the unlikely event that the author did not send a complete manuscript and there are missing pages, these will be noted. Also, if material had to be removed, a note will indicate the deletion.



UMI 3685163

Published by ProQuest LLC (2015). Copyright in the Dissertation held by the Author.

Microform Edition © ProQuest LLC.

All rights reserved. This work is protected against unauthorized copying under Title 17, United States Code



ProQuest LLC.
789 East Eisenhower Parkway
P.O. Box 1346
Ann Arbor, MI 48106 - 1346

**MATHEMATICAL MODELING AND STOCHASTIC SIMULATION OF
SOFT MATERIALS**

by

Yun Zeng

Approved: _____
John Pelesko, Ph.D.
Chair of the Department of Mathematical Sciences

Approved: _____
George H. Watson, Ph.D.
Dean of the College of Arts & Sciences

Approved: _____
James G. Richards, Ph.D.
Vice Provost for Graduate and Professional Education

I certify that I have read this dissertation and that in my opinion it meets the academic and professional standard required by the University as a dissertation for the degree of Doctor of Philosophy.

Signed: _____

L. Pamela Cook, Ph.D.
Professor in charge of dissertation

I certify that I have read this dissertation and that in my opinion it meets the academic and professional standard required by the University as a dissertation for the degree of Doctor of Philosophy.

Signed: _____

Richard Braun, Ph.D.
Member of dissertation committee

I certify that I have read this dissertation and that in my opinion it meets the academic and professional standard required by the University as a dissertation for the degree of Doctor of Philosophy.

Signed: _____

Petr Plechac, Ph.D.
Member of dissertation committee

I certify that I have read this dissertation and that in my opinion it meets the academic and professional standard required by the University as a dissertation for the degree of Doctor of Philosophy.

Signed: _____

Lin Zhou, Ph.D.
Member of dissertation committee

ACKNOWLEDGEMENTS

I would like to express the deepest appreciation to my committee chair, Professor Cook, who is my mentor and dear friend. She continually inspired me to tackle the challenges and supported me in every way. Without her guidance and persistent help this dissertation would not have been possible.

I would like to thank my committee members, Professor Braun, Professor Plechac and Professor Zhou, for providing truthful and illuminating comments on my dissertation.

My sincere thanks also goes to Professor Pelesko for offering me the summer research opportunity in his group and leading me working on fluid dynamics projects.

I would like to thank Professor McKinley for providing insights that helped me improve my research.

I am indebted to my many colleagues and friends, for working together through difficult times and for all the fun we have had in the last five years.

I would also like to express my gratitude to Deborah See for all her help.

Last but not the least, I would like to thank my parents and brother for their enormous support and confidence in me throughout all my studies at University of Delaware.

TABLE OF CONTENTS

LIST OF FIGURES	ix
ABSTRACT	xix
 Chapter	
1 INTRODUCTION	1
1.1 Soft Materials	2
1.2 General Experimental Results	3
1.3 Review of Theoretical Approaches	5
1.4 Our Approach	6
2 CONSTITUTIVE MODELING	8
2.1 Geometry	8
2.2 Stress Tensor for Shear Flows	9
2.3 Shear Flow Material Functions	9
2.3.1 Small-Amplitude Oscillatory Shear (SAOS)	9
2.3.2 Step Strain Experiment	10
2.3.3 Start-up Followed by Cessation of Steady Shear Flow	11
2.4 Constitutive Modeling	11
2.4.1 Basic Fluid Flow Governing Equations	12
2.4.2 Upper-Convected Maxwell (UCM) Model	13
2.4.3 Giesekus Model	14
2.4.4 Vasquez-Cook-McKinley (VCM) Model	15

3	GENERAL MODELS FOR DESCRIBING NON-EXPONENTIAL STRESS RELAXATION	19
3.1	Fractional Calculus	20
3.1.1	Definition	20
3.1.2	General Properties	21
3.1.3	Techniques in the Fractional Calculus	21
3.2	Fractional Constitutive Models	22
3.2.1	Scott-Blair Model	22
3.2.2	Fractional Maxwell Model	22
3.2.3	Generalized Tensorial Fractional Maxwell Model	25
3.3	Cates Reptation Model	27
3.3.1	Kinetics of Breaking and Recombination	28
3.3.2	Dynamics of Stress Relaxation	29
3.3.2.1	Pure Reptation	30
3.3.2.2	Reptation and Kinetics of Breakage and Recombination	32
4	1-D FRACTIONAL KINETICS SIMULATED BY CONTINUOUS TIME RANDOM WALK (CTRW) AND SUBORDINATION	35
4.1	Anomalous Diffusion	36
4.2	Fractional Diffusion with/without External Velocity or Force Fields	36
4.3	From Continuous Time Random Walk to Fractional Diffusion Equation	40
4.4	Monte Carlo Simulation of CTRW	41
4.4.1	Standard Random Walks	43
4.4.2	CTRW with Infinite Mean Waiting Time	43
4.4.3	Galilean Invariant Case	46
4.4.4	Non-Galilean Invariant Case	49
4.5	Subordination of Fractional Fokker-Planck Dynamics	51
4.5.1	Subordination Simulation for Fractional Diffusion Equation	52
4.5.2	Subordination Simulation for Fractional Diffusion-Advection Equation - Non-Galilean Invariant Case	53

4.5.3	Subordination Simulation for Fractional Fokker-Planck Equation	57
4.6	Summary of Simulations Using CTRW and the Subordination Method	58
5	TRANSIENT NETWORK MODELS	61
5.1	Transient Network Model with Topology	62
5.1.1	Model Description	62
5.1.2	Simulation Results	65
5.2	Dumbbell Model	67
5.2.1	Model Description	67
5.2.2	Analytical Form of the Stress Tensor for the Dumbbell Model	68
5.2.3	Simulation Results	69
5.2.3.1	Equilibrium	69
5.2.3.2	Start-up and Cessation of Shear Flow	70
5.3	Lodge Network Model	71
5.3.1	Model Description	71
5.3.2	Analytical Form of the Stress Tensor for the Lodge Network Model	72
5.4	Hybrid Lodge Network Model	73
5.4.1	Model Description	73
5.4.2	Rheological Equation for Stress Tensor	74
5.4.3	Simulation Results	75
5.4.3.1	Inception and Cessation of Steady Shear Flow	75
5.4.3.2	Step Strain Relaxation	76
5.5	Fractal Lodge Network Model	77
5.5.1	Model Description	77
5.5.2	Simulation Results	79
5.5.2.1	Inception and Cessation of Steady Shear Flow	79
5.5.2.2	Step Strain Relaxation	82

5.5.2.3	Small-Amplitude Oscillatory Shear	83
5.6	Fractal Hybrid Lodge Network Model	85
5.6.1	Model Description	85
5.6.2	Simulation Results	87
5.6.2.1	Equilibrium	87
5.6.2.2	Step Strain Relaxation	88
5.6.2.3	Inception and Cessation of Steady Shear Flow	90
5.7	Two-species Network Model with Fractal Breakage and Recombination Processes	91
5.7.1	Model Description	91
5.7.2	Simulation Results	93
5.7.2.1	Start-up and Cessation of the Steady-shear Flow . .	93
5.7.2.2	Step Strain Experiment	95
5.8	Two-species Network Model with Subordinated Langevin Process . .	98
5.8.1	Model Description	98
5.8.2	Simulation Results	99
5.8.2.1	Inception and Cessation of Steady Shear Flow	100
5.8.2.2	Step Strain Relaxation	100
6	CONCLUSION	102
	BIBLIOGRAPHY	107
	Appendix	
	REPRINT PERMISSION LETTERS	110

LIST OF FIGURES

1.1	Left: Schematic of a surfactant molecule with a hydrophobic tail and a hydrophilic head. Middle: Schematic of a cylindrical shaped wormlike micelle formed by surfactants hiding their tails from water and their head groups forming an outer shell. Right: Schematic of an entangled network of wormlike micellar chains scales.	2
1.2	The storage modulus G' (<i>red/solid line</i>), and loss modulus G'' (<i>blue/dashed line</i>), for a viscoelastic material as functions of frequency ω in small-amplitude oscillatory shear (SAOS).	3
1.3	Dynamic frequency experiment on a sample containing 50mM concentration of the surfactant erucyl dimethyl amidopropyl betaine (EDAB) at different temperatures [28]. Reproduced from [28] with permission of The Royal Society of Chemistry.	5
2.1	Steady simple shear flow; the top plate moves with a constant velocity V , the bottom plate is fixed. For a Newtonian fluid, the velocity distribution between the plates is linear.	8
2.2	A spring and a dashpot connected in series	13
2.3	Long species A can break to form two shorter species B and two shorter chains of species B can form a longer chain A.	15
2.4	Small-amplitude oscillatory results for a 100 mM/50 mM CpyCl/NaSal solution showing the storage (hollow symbols) and loss (filled symbols) moduli. The dashed lines correspond to fits from a single-mode upper-convected Maxwell model. The solid lines correspond to fits to the data from the VCM model showing the upturn in the loss modulus due to the second, non-Newtonian species [26]. Reprinted with permission from [26]. Copyright 2010, The Society of Rheology.	17

3.1	Stress relaxation after a step strain for the FMM (3.13), where $\lambda = 1$ and $\alpha = \beta = 0.3$ (red/circles). Initially, the decay asymptotes to a stretched-exponential function $G'(t') \sim \exp[-t'^{0.3}/(\lambda^{0.3}\Gamma(1.3))]$ (blue/dashed curve). For long times, the decay asymptotes to a power-law pattern $G'(t') \sim \Gamma(0.3) \sin(0.3\pi)t'^{-0.3}/(\pi\lambda^{0.3})$ (green/solid curve).	24
3.2	Left: $G'(\omega')$ (red/solid curve) and $G''(\omega')$ (blue/dashed curve) for $\alpha = \beta = 1$. Right: $G'(\omega')$ (red/circles) and $G''(\omega')$ (blue/squares) for $\alpha = \beta = 0.3$	25
3.3	The time evolution of τ'_{xy} (left) and τ'_{xx} (right) under simple shear flow with $\dot{\gamma}'_{yx} = 1$ for the tensorial fractional Maxwell model for $\alpha = 1, 0.9, 0.5$ and 0.3 , $\beta = 1$	27
3.4	In the pure reptation, the stress relaxation for a system of chains with exponential length distribution is simulated stochastically and compared with asymptotic studies. In the long-time limit, the stress decay asymptotes to a stretched-exponential function. The left figure plots $\tau(t)$ as a function of t and the right figure plots $\log((\tau(t)))$ as a function of t . Here, $A = 8/\pi^2(3D_0\pi)^{3/8}\sqrt{\pi/2}$, $B = 4/3(3D_0\pi^2)^{1/4}$, and $D_0 = 0.01$	31
3.5	Plot of $f(\zeta)$ as a function of ζ . For $\zeta \ll 1$, $f(\zeta) \sim \zeta^{1/2}$. For $\zeta \gg 1$, $f(\zeta)$ is close to a constant. Here $D_0 = 0.01$	33
3.6	Left: Stress relaxation $\tau(t)$ against t for the Cates reptation model, with $D_0 = 0.01$ for various ζ . Right: Stress relaxation $\tau(t)$ against scaled time $t/\lambda(\zeta)$ for the Cates reptation model, with $D_0 = 0.01$ for various ζ . For ζ small, the decay is almost purely exponential, whereas for large ζ , it is much more disperse. Right: We rescale the time axis by the system relaxation time $\lambda(\zeta)$ for each ζ and compare the relaxation dynamics.	33
4.1	The complementary cumulative distribution function (cdf) $W(t)$ sampled using (4.22) with $\beta = 0.6$ and $\gamma_t = 1$ (red/circles), as well as its approximations for $t \rightarrow 0$ (stretched-exponential, green/dashes) and $t \rightarrow \infty$ (power-law, blue/dashes).	42

- 4.2 Left: Sample paths of random walks with exponentially distributed waiting times generated using (4.22) for $\beta = 1$ and Gaussian jumps generated using (4.23). Right: Comparison of simulation results of the ensemble average of the particle mean-squared displacements (*blue/solid curve*) with equation $\langle x^2(t) \rangle = 2K_1t/\Gamma(2)$ formulated by taking the second moment of (4.2) (*red/circles*). Here $K_1 = 1$. The waiting times scale γ_t is set to 0.001, jump lengths are scaled by $\gamma_x = \gamma_t^{1/2}$ 44
- 4.3 Comparison of the histogram of $N = 2 \times 10^4$ particle positions from a Monte Carlo simulation of random walks with $\gamma_t = 0.001$ (*blue/solid curve*), with the exact form (4.7), with $K_1 = 1$ (*red/dashed curve*) at $t = 2$ 44
- 4.4 Left: Sample paths of CTRW with Mittag-Leffler distributed waiting times generated using (4.22) for $\beta = 0.6$ and Gaussian jumps generated using (4.23). Right: Comparison of simulation results of the ensemble average of the particle mean-squared displacements (*blue/solid curve*) with equation $\langle x^2(t) \rangle = 2K_\beta t^\beta/\Gamma(1 + \beta)$ formulated by taking the second moment of (4.2) (*red/circles*). Here $K_\beta = 1$. The waiting times scale γ_t is set to 0.001 and jump lengths are scaled by $\gamma_x = \gamma_t^{\beta/2}$ 45
- 4.5 Comparison of the histogram of $N = 2 \times 10^4$ particle positions from a Monte Carlo simulation of CTRW for $\gamma_t = 0.001$ (*blue/solid curve*) with the exact form (4.6) (*red/dashed curve*) for $\beta = 0.6$, $K_\beta = 1$, at $t = 2$. The cusp shape of the pdf is a distinctive feature of a CTRW. 45
- 4.6 Left: Sample paths of particles experiencing Brownian motion and external velocity, where the particles move deterministically under an external velocity field and diffuse with Gaussian jumps generated using (4.23) and exponentially distributed waiting times generated using (4.22) for $\beta = 1$. Here with a $v = 10$, the particles drift under the influence of the velocity field. Right: Comparison of simulation results of the ensemble average of the particle mean-squared displacements (*blue/solid curve*) with equation $\langle x^2(t) \rangle = 2K_1t/\Gamma(2) + v^2t^2$ formulated by taking the second moment of (4.10) (*red/circles*). Here $\beta = 1$, $v = 1$ and $K_1 = 1$. The waiting times scale γ_t is set to 0.01 and jump lengths are scaled by $\gamma_x = \gamma_t^{1/2}$ 47

4.7	Comparison of the histogram of particle positions experiencing Brownian motion and drift, for $\gamma_t = 0.01$ (<i>blue/solid curve</i>) with the exact form (4.9) (<i>red/dashed curve</i>) for $\beta = 1$, $K_1 = 1$, $v = 1$, at $t = 2$	48
4.8	Left: Sample trajectories of particles moving on a CTRW under the influence of an external velocity field in the Galilean invariant case. Here $\beta = 0.6$, $v = 10$. Right: Comparison of simulation results of the ensemble average of the particle mean-squared displacements (<i>blue/solid curve</i>) with equation $\langle x^2(t) \rangle = 2K_\beta t^\beta / \Gamma(1 + \beta) + v^2 t^2$ formulated by taking the second moment of (4.10) (<i>red/circles</i>). Here $\beta = 0.6$, $v = 1$ and $K_\beta = 1$. The waiting times scale γ_t is set to 0.01 and jump lengths are scaled by $\gamma_x = \gamma_t^{\beta/2}$	48
4.9	Plot of the histogram of particle positions experiencing subdiffusion and drift for the Galilean invariant case (<i>blue/solid curve</i>) for $\beta = 0.6$, $K_\beta = 1$, $v = 1$, $\gamma_t = 0.01$, at $t = 2$	49
4.10	Left: Sample trajectories of particles moving on a CTRW under the influence of an external velocity field in the non-Galilean invariant case. Here $\beta = 0.6$, $v = 10$. Right: Comparison of simulation results of the ensemble average of the particle mean-squared displacements (<i>blue/solid curve</i>) with equation $\langle x^2(t) \rangle = \frac{2K_\beta t^\beta}{\Gamma(1+\beta)} + \frac{2v^2 t^{2\beta}}{\Gamma(1+2\beta)}$ formulated by taking the second moment of (4.12) (<i>red/circles</i>). Here $\beta = 0.6$, $v = 1$, and $K_\beta = 1$. The waiting time scale γ_t is set to 0.01 and jump lengths are scaled by $\gamma_x = \gamma_t^{\beta/2}$	50
4.11	Plot of the histogram of the particle positions with a non-Galilean invariant velocity assumption from a simulation (<i>blue/solid curve</i>) for $\beta = 0.6$, $\gamma_t = 0.01$, $K_\beta = 1$, $v = 1$, at $t = 2$	50
4.12	A sample realization of the subordinated Langevin dynamics $X(S_t)$ (<i>blue/solid line</i>), the standard Langevin dynamics $X(\tau)$ (<i>red/dash-dot line</i>), and the inverse-time β -stable subordinator S_t (<i>green/dashed line</i>), for simulating the anomalous diffusion in the presence of a constant potential $V(x) = \text{const}$. Here $\beta = 0.6$, $K_1 = 1$	53

- 4.13 Left: The mean-squared displacement of an ensemble of the subordinated stochastic process $X(S_t)$ for describing anomalous diffusion with potential $V(x) = \text{const}$ (*blue/solid curve*) is compared with equation $\langle x^2(t) \rangle = 2K_\beta t^\beta / \Gamma(1 + \beta)$ formulated by taking the second moment of (4.2) (*red/dashed curve*). Right: Evolution in time of the pdf of 10^4 subordinated sample path $X(S_t)$ with a constant potential $V(x) = \text{const}$. Here $\beta = 0.6$, $K_1 = 1$ 54
- 4.14 A sample realization of the anomalous diffusion $X(S_t)$ (*blue/solid line*), the standard Langevin dynamics $X(\tau)$ (*red/dash-dot line*), and the inverse-time β -stable subordinator S_t (*green/dashed line*), in the presence of a linear potential $V(x) = -vx$. Here $v = 10$, $K_1 = 1$, and $\beta = 0.6$ 55
- 4.15 Left: The mean-squared displacement of an ensemble of the subordinated stochastic process $X(S_t)$ for describing anomalous diffusion with potential $V(x) = -vx$ (*blue/solid curve*) is compared with equation $\langle x^2(t) \rangle = \frac{2K_\beta t^\beta}{\Gamma(1+\beta)} + \frac{2v^2 t^{2\beta}}{\Gamma(1+2\beta)}$ formulated by taking the second moment of (4.12) (*red/dashed curve*). Right: Evolution in time of the pdf of 10^4 subordinated sample path $X(S_t)$ with a linear potential $V(x) = -vx$. Here $\beta = 0.6$, $K_1 = 1$ 55
- 4.16 Comparison of the mean-squared displacement of an ensemble by: simulation of particles moving on a CTRW under the influence of an external velocity field in the non-Galilean invariant case (*blue/solid curve*), simulation of the subordinated stochastic process $X(S_t)$ for describing anomalous diffusion with potential $V(x) = -vx$ (*red/dashed curve*), the equation $\langle x^2(t) \rangle = \frac{2K_\beta t^\beta}{\Gamma(1+\beta)} + \frac{2v^2 t^{2\beta}}{\Gamma(1+2\beta)}$ formulated by taking the second moment of (4.12) (*green/circles*), and the equation $\langle x^2(t) \rangle = \frac{2K_\beta t^\beta}{\Gamma(1+\beta)} + v^2 t^2$ formulated by taking the second moment of (4.10) (*magenta/squares*). Here $\beta = 0.6$, and $K_\beta = 1$ 56
- 4.17 A sample realization of the anomalous diffusion $X(S_t)$ (*blue/solid line*), the standard Langevin dynamics $X(\tau)$ (*red/dash-dot line*), and the inverse-time β -stable subordinator S_t (*green/dashed line*), in the presence of a parabolic potential $V(x) = \frac{1}{2}bx^2$. Here $\beta = 0.6$, $b = 1$, $K_1 = 1$ 57

4.18	Left: The mean-squared displacement of an ensemble of the subordinated stochastic process $X(S_t)$ for describing anomalous diffusion with potential $V(x) = -\frac{1}{2}bx^2$ (<i>blue/solid curve</i>) is compared with a power law $\langle x^2(t) \rangle = 2K_\beta t^\beta / \Gamma(1 + \beta)$ (the mean-squared displacement of particles with subdiffusion) (<i>red/dashed curve</i>). Right: Evolution in time of the pdf of 10^4 subordinated sample path $X(S_t)$ with a linear potential $V(x) = -\frac{1}{2}bx^2$. The time evolution of the pdf of particle positions slowly relaxes towards the Boltzmann distribution $\psi_{st}(x) = 1/\sqrt{2\pi} \exp(-bx^2/2)$ black/dashed line. Here $\beta = 0.6$, $b = 1$, $K_1 = 1$	58
5.1	A reversible cross-linked network formed by bead-spring dumbbells and sticky nodes following [7]. In this example, the sticky nodes capture a maximum of $f_{\max} = 4$ beads to form junction points. Each node has a finite lifetime. The lifetimes follow an exponential distribution with mean τ . Thus, the network reorganizes as time passes by.	63
5.2	Under steady-shear flow with $v_0 = 0$, $\dot{\gamma} = 1$, the shear stress and first normal stress of the van den Brule and Hoogerbrugge [7] system with $f_{\max} = 1$ grow as a function of time and eventually reach steady-state values $\sigma_{yx_{ss}} = 1$ (<i>blue/solid curve</i>) and $N_{1_{ss}} = 2$ (<i>red/dashed curve</i>).	66
5.3	A phenomenological network system with bead-spring dumbbells which can attach or detach [5].	67
5.4	Starting from a Gaussian distribution, the probability distribution of dumbbell lengths at equilibrium for the dumbbell model at various times $t = 0$ (<i>green/squares</i>), $t = 5$ (<i>magenta/circles</i>), $t = 10$ (<i>blue/triangles</i>). The pdfs are compared with the equilibrium distribution (5.12) (<i>red/solid curve</i>).	70
5.5	Stochastic simulation of the dumbbell model under shear flow with $\dot{\gamma} = 1$. Left: the probability distribution $P(Q , t)$ of all dumbbell lengths is plotted at various times $t = 0$ (<i>green/squares</i>), $t = 5$ (<i>magenta/circles</i>), $t = 10$ (<i>blue/triangles</i>). Right: The plot of the shear stress (<i>blue/solid curve</i>) and first normal stress difference (<i>red/dashed curve</i>) as a function of time. The imposed shear is turned off at $t = 30$ and the stress relaxes for $30 < t < 35$	71

5.6	Stochastic simulation of the hybrid Lodge network model with spring force and diffusion, under shear flow, with $\dot{\gamma} = 1$ for $0 < t < 10$, and $\dot{\gamma} = 0$ for $t > 10$. The plot is stress versus time for simulations with $\lambda = 0.1$ (<i>blue/solid curve</i>), $\lambda = 1$ (<i>red/dash-dot curve</i>) and $\lambda = 10$ (<i>green/dashed curve</i>) is compared.	75
5.7	Stress relaxation following a step strain for the hybrid Lodge network model with spring force and diffusion with parameters $\lambda = 0.1$ (<i>blue/solid curve</i>), $\lambda = 1$ (<i>red/dash-dot curve</i>) and $\lambda = 10$ (<i>green/dashed curve</i>). Here $\gamma_0 = 10, b = 100$	76
5.8	Left: The time evolution of the shear stress for the fractal Lodge network model after a constant shear rate $\dot{\gamma} = 1$ is imposed for $0 < t < 10$. The resultant stress growth for dumbbells with a Mittag-Leffler breakage/recombination processes for different α is compared. Right: The shear flow is turned off at $t = 10$. The stress relaxation is shown for simulations for different α , $0 < \alpha \leq 1$. The arrow points in the direction of increasing α values.	79
5.9	For stochastic simulation of the fractal Lodge network model with $\lambda_{Br} = 1$, the length distributions of network strands under steady shear flow for $\alpha = 1$ (<i>left</i>) and $\alpha = 0.3$ (<i>right</i>) at various times $t = 0, 5, 10$. Note the length distribution of dumbbell connector vectors is broader with $\alpha = 0.3$, in comparison with $\alpha = 1$	80
5.10	For stochastic simulation of the fractal Lodge network model with $\lambda_{Br} = 1$, the cumulative distribution $F(Q)$ of network strand lengths under steady shear flow for different α at $t = 10$. The arrow points in the direction of decreasing α values.	81
5.11	Stress evolution in time for the fractal Lodge network model after cessation of imposed shear at the various times $T_1 = 0.1$ (<i>blue/solid curve</i>), $T_1 = 1$, (<i>red/dashed curve</i>), and $T_1 = 10$ (<i>green/double dashed curve</i>). The stress relaxation of this fractal Lodge network model, can be rescaled to form a master curve. Here $\alpha = 0.6$ and $\lambda_{Br} = 1$	81
5.12	Left: Stress relaxation for the fractal Lodge network model following a step strain for parameters $\alpha = 0.3, \alpha = 0.6$ and $\alpha = 1$ with $\lambda_{Br} = 1, \gamma_0 = 10, b = 100$. Right: Stress relaxation following the same step strain for $\alpha = 0.6$ with $\lambda_{Br} = 1$ and $\lambda_{Br} = 10$. Both responses exhibit initial stretched-exponential behaviors for $t \ll \lambda_{Br}$ and then power-law patterns for $t \gg \lambda_{Br}$. Here, $A = 1, B = 1/\Gamma(\alpha + 1), C = \Gamma(\alpha) \sin(\alpha\pi)/\pi$	82

5.13	Storage modulus $G'(\omega)$ and loss modulus $G''(\omega)$ as a function of ω for different α and $\lambda_{Br} = 1$	84
5.14	Cole-Cole plot of the storage modulus G' and loss modulus G'' associated with the fractal Lodge network model simulated stochastically for $\alpha = 0.3, 0.6$, in comparison to the semicircular shape corresponding to the exponential relaxation pattern, $\alpha = 1$	85
5.15	The simulation of the mean-squared displacement of bead-spring dumbbell connectors in equilibrium for $\lambda = 0.1$ (<i>blue/solid curve</i>), $\lambda = 1$ (<i>red/dash-dot curve</i>) and $\lambda = 10$ (<i>green/dashed curve</i>) for the fractal hybrid Lodge network model with CTRW processes for both breaking/reforming and spring/Brownian forces. In the left figure, $\alpha = \beta = 1$. In the right figure, $\alpha = \beta = 0.6$	88
5.16	Stress relaxation following a step strain for parameters $\alpha = \beta = 1$ (<i>blue/solid curve</i>), and $\alpha = \beta = 0.6$ (<i>red/dashed curve</i>) for the fractal hybrid Lodge network model with CTRW processes for each of breakage/recombination and spring/Brownian force. Here, $\lambda = 1, \gamma_0 = 10, b = 100$	89
5.17	Stress relaxation following a step strain for the fractal hybrid Lodge network model with CTRW processes for each of breakage/recombination and spring/Brownian force. Left: $\alpha = \beta = 1$. The stress relaxation is exponential and the decay is compared for $\lambda = 0.1$ (<i>blue/solid curve</i>), $\lambda = 1$ (<i>red/dash-dot curve</i>), $\lambda = 10$ (<i>green/dashed curve</i>). Right: $\alpha = \beta = 0.6$. The stress relaxation is non-exponential and the decay is compared for $\lambda = 0.1$ (<i>blue/solid curve</i>), $\lambda = 1$ (<i>red/dash-dot curve</i>), $\lambda = 10$ (<i>green/dashed curve</i>).	89
5.18	Time evolution of the shear stress after a constant shear rate $\dot{\gamma} = 1$ is imposed for $0 < t < 10$ for the fractal hybrid Lodge network model with CTRW processes for each of breakage/recombination and spring and Brownian forces. The resultant stress growth for $\alpha = \beta = 1$ (<i>blue/solid curve</i>) and $\alpha = \beta = 0.6$ (<i>red/dashed curve</i>) are compared. The shear flow is turned off at $t = 10$, the stress relaxation is shown for simulations with $\alpha = \beta = 1$ and $\alpha = \beta = 0.6$	90

5.19	Simulations of shear stress evolution under start-up and cessation of shear flow with $\dot{\gamma} = 1$ for $0 < t < 200$ and $\dot{\gamma} = 0$ for $200 < t < 300$ for the two-species network model with fractal breakage/recombination processes. Here $\alpha = 1$. Left: The shear stress σ_{yx} grows as a function of time for $Z = 10$ (<i>blue/solid curve</i>) and $Z = 100$ (<i>red/dashed curve</i>). Right: The scaled shear stress $\sigma_{yx}/\sigma_{yx_{ss}}$ decays as a function of time for $Z = 10$ (<i>blue/solid curve</i>) and $Z = 100$ (<i>red/dashed curve</i>), where $\sigma_{yx_{ss}}$ is the steady-state value of the shear stress under start-up shear flow.	94
5.20	Simulations of shear stress evolution under start-up and cessation of shear flow with $\dot{\gamma} = 1$ for $0 < t < 200$ and $\dot{\gamma} = 0$ for $200 < t < 300$ for the two-species network model with fractal breakage/recombination processes. Here $\alpha = 0.6$. Left: The shear stress σ_{yx} grows as a function of time $Z = 10$ (<i>blue/solid curve</i>) and $Z = 100$ (<i>red/dashed curve</i>). Right: The scaled shear stress $\sigma_{yx}/\sigma_{yx_{ss}}$ decays as a function of time for $Z = 10$ (<i>blue/solid curve</i>) and $Z = 100$ (<i>red/dashed curve</i>), where $\sigma_{yx_{ss}}$ is the steady-state value of the shear stress under start-up shear flow.	95
5.21	Simulations of shear stress evolution under start-up and cessation of shear flow with $\dot{\gamma} = 1$ for $0 < t < 200$ and $\dot{\gamma} = 0$ for $200 < t < 300$ for the two-species network model with fractal breakage/recombination processes. Here $Z = 10$. Left: The shear stress σ_{yx} grows as a function of time for $\alpha = 1$ (<i>blue/solid curve</i>) and $\alpha = 0.6$ (<i>magenta/dashed curve</i>). Right: The scaled shear stress $\sigma_{yx}/\sigma_{yx_{ss}}$ decays as a function of time for $\alpha = 1$ (<i>blue/solid curve</i>) and $\alpha = 0.6$ (<i>magenta/dashed curve</i>), where $\sigma_{yx_{ss}}$ is the steady-state value of the shear stress under start-up shear flow.	96
5.22	Stress relaxation under a step strain is plotted for the two-species network model with fractal breakage/recombination processes. Left: The stress decay is compared for $Z = 10$ (<i>blue/solid curve</i>) and $Z = 100$ (<i>red/dashed curve</i>) with $\alpha = 1$. Right: The stress decay is compared for $Z = 10$ (<i>blue/solid curve</i>) and $Z = 100$ (<i>red/dashed curve</i>) with $\alpha = 0.6$	96
5.23	Stress relaxation under a step strain is plotted for the two-species network model with fractal breakage/recombination processes with $\alpha = 1$ (<i>blue/solid curve</i>) and $\alpha = 0.6$ (<i>magenta/dashed curve</i>). Here $Z = 10$	97

5.24	The evolution of the shear stress for the subordinated two-species network model under start-up and cessation of shear flow for $\dot{\gamma} = 1$ for $0 < t < 150$ and $\dot{\gamma} = 0$ for $150 < t < 250$. Here $\beta = 0.6$. Left: Stress growth is compared for $Z = 10$ (<i>blue/solid curve</i>) and $Z = 100$ (<i>red/dashed curve</i>). Right: Stress relaxation is compared for $Z = 10$ (<i>blue/solid curve</i>) and $Z = 100$ (<i>red/dashed curve</i>).	100
5.25	The shear stress relaxation for the subordinated two-species network model following a step strain for $Z = 10$ (<i>blue/solid curve</i>) and $Z = 100$ (<i>red/dashed curve</i>). Here $\beta = 0.6$	101

ABSTRACT

Soft materials are all around us; they may appear as consumer products (e.g. detergents, shampoos), foods (e.g. bread dough, jello, ketchup), or biological materials (e.g. blood, muscle). The wide range of applications for which they are used, as well as their complex structural and dynamic properties, have made soft materials appealing to both industry and academia. In particular the interest in studying the properties of soft materials both experimentally and theoretically has steadily increased. One example of a soft material is wormlike micellar solutions [28, 29]. These solvent-surfactant-salt mixtures are excellent exemplar fluids because, depending on the temperature and composition, they may exhibit close to mono-exponential or, alternatively, power-law or stretched-exponential stress decay. When these materials are probed with a sinusoidally varying shearing strain, their viscoelastic moduli may be characterized by a power-law stress response, $G' \sim G'' \sim \omega^\alpha$, where α is the power-law exponent and G', G'' are the storage and loss modulus, respectively. This behavior in frequency space reflects a power-law stress relaxation behavior of the modulus, $G(t) \sim t^{-\alpha}$, in physical/time space. Of particular interest to this thesis is the development of stochastic models that can capture the stress relaxation behavior of such materials in the small strain limit, which is non-exponential in time as opposed to exponential.

Continuous time random walk (CTRW) or subordinated Langevin processes are utilized to model systems exhibiting non-exponential relaxation behavior or anomalous diffusion [20]. Stochastic simulations using the CTRW approach or the subordination method are carried out in this thesis for one-dimensional systems in which the probability density distribution of particle positions is described by a fractional Fokker-Planck equation (FFPE). The equivalence of the CTRW simulation and the subordination simulation with that of the FFPE is analyzed through the simulation of an ensemble

of particle trajectories. Simulation algorithms are tested using one-dimensional cases and the simulated particle dynamics suggest that CTRW processes or subordinated Langevin dynamics can be included in soft material mesoscale dynamics to capture the anomalous transport.

To model the non-exponential stress relaxation dynamics of soft gel systems which are three-dimensional fluids, stochastic models are simulated using transient network theory as developed and combined with the CTRW and subordinated Langevin processes. This approach enables us to connect the microstructural dynamics of certain soft gel-like materials with macroscale experimental observations by examining the material properties under homogeneous shear flow conditions. The study shows that transient network models combined with CTRW or subordination processes can successfully predict the non-exponential stress relaxation dynamics of soft materials. Future work should include the understanding of this class of models for other types of flows, e.g. inhomogeneous (shear-banded) flows, as well as combining the CTRW approach in a transient network model (with the network topology tracked) developed by van den Brule and Hoogerbrugge [7].

Chapter 1

INTRODUCTION

Soft materials are widely in use in view of their special properties. A great deal of industrial research is focused on modifying materials chemically or physically to produce desired rheological properties. Therefore, it is vital to develop a comprehensive and predictive understanding of the dynamical behaviors of these complex materials under flow conditions. This thesis is focused on formulating mathematical models from a mesoscopic point of view and performing stochastic simulation to analyze the macroscopic fluid dynamics. Especially, we are interested in examining the relaxation dynamics observed in soft gel-like materials. The outline of this thesis is as follows. In Chapter 1, soft material systems are introduced and experimental observations of their properties in shear flow are reviewed. In Chapter 2, different types of shear flow are summarized and so are classical constitutive models which have been developed for modeling viscoelastic materials. In Chapter 3, fractional constitutive models and Cates reptation model with breakage and recombination chain dynamics are introduced to describe the power-law/stretched-exponential relaxation behaviors of soft materials. In Chapter 4, continuous time random walk theory is reviewed and the Monte Carlo simulation of continuous time random walk under the influence of external velocity and/or force fields is presented. In Chapter 5, stochastic models are formulated in the context of transient network theory combined with continuous time random walk or subordinated Langevin dynamics to model the subdiffusive behavior and the non-exponential relaxation dynamics of soft-gel systems.

1.1 Soft Materials

As pointed out in the 1991 Nobel lecture by P.G. de Gennes, the major features of soft matter lie in the complexity and flexibility of its underlying microstructure. Exploring the underlying fundamentals has been and is still a great challenge in academic and industrial research. One way to picture the microstructure of these materials is to consider a wormlike micellar surfactant system. The surfactant molecules are composed of two chemically bonded groups; a hydrophobic tail and a hydrophilic head (Figure 1.1 *left*). In an aqueous solution, these surfactant molecules self-assemble into aggregates of different shapes including spheres, ellipsoids and bilayers depending on the surfactant concentration, ionic strength and temperature. In this thesis, we are primarily interested in the long flexible cylindrical structures (called wormlike micelles) of the surfactant system (Figure 1.1 *middle*). Above the critical micelle concentration, these wormlike micelles (worms) entangle to form a physical network, a similar structure to that of entangled polymer solutions (Figure 1.1 *right*).



Figure 1.1: Left: Schematic of a surfactant molecule with a hydrophobic tail and a hydrophilic head. Middle: Schematic of a cylindrical shaped wormlike micelle formed by surfactants hiding their tails from water and their head groups forming an outer shell. Right: Schematic of an entangled network of wormlike micellar chains scales.

Soft materials exhibit fascinating fluid motion and material properties. Rheological experiments are performed on these complex fluids to probe their flow behaviors. In rheological testing, a specific flow deformation is imposed on the material and then the stresses generated in the flowing fluid are measured, or vice versa. The material's

responses to the imposed flows are recorded and fluids can be categorized by the material functions. Unlike Newtonian fluids which can be characterized by two material constants, the density ρ and the viscosity η , these non-Newtonian fluids require a variety of experimental tests to characterize their material functions based on different flow conditions. In this thesis, we focus on the transient behavior of soft materials under imposed homogeneous shearing flow. The time evolution of stress responses of a particular material under the shear flow is of special interest. A few key experimental results are presented below to show how soft materials differ from general viscoelastic fluids.

1.2 General Experimental Results

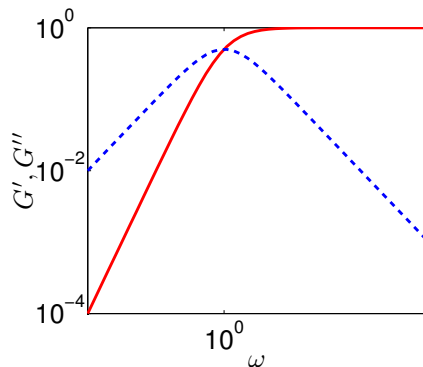


Figure 1.2: The storage modulus G' (red/solid line), and loss modulus G'' (blue/dashed line), for a viscoelastic material as functions of frequency ω in small-amplitude oscillatory shear (SAOS).

The small-amplitude oscillatory shear experiment (SAOS) is performed by imposing a small-amplitude sinusoidal oscillation on the upper of the two parallel plates and the stress response of the sample between the plates is measured. Viscoelastic materials in SAOS flows often behave as in Figure 1.2, where the measured storage and loss moduli are well fitted with the following (Maxwellian) functions of the frequency ω

$$G'(\omega) = \frac{\eta_0 \lambda \omega^2}{1 + \lambda^2 \omega^2}, \quad G''(\omega) = \frac{\eta_0 \omega}{1 + \lambda^2 \omega^2}. \quad (1.1)$$

Here η_0 is the zero-shear-rate viscosity and λ is the relaxation time of the test fluid. The storage modulus $G'(\omega)$ gives information about the elastic character of the fluid, while the loss modulus $G''(\omega)$ tells about the viscous character of the fluid [2]. In Figure 1.2, the dynamic moduli intersect ($G'(\omega) = G''(\omega)$) at an ω_0 when $\lambda\omega_0 = 1$. This time scale $\lambda = 1/\omega_0$ represents the crossover from a viscous ($G'' > G'$) to an elastic ($G' > G''$) behavior. As $\omega \rightarrow 0$, $G'(\omega) \sim \eta_0\lambda\omega^2$ and $G''(\omega) \sim \eta_0\omega$, the viscous property dominates. As $\omega \rightarrow \infty$, $G'(\omega) \sim \eta_0/\lambda$ and $G''(\omega) \sim \eta_0/(\lambda^2\omega)$, the elasticity dominates [2]. Constitutive models that predict this rheological behavior are introduced in Chapter 2.

For the surfactant erucyl dimethyl amidopropyl betaine, EDAB worms (a class of wormlike micelles), Raghavan and Douglas [28] showed that the material behaves like a Maxwellian viscoelastic fluid at high temperature, that is, a single relaxation time scale was discovered (Figure 1.3 *right*). As the temperature was lowered from 70°C to 60°C , the frequency ω_0 at which G' and G'' intersect shifted to a smaller value, which corresponds to an increase in the system relaxation time since $\lambda \sim 1/\omega_0$. At even lower temperatures, e.g. 40°C and 25°C , $\omega_0 \rightarrow 0$ and the storage modulus G' and loss modulus G'' curves are almost parallel to each other over the entire frequency range with $G' \gg G''$, a characteristic of a gel.

In step strain experiments, a sample at rest between parallel plates is disturbed by a sudden shearing displacement. The ensuing time-dependent stress generated by this action is then recorded. The relaxation modulus of a Maxwellian material is well described by an exponential function $G(t) = \tau_{yx}(t)/\gamma_0 = G_0 \exp(-t/\lambda)$, where $\tau_{yx}(t)$ is the shear stress at time t , G_0 is the elastic modulus constant, λ is the relaxation time and γ_0 is the shear strain [2]. Relaxation processes deviating from this classical exponential behavior are encountered in rheological experiments of soft materials. For example, a gluten gel [22] showed a power law relaxation modulus behavior $G(t) = St^{-n}$ following a step strain experiment with $S = 1260 \pm 50 \text{ Pa s}^n$, $n = 0.175 \pm 0.005$, for approximately three decades of time. We kept the SI units for all experimental measurements in this thesis; Pa is Pascals ($1 \text{ Pa} = 1 \text{ N/m}^2$, N is Newtons, m is meters)

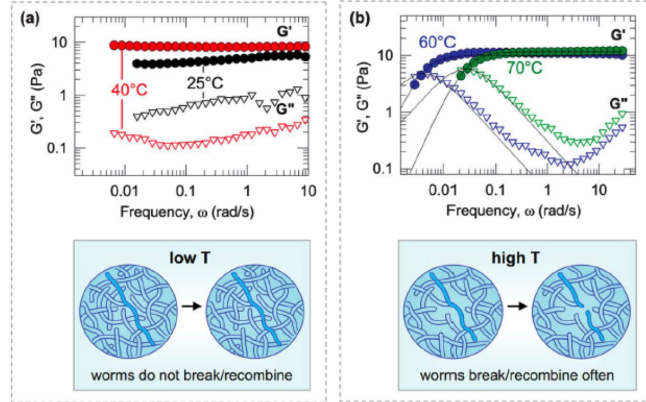


Figure 1.3: Dynamic frequency experiment on a sample containing 50mM concentration of the surfactant erucyl dimethyl amidopropyl betaine (EDAB) at different temperatures [28]. Reproduced from [28] with permission of The Royal Society of Chemistry.

and s is seconds.

Returning to a wormlike micellar solution (CPyCl in NaSal), as observed in [29], the relaxation modulus is well described by a stretched-exponential function $G(t) = G_0 \exp[-(t/\lambda)^\alpha]$. The exponent α varies with the salt/surfactant concentration ratio. For salt/surfactant concentration ratios above 0.6, the stress decay is purely exponential ($\alpha = 1$). A decrease of the stretched-exponential exponent α from 1 is observed as the concentration ratio decreases below 0.6. In this regime, the relaxation modulus shows a stretched-exponential pattern.

1.3 Review of Theoretical Approaches

Soft materials exhibit many distinct rheological properties as compared to Maxwellian viscoelastic fluids. The power-law/stretched-exponential relaxation behaviors observed in surfactant solutions [4, 28, 29], gels [22, 37], and biological tissues [15, 34], are of particular interest in this thesis.

Much work has been done to study the fluid dynamics of soft materials. While continuum-based constitutive models have been extensively studied, these canonical models fail to predict non-exponential stress relaxation behavior in the small strain

limit (see Chapter 2) [2, 21]. Fractional differential equation models have been proposed to simulate the power-law (in time) stress decay. A one-dimensional scalar fractional Maxwell model (FMM) was derived from the Maxwell model by replacing the time derivative with a fractional time derivative [14]. Yang et al [38] developed a tensorial formulation of the fractional Maxwell model (three-dimensional) and applied it to homogeneous steady-shear flows. The above phenomenological models have limited applicability since the underlying physics are not considered and it is therefore difficult to account for the nonlinear dynamics.

Cates [4] modeled an equilibrium system of wormlike micelles with a specific polydispersity in which the chains diffuse (reptate) in their tubes as well as breaking and recombining with the entangled network. The interplay between the reptation and breakage/recombination events results in very different stress relaxation behaviors and time scales. In the fast-breaking limit, the system mainly relaxed its stress through the breaking/reforming and the stress decay exhibited an exponential behavior. In the pure reptation regime (no breaking/reforming), this model predicted a stretched-exponential stress relaxation. This prediction is consistent with experimental findings of surfactant solutions. But, this model is limited to describing the wormlike micellar system in the equilibrium regime.

1.4 Our Approach

Continuous time random walk (CTRW) models have been developed to model one-dimensional particle systems exhibiting subdiffusion and non-exponential relaxation dynamics [20]. Furthermore, Monte Carlo simulations of particles following a CTRW have been implemented by Fulger et al [10]. To further investigate CTRW processes within the context of the complicated three-dimensional fluid dynamics models, we first extend the Monte Carlo simulation of one-dimensional particle dynamics, governed by a CTRW to include the effect of an external velocity or force field. The model predictions are compared with theoretical results provided by Metzler and Klafter [20].

In addition, a subordination simulation is examined. This method provides an alternative way to simulate particle dynamics undergoing CTRW processes by rescaling the time variable. Numerical simulations for both CTRW and subordination are analyzed and these simulation algorithms lay the ground work for simulating soft material fluid dynamics in the three-dimensional space.

Due to the presence of the reversible cross-links/entanglements between the macromolecules/aggregates of a soft material system, it is attractive to analyze the behavior of the soft gels within the context of transient network theory. Transient network theory can include breakage/reforming of the network entanglements, in which Hookean bead-spring dumbbells have been used as the fundamental connector units of the soft material systems. Langevin equations have been formulated to describe the dynamics of each dumbbell connector, in which the dumbbell can experience elastic spring force, drag force due to the solvent, and a Brownian force as well as attaching or detaching from the network.

Stochastic simulation provides a powerful tool to investigate these models. In particular in this thesis breakage/recombination events from the network are simulated probabilistically. Many soft materials exhibit power-law/stretched-exponential, as opposed to exponential, relaxation dynamics. In this thesis, in order to capture these non-exponential stress relaxation behaviors we introduce CTRW processes (as opposed to conventional random walk processes) to the stochastic models. This CTRW process is introduced into the breaking/reforming processes as well as to the intermolecular kinetics. Furthermore, subordination method is used to simulate a soft material system with the overall dynamics modeled as CTRW processes, i.e. the convection due to shearing flow, elastic spring and Brownian force, and breakage/recombination. These generalizations of conventional transient network models at the mesoscale improve on the fractional differential equation (at the macroscale) models in versatility and direct physical interpretation. The simulations reported in this thesis show that these generalizations of conventional models do evidence non-exponential stress relaxation dynamics as well as subdiffusive effects.

Chapter 2

CONSTITUTIVE MODELING

In chapter 1, experimental findings of soft materials under homogeneous shearing flow were introduced. In this chapter, the standard shear flow patterns are presented and the material functions that can be obtained from each experiment are reviewed. Then some exemplar constitutive models developed to model viscoelastic materials that exhibit exponential stress decay behaviors are introduced.

2.1 Geometry

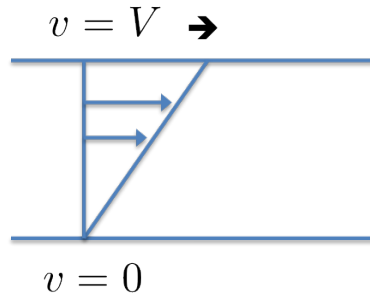


Figure 2.1: Steady simple shear flow; the top plate moves with a constant velocity V , the bottom plate is fixed. For a Newtonian fluid, the velocity distribution between the plates is linear.

Figure 2.1 shows a two-dimensional schematic of a velocity profile in simple Newtonian shearing flow. Simple shear flow can be generated by placing a sample fluid between two parallel plates with the top plate moving with a certain velocity and the bottom plate being held stationary. In such an idealized parallel plate geometry, we choose the flow direction as x-axis, the direction in which the velocity changes (the gradient direction) as y-axis, and the z-axis is neutral. Realistic examples of simple

shear rheometers include concentric cylinders (Taylor-Couette), plate-plate and cone-and-plate rheometers. A more comprehensive review can be found in [2, 21].

2.2 Stress Tensor for Shear Flows

In a homogeneous (time-dependent) rectangular shear flow, the velocity is assumed to be

$$\mathbf{v} = (\dot{\gamma}_{yx}(t)y, 0, 0), \quad (2.1)$$

where $\dot{\gamma}_{yx}$ is the xy-component of the shear rate tensor. The absolute value of $\dot{\gamma}_{yx}$ is called the shear rate $\dot{\gamma} = |\dot{\gamma}_{yx}|$. The shear-rate tensor for this flow, $\dot{\boldsymbol{\gamma}} = \nabla \mathbf{v} + (\nabla \mathbf{v})^t$, is

$$\dot{\boldsymbol{\gamma}} = \begin{pmatrix} 0 & \dot{\gamma}_{yx}(t) & 0 \\ \dot{\gamma}_{yx}(t) & 0 & 0 \\ 0 & 0 & 0 \end{pmatrix}. \quad (2.2)$$

Due to the simplicity of the velocity field for simple shear flow, the stress tensor is symmetric and has only four independent nonzero components,

$$\boldsymbol{\tau} = \begin{pmatrix} \tau_{xx} & \tau_{yx} & 0 \\ \tau_{yx} & \tau_{yy} & 0 \\ 0 & 0 & \tau_{zz} \end{pmatrix}. \quad (2.3)$$

The quantities of experimental interest are the shear stress and two normal stress differences. The xy-component of the stress tensor is the shear stress τ_{yx} . The first normal stress difference is defined as $N_1 = \tau_{xx} - \tau_{yy}$, and the second normal stress difference $N_2 = \tau_{yy} - \tau_{zz}$ [2].

2.3 Shear Flow Material Functions

2.3.1 Small-Amplitude Oscillatory Shear (SAOS)

In a small-amplitude oscillatory shear (SAOS) experiment [2], the fluid is subjected to a sinusoidal oscillatory shear strain of small amplitude ($\gamma_0 \ll 1$),

$$\gamma_{yx}(t) = \gamma_0 \sin(\omega t), \quad (2.4)$$

thus, the shear rate follows

$$\dot{\gamma}_{yx}(t) = \gamma_0 \omega \cos(\omega t) = \dot{\gamma}_0 \cos \omega t, \quad (2.5)$$

where $\gamma_0 = \dot{\gamma}_0/\omega$ and $\dot{\gamma}_0$ are the (positive) amplitudes of the shear strain and shear rate oscillations, respectively. When a sample is under SAOS, the shear stress that is produced is a sine wave of the same frequency,

$$\tau_{yx}(t) = -A(\omega)\gamma_0 \sin(\omega t + \delta), \quad (2.6)$$

where δ gives the phase difference between the strain and the stress responses. Rewriting equation (2.6) using trigonometric identities gives $\tau_{yx}(t) = -(A(\omega)\gamma_0 \cos \delta) \sin \omega t - (A(\omega)\gamma_0 \sin \delta) \cos \omega t$. The storage modulus $G'(\omega)$ is the amplitude of the portion of the stress that is in phase with the strain (proportional to $\sin \omega t$) divided by γ_0 , and the loss modulus $G''(\omega)$ is the amplitude of the portion of the stress that is out of phase with the strain (proportional to $\cos \omega t$) divided by γ_0 . Therefore,

$$G' = A(\omega) \cos \delta, \quad (2.7)$$

$$G'' = A(\omega) \sin \delta, \quad (2.8)$$

and $A(\omega) = \sqrt{G'^2 + G''^2}$, $\tan \delta = G''/G'$. For a Newtonian fluid $\tau_{yx} = -\eta_0 \dot{\gamma}_{yx}$, the response is always completely in phase with the strain rate, $G' = 0$ and $G'' = \eta_0 \omega$. For a viscoelastic material, both G' and G'' are functions of ω as in (1.1). For large strains, G' and G'' may be functions of γ_0 as well.

2.3.2 Step Strain Experiment

Stress relaxation can be observed in a step strain experiment $\gamma_{yx}(t) = \gamma_0 H(t)$ and $\dot{\gamma}_{yx}(t) = \gamma_0 \delta(t)$. Here $H(t)$ is the Heaviside unit step function, $\delta(t)$ is the delta function, and γ_0 is the shear strain. The relaxation modulus $G(t)$ describes the time decay of the shear stress and is defined by

$$G(t) = \frac{\tau_{yx}(t)}{\gamma_0}. \quad (2.9)$$

For a Newtonian fluid, the stress instantly relaxes to zero after application of a sudden shearing displacement, while the stresses generated in viscoelastic materials do not go to zero immediately but rather decay over a finite amount of time. For soft gel-like materials, the stress relaxation is very slow and it will take an infinite amount of time for the stress to relax away.

2.3.3 Start-up Followed by Cessation of Steady Shear Flow

In a stress growth experiment, a constant shear rate $\dot{\gamma}_0$ is imposed on the sample fluid at rest at $t = 0$, so $\dot{\gamma}_{yx} = \dot{\gamma}_0 H(t)$. All components of the stress tensor are zero when the steady shearing is begun. For times $t > 0$, the resulting stresses approach their steady-state shear flow values which can be functions of the imposed shear rate. From this (steady-state) flow curve, the steady-state shear viscosity is defined as the negative value of the ratio of steady-state shear stress value $\tau_{yx_{ss}}$ to the shear rate,

$$\eta(\dot{\gamma}_0) = -\frac{\tau_{yx_{ss}}(\dot{\gamma}_0)}{\dot{\gamma}_0}, \quad (2.10)$$

where the viscosity measures a fluid's resistance to the rate of deformation. In this flow, for Newtonian fluids which exhibit a linear relation between the steady-state shear stress and the shear rate, the viscosity is constant. Viscoelastic fluids, on the other hand, may have a viscosity dependent on the shear rate.

In cessation of steady shear flow, the motion of a fluid undergoing steady shearing flow with $\dot{\gamma}_{yx} = \dot{\gamma}_0$ for $0 < t < t_0$ is suddenly stopped at $t = t_0$ so that $\dot{\gamma}_{yx} = 0$ for $t \geq t_0$. The stress relaxation of the steady shear flow stresses is then observed.

The above sections provide a brief summary of all types of transient shear flows encountered in this thesis. In the next section, several existing macroscale constitutive models are introduced and their transient shear flow behavior predictions are presented.

2.4 Constitutive Modeling

Constitutive modeling which describes the behavior of a particular material by adapting mathematical equations to experimental data has been a cornerstone in

computational fluid dynamics [2, 21]. In this chapter dimensional variables are denoted by a prime, $()'$.

2.4.1 Basic Fluid Flow Governing Equations

Any fluid flow problem can be described by three physical conservation laws: the law of conservation of mass, the law of conservation of momentum and a constitutive equation [2, 21]. The continuity equation derived by conserving the mass is:

$$\frac{\partial \rho'}{\partial t'} = -\nabla' \cdot \rho' \mathbf{v}', \quad (2.11)$$

where ρ' is the fluid density and \mathbf{v}' is the fluid velocity. For incompressible fluids, the density is constant, thus equation (2.11) reduces to

$$\nabla' \cdot \mathbf{v}' = 0. \quad (2.12)$$

The equation of motion obtained by balancing momentum in the absence of gravity is:

$$\frac{\partial(\rho' \mathbf{v}')}{\partial t'} = -\nabla' \cdot \rho' \mathbf{v}' \mathbf{v}' - \nabla' \cdot \boldsymbol{\pi}', \quad (2.13)$$

where $\boldsymbol{\pi}'$ is the total stress tensor and contains all the information about the state of stress at a point. The total stress $\boldsymbol{\pi}'$ is the sum of two parts:

$$\boldsymbol{\pi}' = \boldsymbol{\tau}' + p\mathbf{I}, \quad (2.14)$$

where $\boldsymbol{\tau}'$ is the extra stress tensor and $p\mathbf{I}$ is the isotropic equilibrium stress.

A major area of rheological research involves developing the constitutive equations that describe the relation of the extra stress $\boldsymbol{\tau}'$ and the flow deformation $\dot{\boldsymbol{\gamma}}' = \nabla' \mathbf{v}' + (\nabla' \mathbf{v}')^t$. For incompressible Newtonian fluids, the constitutive equation is

$$\boldsymbol{\tau}' = -\eta_0 \dot{\boldsymbol{\gamma}}', \quad (2.15)$$

where η_0 is the constant viscosity of the fluid. This linear relation is true for all flow conditions. Below we describe some constitutive equations for viscoelastic materials.

2.4.2 Upper-Convected Maxwell (UCM) Model

A simple model developed to describe a viscoelastic material is the Maxwell model. The model can be represented by a viscous dashpot connected in series with an elastic spring, as shown in Figure 2.2. The relationship describing dependence of the shear stress τ'_{yx} and shear rate $\dot{\gamma}'_{yx}$ is given by

$$\lambda \frac{d\tau'_{yx}}{dt'} + \tau'_{yx} = -\eta_0 \dot{\gamma}'_{yx}, \quad (2.16)$$

where λ is the relaxation time and η_0 is the zero-shear-rate viscosity. The usefulness of this linear model is limited to small-displacement-gradient flows or to Boger fluids [2].

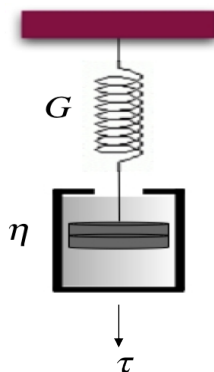


Figure 2.2: A spring and a dashpot connected in series

The upper-convected Maxwell (UCM) model is a generalization of the Maxwell model for arbitrary three-dimensional flows obtained by replacing the time derivative in equation (2.16) with the upper-convected time derivative [2],

$$\lambda \boldsymbol{\tau}'_{(1)'} + \boldsymbol{\tau}' = -\eta_0 \boldsymbol{\gamma}'_{(1)'}, \quad (2.17)$$

where the convected time derivative of the stress tensor $\boldsymbol{\tau}'_{(1)'}$ is defined by

$$\boldsymbol{\tau}'_{(1)'} = \frac{\partial \boldsymbol{\tau}'}{\partial t'} + \mathbf{v}' \cdot \nabla' \boldsymbol{\tau}' - (\nabla' \mathbf{v}')^t \cdot \boldsymbol{\tau}' - \boldsymbol{\tau}' \cdot (\nabla' \mathbf{v}'). \quad (2.18)$$

For homogeneous shearing flows $\mathbf{v}' = (\dot{\gamma}'_{yx}y', 0, 0)$, the second term on the right hand side of equation (2.18) is always zero. For SAOS flow with $\gamma'_{yx}(t') = \gamma_0 \sin(\omega't')$, $\tau'_{yy} = 0$, and the shear stress satisfies the differential equation

$$\tau'_{yx} + \lambda \frac{d\tau'_{yx}}{dt'} = -\eta_0 \gamma_0 \omega' \cos \omega't'. \quad (2.19)$$

The storage modulus G' (shear stress component in-phase with the strain) and loss modulus G'' (shear stress component out-of-phase with the strain) are related to shear stress τ'_{yx} by

$$\tau'_{yx} = -G'(\omega')\gamma_0 \sin \omega't' - G''(\omega')\gamma_0 \cos \omega't'. \quad (2.20)$$

Substituting equation (2.20) into equation (2.19) gives the storage and loss moduli for the Maxwellian materials, $G'(\omega') = \eta_0 \lambda \omega'^2 / (1 + \lambda^2 \omega'^2)$ and $G''(\omega') = \eta_0 \omega' / (1 + \lambda^2 \omega'^2)$, as in equation (1.1).

For the start-up of steady shear flow $\dot{\gamma}' = \dot{\gamma}_0 H(t')$, the stresses τ'_{xx} and τ'_{yx} are given by

$$\tau'_{xx} = -2\eta_0 \dot{\gamma}_0^2 \left[1 - \left(1 + \frac{t'}{\lambda} \right) \exp(-t'/\lambda) \right], \quad (2.21)$$

$$\tau'_{yx} = -\eta_0 \dot{\gamma}_0 [1 - \exp(-t'/\lambda)], \quad (2.22)$$

$\tau'_{yy} = 0$. For the UCM model, a linear relation between the viscosity and the shear rate and a non-zero first normal stress difference are predicted.

2.4.3 Giesekus Model

The Giesekus model is one exemplar non-linear model which takes into consideration the non-isotropic drag of long polymer strands (or worms) [11]. The constitutive equation for a Giesekus fluid is given by

$$\boldsymbol{\tau}' + \lambda \boldsymbol{\tau}'_{(1)'} - \alpha (\boldsymbol{\tau}' \cdot \boldsymbol{\tau}') = -\eta_0 \dot{\gamma}', \quad (2.23)$$

where α controls the degree of the anisotropic drag effect. When $\alpha = 0$, the drag is isotropic and the model reduces to the UCM model. When $\alpha > 1/2$, the model predicts a non-monotonic stress-strain rate relation in shear [2].

2.4.4 Vasquez-Cook-McKinley (VCM) Model

The VCM model is a two-species model (Giesekus and UCM are single-species models) which consider two types of network strands, long chains with length L (Species A) and the short chains with length $L/2$ (Species B) [36]. This two-species formulation is a discrete version of the Cates reptation model [4], in which there exists an exponential length distribution of micellar strands at equilibrium. The breaking and reforming dynamics are simplified to include two processes: the long chains from species A can break at the middle to form two chains of length $L/2$. In the mean time, two short chains can join at their ends to form a long chain (Figure 2.3).

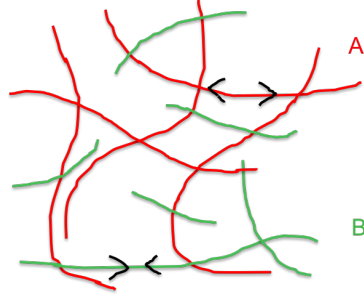


Figure 2.3: Long species A can break to form two shorter species B and two shorter chains of species B can form a longer chain A.

The non-dimensional constitutive equations (see [36] for non-dimensionalization), include equations for the number density of each species and the stress from each species [36],

$$\mu \frac{dn_A}{dt} = 2\delta_A \nabla^2 n_A - \delta_A \nabla \nabla : \mathbf{A} + \frac{1}{2} c_B n_B^2 - c_A n_A, \quad (2.24)$$

$$\mu \frac{dn_B}{dt} = 2\delta_B \nabla^2 n_B - 2\delta_B \nabla \nabla : \mathbf{B} - c_B n_B^2 + 2c_A n_A, \quad (2.25)$$

$$\mu \mathbf{A}_{(1)} + \mathbf{A} - n_A \mathbf{I} - \delta_A \nabla^2 \mathbf{A} = c_B n_B \mathbf{B} - c_A \mathbf{A}, \quad (2.26)$$

$$\epsilon \mu \mathbf{B}_{(1)} + \mathbf{B} - \frac{n_B}{2} \mathbf{I} - \epsilon \delta_B \nabla^2 \mathbf{B} = -2\epsilon c_B n_B \mathbf{B} + 2\epsilon c_A \mathbf{A}, \quad (2.27)$$

where \mathbf{A} and \mathbf{B} are the stress contribution from species A and B, and n_A and n_B are the number density functions of species A and B. The ratio of the relaxation time of the short chains to the relaxation time of the long chains is denoted by

$$\epsilon = \frac{\lambda_B}{\lambda_A}, \quad (2.28)$$

and the ratio of the relaxation time of the long chains to the effective relaxation time of the elastic network is

$$\mu = \frac{\lambda_A}{\lambda_{\text{eff}}}. \quad (2.29)$$

In the constitutive equations ((2.24) - (2.27)), δ_A and δ_B are non-dimensional diffusion constants for species A and B. Further, c_A and c_B are dimensionless breakage and recombination rates defined as [36]

$$c_A = c_{Aeq} + \frac{1}{3}\xi\mu \left(\dot{\gamma} : \frac{\mathbf{A}}{n_A} \right), \quad (2.30)$$

$$c_B = c_{Beq}. \quad (2.31)$$

The non-dimensional stress tensor $\boldsymbol{\sigma}$ is given by

$$\boldsymbol{\sigma} = \mathbf{A} + 2\mathbf{B}. \quad (2.32)$$

The stress tensor $\boldsymbol{\sigma} = -\boldsymbol{\tau} + \mathbf{I}$ and is resulted from the stress contribution of all the species in the system. It is convenient to regard this stress tensor $\boldsymbol{\sigma}$ in this model.

This model was examined in various flow conditions, including steady-state shear flow, step strain, and small-amplitude oscillatory flow (SAOS) [36]. In SAOS flow, the VCM model predicts the storage modulus and loss modulus (in dimensional form) as follows:

$$G' = G_0 \left[\frac{(\lambda_{\text{eff}}\omega')^2}{1 + (\lambda_{\text{eff}}\omega')^2} + n_B^0 \frac{(\lambda_B\omega')^2}{1 + (\lambda_B\omega')^2} \right], \quad (2.33)$$

$$G'' = G_0 \left[\frac{\lambda_{\text{eff}}\omega'}{1 + (\lambda_{\text{eff}}\omega')^2} + n_B^0 \frac{\lambda_B\omega'}{1 + (\lambda_B\omega')^2} \right] + \eta_s\omega', \quad (2.34)$$

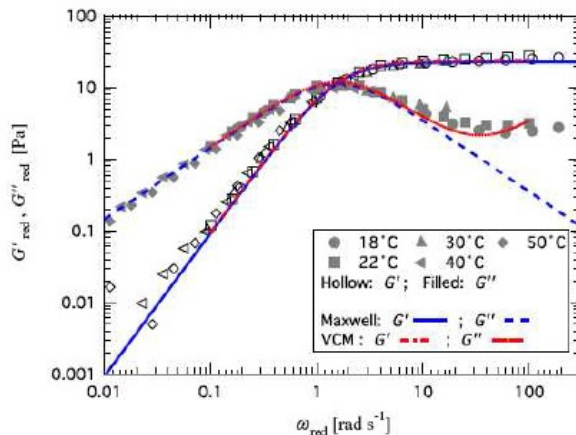


Figure 2.4: Small-amplitude oscillatory results for a 100 mM/50 mM CpyCl/NaSal solution showing the storage (hollow symbols) and loss (filled symbols) moduli. The dashed lines correspond to fits from a single-mode upper-convected Maxwell model. The solid lines correspond to fits to the data from the VCM model showing the upturn in the loss modulus due to the second, non-Newtonian species [26]. Reprinted with permission from [26]. Copyright 2010, The Society of Rheology.

or essentially, in linear theory, a two-mode Maxwell model with well separated modes. Here the dimensional frequency is $\omega' = \omega/\lambda_{\text{eff}}$ and $\lambda_{\text{eff}} = \lambda_A/(1 + c'_{Aeq}\lambda_A)$ is the effective relaxation time of the networks. The term $\eta_s\omega$ in the loss modulus equation arises from the Newtonian solvent with viscosity η_s , G_0 is the characteristic elastic modulus, n_B^0 is the number density of species B in equilibrium. The VCM model predictions fit well with the experimental data of particular wormlike micellar solutions at a particular temperature and concentration (Figure 2.4). This is due to the addition of a second, non-Newtonian species and to the fact that the effective relaxation time of the long chain micellar system is reduced from the reptation time of the long species due to breakage. This model does not generate good predictions when the temperature or concentration are changed [36].

The two non-linear models discussed above, the Giesekus model and the VCM model, are variants of the UCM model and as such give an exponential stress relaxation prediction in the linear viscoelastic regime [11, 36]. There are a large number of soft

gel-like materials that do not fall under this category. Thus, alternative models have been considered to capture the non-exponential stress relaxation dynamics exhibited in those cases, i.e. fractional constitutive models and the Cates reptation model [4, 14].

Chapter 3

GENERAL MODELS FOR DESCRIBING NON-EXPONENTIAL STRESS RELAXATION

The relaxation processes of many soft materials exhibit a power-law $G'(t) \sim (t'/\lambda)^{-\alpha}$ or stretched-exponential $G'(t) \sim \exp(-(t'/\lambda)^\alpha)$ decay, where $G'(t)$ is the relaxation modulus, λ is the relaxation time, $0 < \alpha < 1$ [14, 15, 22, 28, 29, 34, 37]. Power-law stress relaxation in the time domain implies power-law behavior in the storage modulus, $G'(\omega')$ and loss modulus, $G''(\omega')$ measured using SAOS experiments [22]. As we have seen in Chapter 2, standard constitutive models with integer-order derivatives fail to predict relaxation processes other than exponential relaxation $G'(t) \sim \exp(-t'/\lambda)$ in the linear regime. These soft matter systems often consist of complex interacting microstructures over multiple length and time scales. If Maxwellian relaxation mode is used, the shear stress would require summing a large number of relaxation modes $\tau'_{yx}(t) (= \gamma_0 G'(t)) = \sum_k \tau_k \exp(-t'/\lambda_k)$, where γ_0 is the shear strain, τ_k and λ_k are fitting constants [14, 15]. The number of Maxwellian relaxation modes needed to fit the stress relaxation data of biological samples varies with the scale of the measurement time or frequency. For that reason this approach lacks physical meaning [15]. In the last few decades, fractional calculus has become an increasingly popular tool for describing many physical systems [24, 27, 33]. Incorporation of fractional calculus into rheological modeling allows one to formulate constitutive relationships with very few parameters as shown in [14]. While fractional constitutive models are formulated from a macroscopic standpoint, Cates reptation model investigated the relaxation dynamics of wormlike micellar solutions from a mesoscopic point of view by using a one-dimensional stochastic approach [4]. In this chapter, we begin with the fundamentals of fractional derivatives. Then we introduce some fractional constitutive models (macroscale) and

reptation models (mesoscale) developed to capture the non-exponential relaxation processes. In this chapter, all dimensional variables are denoted using prime, (\prime).

3.1 Fractional Calculus

3.1.1 Definition

The two most widely used definitions for the fractional derivative of order α of a function $f(t)$ are the Riemann-Liouville definition and the Caputo definition [24, 27]. The Riemann-Liouville definition of the fractional derivative is

$${}_0D_t^\alpha f(t) = \frac{1}{\Gamma(1-\alpha)} \frac{d^n}{dt^n} \int_0^t (t-\tau)^{-\alpha} f(\tau) d\tau \quad (n-1 < \alpha \leq n). \quad (3.1)$$

Here α is the order of the fractional derivative, n is the smallest integer greater than α and Γ is the gamma function. When $\alpha = 1$, the Riemann-Liouville definition reduces to the normal first-order derivative. The Riemann-Liouville fractional derivative of a constant C is not zero,

$${}_0D_t^\alpha C = \frac{Ct^{-\alpha}}{\Gamma(1-\alpha)}. \quad (3.2)$$

The Caputo definition of the fractional derivative is

$${}_0^C D_t^\alpha f(t) = \frac{1}{\Gamma(1-\alpha)} \int_0^t (t-\tau)^{-\alpha} f^{(n)}(\tau) d\tau \quad (n-1 < \alpha \leq n), \quad (3.3)$$

where $f^{(n)}(t)$ is the n -th derivative of $f(t)$. Both definitions are obtained under the assumption that the function $f(t)$ must be n times continuously differentiable. The Caputo derivative of a constant is zero according to the definition. Differential equations with fractional derivatives are called fractional differential equations. The main advantage of Caputo's approach is that the initial conditions for fractional differential equations with Caputo derivatives take on the same form as for integer-order differential equations. This results in physically interpretable initial conditions, which contain $f(0)$, $f'(0)$, etc. However, the Riemann-Liouville approach leads to initial conditions with fractional derivatives at $t = 0$. Note that fractional differential equations with these two definitions agree with zero initial conditions, $f(0) = 0, f'(0) = 0, \dots, f^{(n)}(0) = 0$.

3.1.2 General Properties

The basic rules of differentiation hold for fractional differential operators,

(a) Linearity

$$D^\alpha(f_1 + f_2) = D^\alpha f_1 + D^\alpha f_2. \quad (3.4)$$

(b) Homogeneity

$$D^\alpha(Cf) = CD^\alpha f, \quad C \text{ is any constant.} \quad (3.5)$$

(c) Composition

$$D^\alpha(D^\beta f(t)) = D^\beta(D^\alpha f(t)) = D^{\alpha+\beta} f(t), \quad (3.6)$$

where D_t^α denotes either of the two mentioned fractional differentiations.

3.1.3 Techniques in the Fractional Calculus

The Laplace transform of fractional derivatives takes on different forms for the two definitions [24, 27]. The Laplace transform of the Riemann-Liouville fractional derivative is

$$\mathcal{L}\{ {}_0D_t^\alpha f(t); s \} = s^\alpha \hat{f}(s) - \sum_{k=0}^{n-1} s^k [{}_0D_t^{\alpha-k-1} f(t)]|_{t=0}. \quad (3.7)$$

The Laplace transform of the Caputo derivative is

$$\mathcal{L}\{ {}_0^C D_t^\alpha f(t); s \} = s^\alpha \hat{f}(s) - \sum_{k=0}^{n-1} s^k f^{(k)}(0), \quad (3.8)$$

where

$$\hat{f}(s) = \mathcal{L}\{ f(t); s \} = \int_0^\infty \exp(-st) f(t) dt, \quad (3.9)$$

and $f^{(k)}(0)$ is the k -th derivative of $f(t)$ at $t = 0$ (k is an integer). The Laplace transform of the Caputo derivative allows utilization of initial values of classical integer-order derivatives with known physical interpretations. The Fourier transform of both the Riemann-Liouville and Caputo derivatives is given by [27]

$$\mathcal{F}\{ {}_{-\infty}D_t^\alpha f(t); \omega \} = (i\omega)^\alpha \hat{f}(\omega), \quad (3.10)$$

where ${}_{-\infty}D_t^\alpha$ denotes either of the two mentioned fractional differentiations with lower limit being $-\infty$ and

$$\hat{f}(\omega) = \mathcal{F}\{f(t); \omega\} = \int_{-\infty}^{\infty} \exp(i\omega t) f(t) dt. \quad (3.11)$$

Here $f(t)$ is a continuous function and absolutely integrable in $(-\infty, \infty)$ [27].

3.2 Fractional Constitutive Models

3.2.1 Scott-Blair Model

Scott-Blair [31] first proposed a constitutive equation for the shear stress in terms of a fractional derivative

$$\tau'_{yx}(t') = \eta_0^\alpha {}^C D_{t'}^\alpha \gamma'_{yx}(t'), \quad (3.12)$$

where $\eta_0^\alpha = G_0 \lambda^\alpha$, G_0 is the constant modulus, and $0 \leq \alpha \leq 1$. This model effectively creates an element that interpolates between the constitutive responses of a spring and a dashpot. This model reduces to a spring $\tau'_{yx}(t') \propto \gamma'_{yx}(t')$ when $\alpha = 0$ and a dashpot $\tau'_{yx}(t') \propto \dot{\gamma}'_{yx}(t')$ when $\alpha = 1$. This model enables the quantitative description of viscoelastic behavior over a broad range of frequencies and timescales with only a few material parameters, η_0^α and α .

3.2.2 Fractional Maxwell Model

The fractional Maxwell model (FMM), which consists of two spring-pot elements in series, was studied in detail by Nonnenmacher [23] and Schiessel et al [30]. The constitutive equation for the scalar FMM is

$$\tau'_{yx} + \lambda^\alpha {}^C D_{t'}^\alpha \tau'_{yx} = G_0 \lambda^\beta {}^C D_{t'}^{\beta-1} \dot{\gamma}'_{yx}, \quad (3.13)$$

where $0 < \alpha \leq \beta \leq 1$ and an initial condition $\tau'_{yx}(0) = 0$ is assumed. Applying the Laplace transform to equation (3.13),

$$\hat{\tau}_{yx}(s) = \frac{G_0 \lambda^{\beta-\alpha} s^{\beta-1} \hat{\gamma}_{yx}(s)}{\lambda^{-\alpha} + s^\alpha}. \quad (3.14)$$

To solve the above equation, we introduce the two-parameter Mittag-Leffler function $E_{a,b}(z)$, which is defined as

$$E_{a,b}(z) = \sum_{k=0}^{\infty} \frac{z^k}{\Gamma(ak + b)}. \quad (3.15)$$

In particular, $E_{1,1}(z) = \exp(z)$, $E_{2,1}(z^2) = \cosh(z)$, $E_{2,1}(-z^2) = \cos(z)$, $E_{1/2,1}(\pm z^{1/2}) = \exp(z)\operatorname{erfc}(\mp z^{1/2})$ [24, 27]. The Laplace transform of $E_{\alpha,\beta}(-at^\alpha)$ is [27]

$$\int_0^{\infty} \exp(-st)t^{\beta-1}E_{\alpha,\beta}(-at^\alpha)dt = \frac{s^{\alpha-\beta}}{s^\alpha + a}. \quad (3.16)$$

By inverse Laplace transforming equation (3.14), we find that

$$\tau'_{yx}(t') = G_0 \int_0^{t'} \left(\frac{t' - s}{\lambda}\right)^{\alpha-\beta} E_{\alpha,\alpha-\beta+1} \left(-\left(\frac{t' - s}{\lambda}\right)^\alpha\right) \dot{\gamma}'_{yx}(s) ds. \quad (3.17)$$

The solution of the FMM following the imposition of a step strain $\gamma'_{yx} = \gamma_0 H(t')$ or $\dot{\gamma}'_{yx} = \gamma_0 \delta(t')$ is therefore

$$G'(t') = \frac{\tau'_{yx}(t')}{\gamma_0} = G_0 \left(\frac{t'}{\lambda}\right)^{\alpha-\beta} E_{\alpha,\alpha-\beta+1} \left(-\left(\frac{t'}{\lambda}\right)^\alpha\right). \quad (3.18)$$

The asymptotes of the relaxation modulus for short and long times exhibit power-law behaviors as shown in the following table,

$G'(t')$	$0 < \alpha < 1, \beta = 1$	$0 < \alpha < \beta < 1$
$t' \rightarrow 0$	$G'(t') \rightarrow \frac{G_0}{\Gamma(\alpha)} \left(\frac{t'}{\lambda}\right)^{\alpha-1}$	$G'(t') \rightarrow \frac{G_0}{\Gamma(1+\alpha-\beta)} \left(\frac{t'}{\lambda}\right)^{\alpha-\beta}$
$t' \rightarrow \infty$	$G'(t') \rightarrow \frac{-G_0}{\Gamma(-\alpha)} \left(\frac{t'}{\lambda}\right)^{-1-\alpha}$	$G'(t') \rightarrow \frac{G_0}{\Gamma(1-\beta)} \left(\frac{t'}{\lambda}\right)^{-\beta}$

If $\alpha = \beta = 1$, the relaxation modulus is exponential $G'(t') = G_0 \exp(-t'/\lambda)$. When $0 < \alpha = \beta < 1$, the relaxation modulus, is a one-parameter Mittag-Leffler function $G'(t') = G_0 E_{\alpha,1} \left(-\left(\frac{t'}{\lambda}\right)^\alpha\right)$ with an initial stretched-exponential behavior $G'(t') \sim \exp[-t'^\alpha / (\lambda^\alpha \Gamma(\alpha+1))]$ and a long time power-law asymptote $G'(t') \sim \Gamma(\alpha) \sin(\alpha\pi) t'^{-\alpha} / (\pi \lambda^\alpha)$ (Figure 3.1). The one-parameter Mittag-Leffler function $E_{a,1}(z)$ is sometimes denoted as $E_a(z)$.

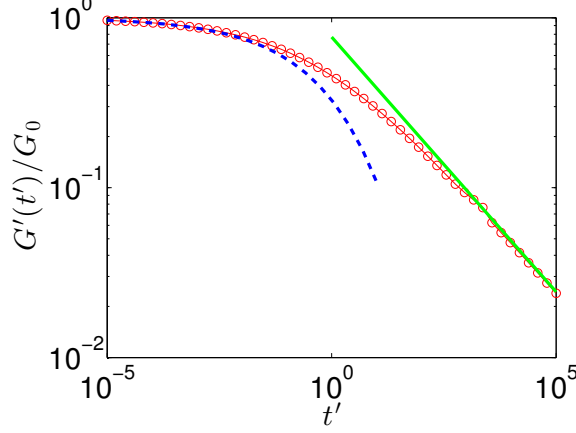


Figure 3.1: Stress relaxation after a step strain for the FMM (3.13), where $\lambda = 1$ and $\alpha = \beta = 0.3$ (red/circles). Initially, the decay asymptotes to a stretched-exponential function $G'(t') \sim \exp[-t'^{0.3}/(\lambda^{0.3}\Gamma(1.3))]$ (blue/dashed curve). For long times, the decay asymptotes to a power-law pattern $G'(t') \sim \Gamma(0.3) \sin(0.3\pi)t'^{-0.3}/(\pi\lambda^{0.3})$ (green/solid curve).

The complex modulus $G^*(\omega') = G'(\omega') + iG''(\omega')$ found by Fourier transforming the FMM model is given by

$$G^*(\omega') = \frac{G_0\lambda^\beta(i\omega')^\beta}{1 + G_0\lambda^\alpha(i\omega')^\alpha}. \quad (3.19)$$

The storage modulus and loss modulus can be obtained by evaluating the real and imaginary parts of the right hand side of the above equation

$$G'(\omega') = \frac{G_0\lambda^\beta\omega'^\beta (\cos(\frac{\pi}{2}\beta) + G_0\lambda^\alpha\omega'^\alpha \cos(\frac{\pi}{2}(\beta - \alpha)))}{1 + 2G_0\lambda^\alpha\omega'^\alpha \cos(\frac{\pi}{2}\alpha) + G_0^2\lambda^{2\alpha}\omega'^{2\alpha}}, \quad (3.20)$$

$$G''(\omega') = \frac{G_0\lambda^\beta\omega'^\beta (\sin(\frac{\pi}{2}\beta) + G_0\lambda^\alpha\omega'^\alpha \sin(\frac{\pi}{2}(\beta - \alpha)))}{1 + 2G_0\lambda^\alpha\omega'^\alpha \cos(\frac{\pi}{2}\alpha) + G_0^2\lambda^{2\alpha}\omega'^{2\alpha}}. \quad (3.21)$$

The asymptotes of $G'(\omega)$ and $G''(\omega)$ are listed in the following table,

$G'(\omega'), G''(\omega')$	$0 < \alpha < 1, \beta = 1$	$0 < \alpha < \beta < 1$
$\omega' \rightarrow 0$	$G'(\omega') \rightarrow \omega'^{\alpha+1}, G''(\omega') \rightarrow \omega'^\beta$	$G'(\omega') \rightarrow \omega'^\beta, G''(\omega') \rightarrow \omega'^\beta$
$\omega' \rightarrow \infty$	$G'(\omega') \rightarrow \omega'^{1-\alpha}, G''(\omega') \rightarrow \omega'^{1-\alpha}$	$G'(\omega') \rightarrow \omega'^{\beta-\alpha}, G''(\omega') \rightarrow \omega'^{\beta-\alpha}$

The storage and loss moduli predicted by the FMM model for $\alpha = \beta = 1$ (*left*) and $\alpha = \beta = 0.3$ (*right*) are compared in Figure 3.2.

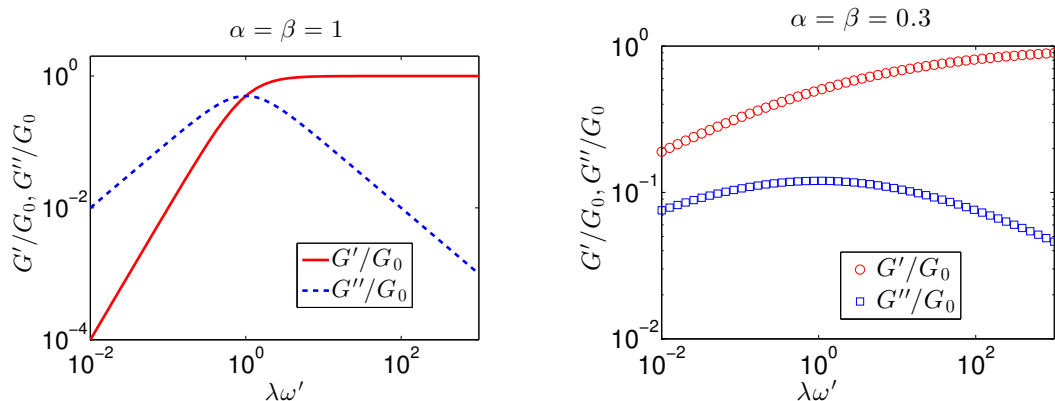


Figure 3.2: Left: $G'(\omega')$ (red/solid curve) and $G''(\omega')$ (blue/dashed curve) for $\alpha = \beta = 1$. Right: $G'(\omega')$ (red/circles) and $G''(\omega')$ (blue/squares) for $\alpha = \beta = 0.3$.

FMM thus can accurately model the complex relaxation behavior exhibited by bulk materials as well as the elastic modulus and loss modulus behavior. The limitation of this model is that it only describes the fluid dynamics in the linear viscoelastic limit and cannot be easily modified to describe non-linear viscoelastic behavior.

3.2.3 Generalized Tensorial Fractional Maxwell Model

Yang [38] proposed a tensorial formulation of the generalized scalar fractional Maxwell model. In this model, the fractional derivative acts on the convected components of the stress tensor to ensure the model is frame-invariant, and thus the model can be applied to flows with large strains. The model equation is:

$$\boldsymbol{\tau}'_{[0]'} + \lambda^\alpha {}^C D_{t'}^\alpha \boldsymbol{\tau}'_{[0]'} = G_0 \lambda^\beta {}^C D_{t'}^\beta \boldsymbol{\gamma}'_{[0]'}, \quad (3.22)$$

with initial conditions $\boldsymbol{\tau}'_{[0]'}|_{t' \leq 0} = 0$, $\boldsymbol{\gamma}'_{[0]'}|_{t' \leq 0} = 0$. Here the relative strain tensor is

$$\boldsymbol{\gamma}'_{[0]'}(\mathbf{r}', t', t'_s) = \mathbf{I} - \mathbf{E}' \cdot \mathbf{E}'^{t'}, \quad (3.23)$$

where $\gamma'_{[0]'}$ is a function of past time t'_s by following a particle with position \mathbf{r}' at time t' . For small displacement gradients, $\gamma'_{[0]'}$ reduces to strain tensor γ' . The relative displacement gradient tensor $\mathbf{E}'(\mathbf{r}', t', t'_s)$ under steady-shear flow is

$$\mathbf{E}'(\mathbf{r}', t', t'_s) = \begin{pmatrix} 1 & (t' - t'_s)\dot{\gamma}'_{yx} & 0 \\ 0 & 1 & 0 \\ 0 & 0 & 0 \end{pmatrix}. \quad (3.24)$$

The relative stress tensor is

$$\boldsymbol{\tau}'_{[0]' }(\mathbf{r}', t', t'_s) = \mathbf{E}' \cdot \boldsymbol{\tau}' \cdot \mathbf{E}'^t. \quad (3.25)$$

Here, we have

$${}_0^C D_{t'}^\alpha \boldsymbol{\tau}'_{[0]' } = \frac{1}{\Gamma(1-\alpha)} \int_0^{t'} (t' - s)^{-\alpha} \boldsymbol{\tau}'_{[1]' }(s) ds, \quad (3.26)$$

where

$$\boldsymbol{\tau}'_{[1]' }(\mathbf{r}', t', t'_s) = \mathbf{E}' \cdot \boldsymbol{\tau}'_{(1)} \cdot \mathbf{E}'^t. \quad (3.27)$$

When $\alpha = \beta = 1$, this model reduces to the UCM model. This model can be solved exactly by Laplace transform [27],

$$\boldsymbol{\tau}'_{[0]' }(t') = E \int_0^{t'} \left(\frac{t' - s}{\lambda} \right)^{\alpha-\beta} E_{\alpha, \alpha-\beta+1} \left[- \left(\frac{t' - s}{\lambda} \right)^\alpha \right] \boldsymbol{\gamma}'_{[1]' }(s) ds, \quad (3.28)$$

where $\boldsymbol{\gamma}'_{[1]' } = \mathbf{E} \cdot \dot{\boldsymbol{\gamma}}' \cdot \mathbf{E}'^t$. The relaxation modulus is

$$G'(t') = G_0 \left(\frac{t'}{\lambda} \right)^{\alpha-\beta} E_{\alpha, \alpha-\beta+1} \left[- \left(\frac{t'}{\lambda} \right)^\alpha \right]. \quad (3.29)$$

Under simple shear flow, $\dot{\gamma}'_{yx} = \dot{\gamma}'$, the stress components can be obtained explicitly:

$$\tau'_{xx} = 2G_0 \int_0^{t'} \left(\frac{t' - s}{\lambda} \right)^{\alpha-\beta} E_{\alpha, \alpha-\beta+1} \left(- \left(\frac{t' - s}{\lambda} \right)^\alpha \right) \dot{\gamma}'^2 (t' - s) ds, \quad (3.30)$$

$$\tau'_{yx} = G_0 \int_0^{t'} \left(\frac{t' - s}{\lambda} \right)^{\alpha-\beta} E_{\alpha, \alpha-\beta+1} \left(- \left(\frac{t' - s}{\lambda} \right)^\alpha \right) \dot{\gamma}' ds. \quad (3.31)$$

The first normal stress difference $N'_1 = \tau'_{xx}$, since $\tau'_{yy} = 0$, and this model predicts a zero second normal stress. For $\beta = 1$, the shear stress for different α is shown in

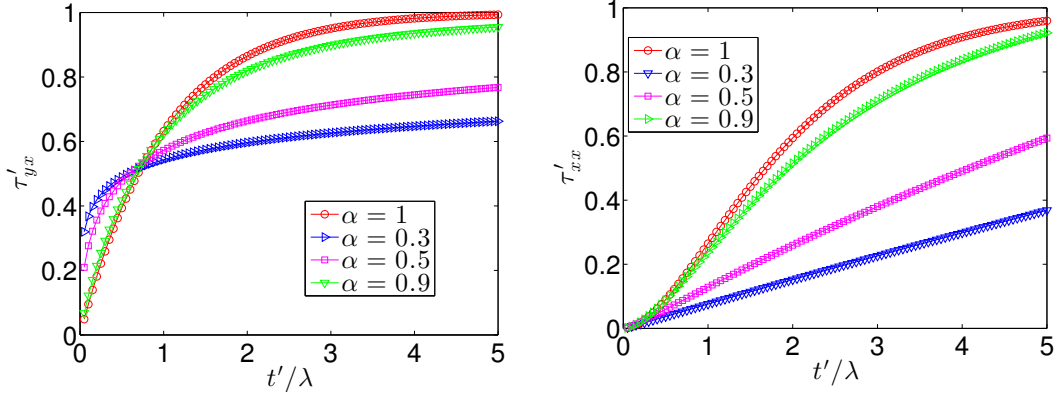


Figure 3.3: The time evolution of τ'_{xy} (*left*) and τ'_{xx} (*right*) under simple shear flow with $\dot{\gamma}'_{yx} = 1$ for the tensorial fractional Maxwell model for $\alpha = 1, 0.9, 0.5$ and 0.3 , $\beta = 1$.

Figure 3.3 (*left*) and the first normal stress difference is shown in Figure 3.3 (*right*). As t increases, the shear stress slowly approaches to steady-state and the growth is slower with a smaller α . As opposed to Yang’s claim, otherwise, the first normal stress difference predicted by this model does not reach a steady-state solution for $0 < \alpha < 1$.

Fractional constitutive models are successful in predicting some experimental observations of soft material systems. However, it is difficult to relate these fractional constitutive models (macroscale models) with the anomalous relaxation and diffusion behaviors of these soft materials (mesoscale dynamics). Rather than using this phenomenological approach, we will consider the system as a transient network at the mesoscale and simulate the equilibrium and dynamic behaviors of soft materials stochastically in Chapter 5. The connection of our proposed stochastic simulation for capturing non-exponential stress relaxation dynamics and their anticipated fractional equivalent models will also be presented in Chapter 5.

3.3 Cates Reptation Model

de Gennes [6] proposed that the neighboring chains of an entangled system make a test chain behave as if it is confined to a tube. Thus, the test chain only relaxes by a snake-like motion along its backbone, that is, within the containing tube. This motion

is called reptation.

For a chain of length L , the fundamental reptation relaxation time is

$$\lambda_L = L^3/D_0, \quad (3.32)$$

where D_0 is the mobility constant, independent of L [4]. Under the reptation hypothesis, Doi and Edwards [8] proposed that, after imposing an infinitesimal stress at time $t = 0$, the stress relaxation $\tau(t)$ of strands of length L in equilibrium conditions equals the average fraction of tube remaining at time t ,

$$\tau(t) = \frac{8}{\pi^2} \sum_{p=\text{odd}} \frac{1}{p^2} \exp\left(-\frac{p^2 t}{T_d}\right), \quad (3.33)$$

where $T_d = L^3/D_0\pi^2$ [8].

Cates [4] developed a theoretical study on the stress relaxation behavior of entangled wormlike micelles assuming the relaxation time is correlated with two fundamental time scales in the system, the reptation time of a chain of mean length $\lambda_{\text{rep}} = \bar{L}^3/D_0$ and the mean time for such a chain to break into two pieces λ_{break} . Here \bar{L} is the mean length for a system of strands. He predicted different characteristic relaxation time scales depending on the relative size of λ_{rep} and λ_{break} . In the pure reptation limit $\lambda_{\text{rep}} \ll \lambda_{\text{break}}$, the breakage and recombination times are long and the characteristic system relaxation time is then $\lambda = \lambda_{\text{rep}}$. In the fast-breaking limit $\lambda_{\text{break}} \ll \lambda_{\text{rep}}$, the chains are constantly breaking and the system relaxation time is given by $\lambda = \sqrt{\lambda_{\text{break}}\lambda_{\text{rep}}}$. The relaxation behaviors derived for these two regimes differ, with a stretched-exponential pattern predicted in the pure reptation case and a mono-exponential decay in the fast-breaking case. These behaviors have been observed experimentally [13, 28, 29].

3.3.1 Kinetics of Breaking and Recombination

In Cates reptation model [4], it is assumed that a chain can break with a fixed probability per unit time per unit length anywhere along its length L (L is a continuous variable and $L > 0$). Furthermore, the reforming rate is proportional to the product of

the concentrations of the two reacting subchains and is independent of the molecular weights of the chains. The time evolution of the number density $N(L)dL$ of chains with length $L \pm 1/2dL$ follows

$$\begin{aligned} \frac{dN(L)}{dt} = & -c_1LN(L) - c_2N(L) \int_0^\infty N(L_1)dL_1 + 2c_1 \int_L^\infty N(L_1)dL_1 \\ & + c_2 \int_0^\infty \int_0^\infty N(L_1)N(L_2)\delta(L_1 + L_2 - L)dL_1dL_2, \end{aligned} \quad (3.34)$$

where dL is an infinitesimal length. The parameters c_1 and c_2 are rate constants for the breakage and recombination processes, respectively. The first term represents the decrease in $N(L)$ by breakage; the second term is the decrease of $N(L)$ by the reaction of chains of length L with others to form longer chains; the third is the creation of chains of length L by breakage of longer chains; and the fourth term is creation of chains of length L by recombination of two shorter chains. The steady state solution of the above equation is

$$N(L) = 2c_1/c_2 \exp(-L/\bar{L}), \quad (3.35)$$

where the mean length \bar{L} depends on the ratio of the breakage and reforming rates and the concentration of polymers $\rho = \int_0^\infty LN(L)dL$:

$$2\bar{L}^2 = \rho c_2/c_1. \quad (3.36)$$

The characteristic breakage time is defined as [4]

$$\lambda_{\text{break}} = 1/(c_1\bar{L}). \quad (3.37)$$

3.3.2 Dynamics of Stress Relaxation

In equilibrium, the lengths of all the chains in the Cates system follow an exponential distribution as in equation (3.35) [4]. Here we non-dimensionalize chain lengths L by \bar{L} , where \bar{L} is the mean length of all the chains. In a small time interval dt , a chain of length L can break in any small interval dL along its length, with the probability c_1dLdt . In the mean time, it can join with another chain of length $L_1 \pm dL$ at either of its ends, each with the probability $c_1 \exp(-L_1)dLdt/2$. Initially, the lengths to the left

of the particle L_{left} and to the right L_{right} are generated from an exponential distribution. The absorbing walls at the two ends of the line segment can make jumps which represent the breakage and recombination processes. During a small time interval dt , the chains also have equal probability to diffuse to the left or right by step length $\Delta = \sqrt{2D_0 dt/L(t)}$. The stress carried by the chain goes away in both reptation and breakage/recombination. If one end of the chain diffuses outside the tube, the stress carried by that portion of the chain will relax right away. Also, if a chain breaks into shorter chains, the stress will relax during this process.

3.3.2.1 Pure Reptation

In the pure reptation limit, where $\lambda_{\text{break}} \rightarrow \infty$, the chains can only diffuse through reptation to the left or right; breakage/recombination events rarely happen on this time scale (of reptation motion). The stress relaxation, obtained for the system of chains with exponential length distribution (3.35) corresponding to the chains still in a tube is

$$\begin{aligned}\tau(t) &= \int_0^\infty L \exp(-L) \tau(L, t) dL \\ &= \int_0^\infty L \exp(-L) \frac{8}{\pi^2} \sum_{p=\text{odd}} \frac{1}{p^2} \exp\left(-\frac{tp^2}{T_d(L)}\right) dL.\end{aligned}\tag{3.38}$$

The first term of the series dominates the value of the stress. To reproduce the analysis of the asymptotic behavior of the stress tensor as proposed in [4], we perform steepest descent analysis on the weighted integral of the first term of the integral $\tau_1(t)$ to obtain the asymptotic behavior of stress relaxation as $t \rightarrow \infty$. Note,

$$\tau_1(t) = \frac{8}{\pi^2} \int_0^\infty L \exp\left(-L - \frac{tD_0\pi^2}{L^3}\right) dL.\tag{3.39}$$

Let $a = tD_0\pi^2$ and $f(L) = -L - \frac{a}{L^3}$. Then $f'(L) = -1 + 3aL^{-4}$, $f''(L) = -12aL^{-5}$. The minimum of $f(L)$ is at $L_0 = (3a)^{1/4}$ with $L = SL_0$. Thus, we obtain

$$\begin{aligned}
\tau_1(t) &= \frac{8}{\pi^2} \int_0^\infty SL_0 \exp\left(-SL_0 - \frac{a}{S^3 L_0^3}\right) L_0 dS \\
&= \frac{8}{\pi^2} \int_0^\infty SL_0^2 \exp\left(-L_0 \left[S + \frac{1}{3S^3}\right]\right) dS.
\end{aligned} \tag{3.40}$$

Let $\phi(S) = S + 1/(3S^3)$, $\phi'(S) = 1 - S^{-4}$, and $\phi''(S) = 4S^{-5}$. $\phi'(S_0) = 0 \Rightarrow S_0 = 1$. Thus, according to the steepest descent method, the asymptotic behavior of $\tau_1(t)$ for large t is

$$\begin{aligned}
\tau_1(t) &\sim \frac{8}{\pi^2} \frac{\sqrt{2} S_0 L_0^2 \exp(L_0[-S_0 - 1/(3S_0)])}{\sqrt{-(-L_0)\phi''(S_0)}} \int_{-\infty}^\infty e^{-s^2} ds, \quad t \rightarrow \infty \\
&= (3a)^{1/2} \frac{\sqrt{2\pi} \exp(-(3a)^{1/4} 4/3)}{\sqrt{4(3a)^{1/4}}} \\
&= \frac{8}{\pi^2} [t/(3D_0\pi^2)^{-1}]^{3/8} \exp\left(-\frac{4}{3}[t/(3D_0\pi^2)^{-1}]^{1/4}\right) \sqrt{\frac{\pi}{2}}.
\end{aligned} \tag{3.41}$$

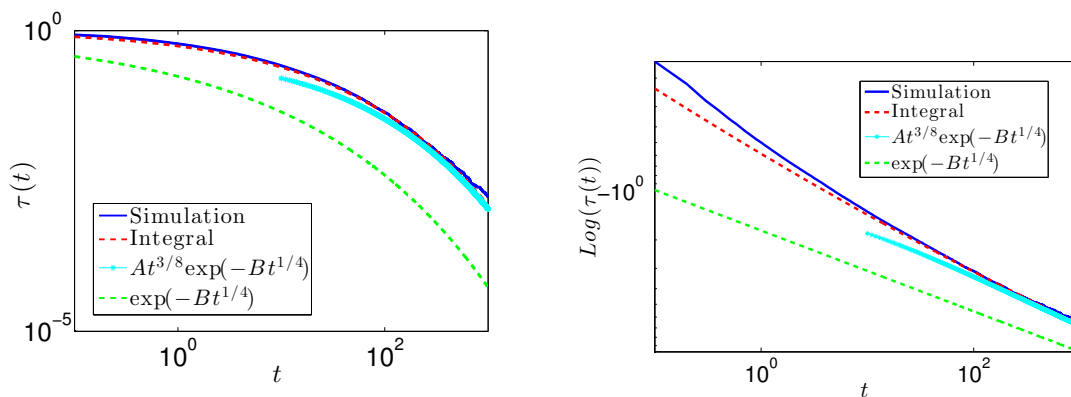


Figure 3.4: In the pure reptation, the stress relaxation for a system of chains with exponential length distribution is simulated stochastically and compared with asymptotic studies. In the long-time limit, the stress decay asymptotes to a stretched-exponential function. The left figure plots $\tau(t)$ as a function of t and the right figure plots $\log(\tau(t))$ as a function of t . Here, $A = 8/\pi^2(3D_0\pi)^{3/8}\sqrt{\pi/2}$, $B = 4/3(3D_0\pi^2)^{1/4}$, and $D_0 = 0.01$.

To simulate the full time evolution of this model as Cates [4], we considered $N = 5 \times 10^4$ chains with their initial lengths distributed according to (3.35) and

allowed each chain to diffuse to the left or right with parameter $D_0 = 0.01$. The stress of the system is determined through the fraction of chains remaining inside the tube [8]. In Figure 3.4 *left*, the stress decay obtained from simulation is compared with the numerical approximation of the full analytical integral, the asymptotic form, and the stretched-exponential function itself, in a log-linear plot. The simulations verify that for large times, the decay asymptotes to the stretched-exponential function.

3.3.2.2 Reptation and Kinetics of Breakage and Recombination

Let $\zeta = \lambda_{\text{break}}/\lambda_{\text{rep}}$ and $\lambda_{\text{rep}} = 1/D_0$, the fundamental relaxation time λ is dependent on both time scales λ_{break} and λ_{rep} ,

$$\lambda = \eta/G_0 = f(\zeta)\lambda_{\text{rep}}. \quad (3.42)$$

We choose a representative set of values of parameter ζ varying from 0.005 to 3100 (this range is enough to be representative of different regimes) and simulate the dynamics of the ensemble of 5×10^4 chains. The chains can break and reform, and diffuse, independently. The system relaxation time λ can be computed by integrating the stress decay function $\lambda = \int_0^\infty \tau(t)dt$ for each ζ , thus we can obtain λ and f as a function of ζ . When $\zeta \ll 1$, $f(\zeta) \sim \zeta^{1/2}$ and the system relaxation time $\lambda \sim \sqrt{\lambda_{\text{break}}\lambda_{\text{rep}}}$. For $\zeta \gg 1$, the system relaxation time $\lambda \sim \lambda_{\text{rep}}$ and f is close to a constant value. The function $f(\zeta)$ against ζ is plotted in Figure 3.5.

The stress decay $\tau(t)$ is plotted against time in Figure 3.6 *left*. When $\zeta = 0.01$, the breakage time scale is much smaller than the reptation time scale and the system is in the fast-breaking limit. The chains break and reform frequently and reptation happens much less often. The stress decay in this case shows an exponential behavior. When $\zeta = 1$, the breakage time is on the same scale as the reptation and $\tau(t)$ is non-exponential (the stress decay $\log(\tau(t))$ plotted against t exhibits a non-linear curve). When $\zeta = 3100$, the system is approaching the pure reptation limit, in which the chains rarely break/reform and experience mostly reptation motion.

By examining the relaxation dynamics of living polymers using a stochastic approach, Cates [4] suggested that the stress decay is exponential in the rapid breaking

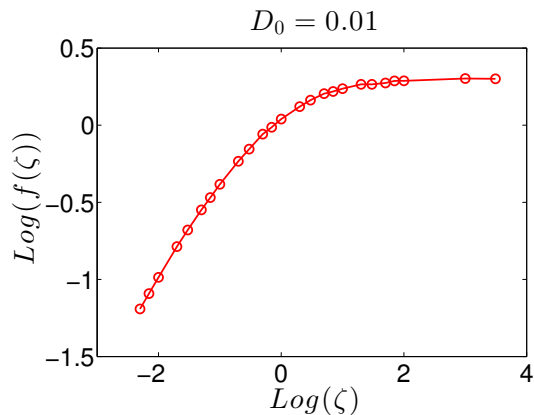


Figure 3.5: Plot of $f(\zeta)$ as a function of ζ . For $\zeta \ll 1$, $f(\zeta) \sim \zeta^{1/2}$. For $\zeta \gg 1$, $f(\zeta)$ is close to a constant. Here $D_0 = 0.01$

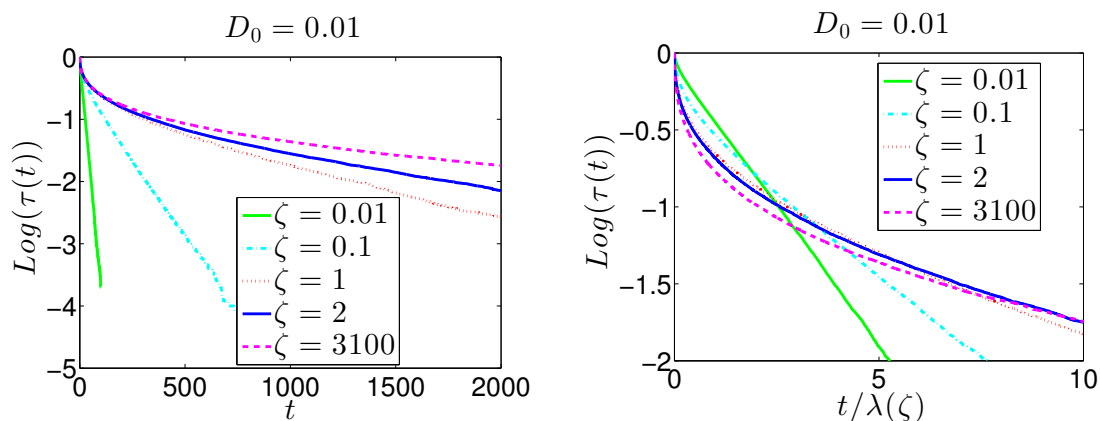


Figure 3.6: Left: Stress relaxation $\tau(t)$ against t for the Cates reptation model, with $D_0 = 0.01$ for various ζ . Right: Stress relaxation $\tau(t)$ against scaled time $t/\lambda(\zeta)$ for the Cates reptation model, with $D_0 = 0.01$ for various ζ . For ζ small, the decay is almost purely exponential, whereas for large ζ , it is much more disperse. Right: We rescale the time axis by the system relaxation time $\lambda(\zeta)$ for each ζ and compare the relaxation dynamics.

limit and the decay asymptotes to a stretched-exponential in the long-time limit when relaxation occurs only by curvilinear diffusion (pure reptation). In his work, it is shown theoretically that the stress relaxation asymptotes to a stretched-exponential behavior for $t \rightarrow \infty$ in the pure reptation regime. This non-exponential behavior results from the polydispersity of the chains, which leads to a spectrum of relaxation time scales

in the system. This finding is consistent with experimental observations of many soft material systems, e.g. CPyCl/NaSal solution. However, this model is limited to one-dimensional case and equilibrium conditions. It is challenging to extend this model to investigate the fluid dynamics under different flow conditions. Later, in Chapter 5, a mesoscale stochastic approach (transient network model) is employed to simulate the fluid dynamics of soft materials under shearing flow. To capture the broad spectrum of relaxation times, the breakage/recombination processes are simulated using a heavy-tail waiting time distribution and stochastic simulation predicts a non-exponential stress relaxation behavior.

Chapter 4

1-D FRACTIONAL KINETICS SIMULATED BY CONTINUOUS TIME RANDOM WALK (CTRW) AND SUBORDINATION

In Chapter 3, two approaches to model soft gel-like materials were presented, fractional constitutive models and Cates reptation model. While these two approaches successfully predicted observed non-exponential (power-law or stretched-exponential) stress decay after a small strain, the fractional constitutive models have the limitation of not connecting directly to the underlying physics of the system, and the Cates reptation model is an equilibrium model which is difficult to formulate in flow conditions.

Complex systems which exhibit anomalous diffusion and non-exponential relaxation dynamics can be described by fractional diffusion equation, fractional diffusion-advection equation, and fractional Fokker-Planck equation in the long-time limit [20]. In these models, the probability density distribution function (pdf) $\psi(x, t)$ of particles with position x at time t is described by partial differential equations (PDEs) and, for simple cases, the exact solution can be obtained. These models have been extensively studied and recognized as important tools in the description of anomalous transport processes in both the absence and the presence of external velocity or force fields [20].

In this chapter, several types of fractional kinetic models introduced in [20] are reviewed. The Monte Carlo simulations for the fractional diffusion equation using continuous time random walk (CTRW) and subordination are provided by [10, 17]. We will extend the stochastic processes described by the fractional diffusion equation to include the external velocity or force fields. The analysis in this chapter is restricted to the one-dimensional case. The main goal of this chapter is to test the Monte Carlo simulation algorithms for one-dimensional particle dynamics undergoing CTRW or subordinated processes. This test sets a foundation to simulate the three-dimensional

fluid dynamics of soft material systems stochastically in Chapter 5. In this chapter, all variables are dimensional and we leave out the prime notation, $()'$.

4.1 Anomalous Diffusion

Anomalous diffusion occurs in a multitude of systems, and is typified by the mean-squared displacement of a particle being a non-linear function of time $\langle \Delta r^2 \rangle \sim t^\beta, \beta \neq 1$ [20]. The anomalous diffusion exponent β determines whether the process will be categorized as subdiffusive, if $0 < \beta < 1$, or superdiffusive, if $\beta > 1$. The mean-squared displacement of tracer particles in soft materials has been measured using microrheology and subdiffusive behavior has been observed [16]. The Laplace transform of $\langle \Delta r^2(t) \rangle$ is related to the Laplace transform of the temporal relaxation of the stress for a soft material through the generalized Stokes-Einstein equation

$$\hat{G}(s) = \frac{k_B T}{\pi a s \langle \Delta \hat{r}^2(s) \rangle}, \quad (4.1)$$

where k_B is the Boltzmann's constant, T is the temperature, and a is the radius of the spherical tracer particle [18]. This subdiffusive behavior reflects a power-law stress decay behavior $G(t) \sim G_0 t^{-\beta}, 0 < \beta < 1$.

4.2 Fractional Diffusion with/without External Velocity or Force Fields

For a collection of particles undergoing standard diffusion, the time evolution of the probability distribution function (pdf) of their positions can be described by a diffusion equation. A consistent generalization of the diffusion equation to model physical systems with subdiffusive behavior is given by,

$$\frac{\partial \psi(x, t)}{\partial t} = {}_0^C D_t^{1-\beta} K_\beta \frac{\partial^2}{\partial x^2} \psi(x, t), \quad 0 < \beta < 1, \quad (4.2)$$

where ${}_0^C D_t^{1-\beta}$ is the Caputo fractional derivative of order $1 - \beta$ and $\psi(x, t)$ is the pdf of finding a particle at position x at time t [10]. Here K_β is the generalized diffusion constant with dimension $[K_\beta] = \text{m}^2 \text{s}^{-\beta}$ [20]. If we integrate the equation (4.2) by ${}_0^C D_t^{\beta-1}$, we can see that the time derivative is generalized to a fractional-order temporal

derivative and the second-order spatial derivative remains unchanged. When $\beta = 1$, this fractional diffusion equation is the regular diffusion equation. By taking the second moment of equation (4.2), it is shown that the mean-squared displacement of particles whose pdf is represented by $\psi(x, t)$ follows a power-law in time for $0 < \beta < 1$ (as opposed to linear when $\beta = 1$) [20],

$$\langle x^2(t) \rangle = \frac{2K_\beta}{\Gamma(1 + \beta)} t^\beta. \quad (4.3)$$

Here $\langle x^2(t) \rangle$ is the ensemble average of the square of all particle positions at time t and $\langle x^2(t) \rangle = \int_{-\infty}^{\infty} \psi(x, t) x^2 dx$ [20]. For equation (4.2), the relaxation of single mode follows a Mittag-Leffler pattern

$$T_n(t) = E_\beta(-\lambda_{n,\beta} t^\beta). \quad (4.4)$$

$T_n(t)$ is obtained using separation of variables $\psi(x, t) = \sum_n X_n(x) T_n(t)$, where $\lambda_{n,\beta}$ is the n -th eigenvalue. Here $E_a(z)$ is the one-parameter Mittag-Leffler function defined as

$$E_a(z) = \sum_{k=0}^{\infty} \frac{z^k}{\Gamma(ak + 1)}. \quad (4.5)$$

For the initial condition $\psi_0(x) = \delta(x)$, the exact solution of equation (4.2) is given by [20]

$$\psi(x, t) = \frac{1}{\sqrt{4K_\beta t^\beta}} \sum_{n=0}^{\infty} \frac{(-1)^n}{n! \Gamma(1 - \beta[n + 1]/2)} \left(\frac{x^2}{K_\beta t^\beta} \right)^{n/2}. \quad (4.6)$$

When $\beta = 1$, this pdf reduces to Gaussian distribution:

$$\psi(x, t) = \frac{1}{\sqrt{4\pi K_1 t}} \exp\left(-\frac{x^2}{4K_1 t}\right). \quad (4.7)$$

Later on in the simulation, we let the diffusion coefficient $K_\beta = 1$. A different value of K_β means a scale transformation of space and/or time units [10].

Eventually, we are interested in modeling soft materials composed of bead-spring dumbbells in imposed shear flows. Thus, it is helpful for us to investigate subdiffusive process under the influence of an external velocity and a force field using one-dimensional particle system. The probability of a particle being at position x at

time t under the influence of a constant velocity is modeled through the following diffusion-advection equation,

$$\frac{\partial\psi(x,t)}{\partial t} = -v\frac{\partial\psi}{\partial x} + K_1\frac{\partial^2}{\partial x^2}\psi(x,t), \quad (4.8)$$

where the advective drift $v\partial\psi/\partial x$ is brought about by the external velocity field v , K_1 is the diffusion coefficient [20]. The explicit solution to the diffusion-advection equation (4.8) with an initial condition $\psi_0(x) = \delta(x)$ is obtained by shifting the Gaussian distribution (4.7),

$$\psi(x,t) = \frac{1}{\sqrt{4K_1\pi t}} \exp\left(-\frac{(x-vt)^2}{4K_1t}\right). \quad (4.9)$$

For the fractional analogue, two variants of the above diffusion-advection model (equation (4.8)) have been investigated by Metzler and Klafter [20]: a Galilean invariant of the diffusion-advection equation, and a non-Galilean invariant of the diffusion-advection equation. Galilean invariant is defined as the pdf being invariant under a transformation $x \rightarrow x - vt$. The Galilean invariant fractional diffusion-advection equation is given by

$$\frac{\partial\psi(x,t)}{\partial t} = -v\frac{\partial\psi}{\partial x} + {}_0^C D_t^{1-\beta} \left(K_\beta \frac{\partial^2}{\partial x^2} \psi(x,t) \right). \quad (4.10)$$

The mean-squared displacement of particles described by this equation is given by [20]

$$\langle x^2(t) \rangle = \frac{2K_\beta t^\beta}{\Gamma(1+\beta)} + v^2 t^2. \quad (4.11)$$

As pointed out in [20], we might also consider a non-Galilean invariant fractional diffusion-advection equation as given by

$$\frac{\partial\psi(x,t)}{\partial t} = {}_0^C D_t^{1-\beta} \left(-A_\beta v \frac{\partial\psi}{\partial x} + K_\beta \frac{\partial^2}{\partial x^2} \psi(x,t) \right), \quad (4.12)$$

where A_β is the generalized advection parameter and is of dimension $[A_\beta] = s^{1-\beta}$. We assume $A_\beta = 1$ for simplicity. The mean-squared displacement of particles is then given by [20]

$$\langle x^2(t) \rangle = \frac{2K_\beta t^\beta}{\Gamma(1+\beta)} + \frac{2v^2 t^{2\beta}}{\Gamma(1+2\beta)}. \quad (4.13)$$

When $\beta = 1$, equations (4.10) and (4.12) reduce to the standard diffusion-advection equation (4.8).

The Fokker-Planck equation describes particles diffusing under an external force field. The fractional Fokker-Planck equation is a generalization of the Fokker-Planck equation to describe anomalous diffusion in an external force field,

$$\frac{\partial \psi(x, t)}{\partial t} = {}_0^C D_t^{1-\beta} \left(\frac{\partial}{\partial x} \frac{V_x(x) \psi}{m \eta_\beta} + K_\beta \frac{\partial^2}{\partial x^2} \psi(x, t) \right), \quad (4.14)$$

where the force is related to the potential through $F(x) = -dV(x)/dx$. Here m is the mass of the particle and η_β is the generalized drag coefficient of dimension $[\eta_\beta] = s^{\beta-2}$ [20]. This fractional Fokker-Planck equation (4.14) is obtained by generalizing the standard Fokker-Planck equation by replacing the regular time derivative with a fractional time derivative, and it reduces to the standard Fokker-Planck equation when $\beta = 1$. In the force-free limit $V(x) = \text{const}$, the fractional Fokker-Planck equation (4.14) reduces to the fractional diffusion equation (4.2). When the potential field satisfies $V(x) = -vx$, $dV/dx = -v$ and $v = \text{const}$, equation (4.14) reduces to the non-Galilean invariant equation (4.12). With a harmonic potential $V(x) = \frac{1}{2}bx^2$, the external field exerts a restoring force $F(x) = -bx$ on the particle. In this case, the fractional Fokker-Planck equation is also referred to as the fractional Ornstein-Uhlenbeck process [33]. The stationary solution of equation (4.14) with $V(x) = \frac{1}{2}bx^2$ is given by the Boltzmann distribution $\psi_{st}(x) = 1/\sqrt{2\pi} \exp[-bx^2/(2m\eta_\beta K_\beta)]$. If a point source initial condition, $\psi_0(x) = \delta(x - 1)$, is considered, the probability distribution of a particle ensemble initially peaked at $x = 1$ will slowly relax towards Boltzmann equilibrium [33].

Instead of solving the PDE for $\psi(x, t)$ itself, we follow particle trajectories governed by stochastic dynamics that leads to the fractional differential equations in the long-time limit. Specifically, a large number of particle trajectories are generated and the histograms of the particle positions, at long times, are compared with those of the solution of the PDE, $\psi(x, t)$. The power-law relation of the particle mean-squared displacement is captured in the simulation. In the next section, we report on Monte Carlo simulation of particles undergoing CTRW with/without the influence of an external

velocity or an external force field and show that the CTRW predictions converge to the fractional equations in the long-time limit.

4.3 From Continuous Time Random Walk to Fractional Diffusion Equation

The CTRW model is one mathematical model to describe the subdiffusive dynamics. This model accounts for possible trapping events of the diffusing particles within the surrounding (networked) structure. A CTRW consists of a sequence of independent identically distributed (i.i.d.) random jumps ξ_i separated by i.i.d. random waiting times τ_i [10, 20]. Let t_n be the sum of the waiting times after n steps,

$$t_n = \sum_{i=1}^n \tau_i, \quad \tau_i \in \mathbf{R}_+, \quad (4.15)$$

then the position at time $t \in [t_n, t_{n+1})$ is given by

$$x(t) = \sum_{i=1}^n \xi_i, \quad \xi_i \in \mathbf{R}. \quad (4.16)$$

We consider an uncoupled situation in which the jump length and waiting time are independent random variables. With $\lambda(x)dx$ being the probability of a jump of length in the interval $(x, x + dx)$, and $w(t)dt$ being the probability of a waiting time in the interval $(t, t + dt)$, different types of uncoupled CTRW processes can be categorized as to whether the characteristic waiting time

$$T = \int_0^{\infty} tw(t) dt \quad (4.17)$$

and/or jump length variance

$$\Sigma^2 = \int_{-\infty}^{\infty} x^2 \lambda(x) dx \quad (4.18)$$

are finite or infinite, respectively [20].

If both T and Σ^2 are finite, this random walk model leads to normal diffusion in the long-time limit [20]. For example, if the waiting time pdf is Poissonian, $w(t) = \gamma_t^{-1} \exp(-t/\gamma_t)$, with the characteristic waiting time $T = \gamma_t$, and the jump length pdf is Gaussian, $\lambda(x) = (4\pi\gamma_x^2)^{-1/2} \exp(-x^2/(4\gamma_x^2))$, with the jump length variance

$\Sigma^2 = 2\gamma_x^2$, the random walk process is equivalent to a discrete one-dimensional random walk model, in which the random walker jumps with a fixed distance Δx to the left or right with equal probability at each time step Δt [20]. Here γ_t and γ_x are time and length scale parameters, respectively.

In many physical situations, the waiting times may be non-Poissonian due to obstacles and traps that delay the particle's jump [33]. When the characteristic waiting time T diverges, but the jump length variance Σ^2 is finite, the process is referred to as a fractal time random walk [20]. In this case, the waiting time distribution is heavy-tailed with an asymptotic behavior of

$$w(t) \sim (t/\gamma_t)^{-1-\beta}, \quad (4.19)$$

where $0 < \beta < 1$ [20, 33]. The CTRW with a heavy-tailed waiting time distribution and a Gaussian jump length pdf converges in the long-time limit to the fractional diffusion equation (4.2) [10, 20].

4.4 Monte Carlo Simulation of CTRW

As shown by Fulger et al [10], CTRW with random waiting times generated from the Mittag-Leffler distribution

$$w(t) = -\frac{d}{dt} E_\beta(-(t/\gamma_t)^\beta), \quad (4.20)$$

and jump lengths generated from the Gaussian distribution

$$\lambda(x) = (4\pi\gamma_x^2)^{-1/2} \exp(-x^2/(4\gamma_x^2)), \quad (4.21)$$

converges to the fractional diffusion equation (4.2) in the long-time limit. Here γ_t is a time scale parameter and $\gamma_x = \gamma_t^{\beta/2}$ is a length scale parameter. The mean for this waiting time distribution $T = \int_0^\infty tw(t)dt$ is infinite. It is challenging computationally to generate random waiting times which follow the distribution (4.20). According to [10], the random waiting times with the pdf (4.20) can be generated using the inversion formula,

$$t_i^\beta = -\gamma_t \ln u \left(\frac{\sin(\beta\pi)}{\tan(\beta\pi v)} - \cos(\beta\pi) \right)^{1/\beta}, \quad (4.22)$$

where $u, v \in (0, 1)$ are independent uniformly distributed random numbers, and t_i^β is the Mittag-Leffler random number. For $\beta = 1$, equation (4.22) reduces to the inversion formula for the exponential distribution $t_i = -\gamma_t \ln u$ and the cumulative distribution function (cdf) of the waiting times reduces to an exponential form $W(t) = \exp(-t/\gamma_t)$. To test this random number generator, $N = 10^4$ random numbers are generated using (4.22) and their cumulative distribution is compared with the exact cdf $W(t) = E_\beta(-(t/\gamma_t)^\beta)$ for $\gamma_t = 1$ and $\beta = 0.6$ (Figure 4.1). For $0 < \beta < 1$, $W(t)$ is approximated by a stretched-exponential function $W(t) \sim \exp(-t^\beta/\Gamma(\beta + 1))$ for short time $t \ll 1$. For larger time $t \gg 1$, $W(t)$ asymptotes to the power law pattern $W(t) \sim \Gamma(\beta) \sin(\beta\pi)t^{-\beta}/\pi$.

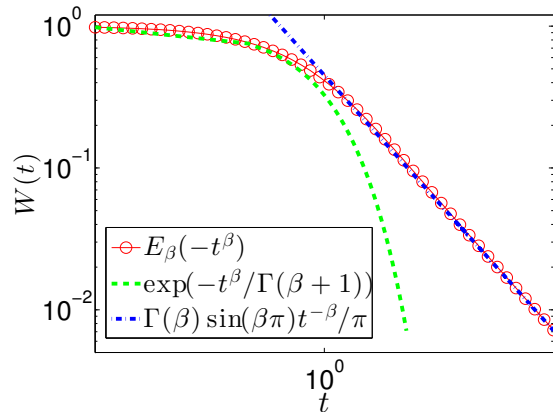


Figure 4.1: The complementary cumulative distribution function (cdf) $W(t)$ sampled using (4.22) with $\beta = 0.6$ and $\gamma_t = 1$ (red/circles), as well as its approximations for $t \rightarrow 0$ (stretched-exponential, green/dashes) and $t \rightarrow \infty$ (power-law, blue/dashes).

Jump lengths were generated using

$$\xi_i = 2\gamma_x \sqrt{-\ln u} \sin \phi, \quad (4.23)$$

where $\phi = \pi(v - 1/2)$ and the jumps scale parameter follows the relationship $\gamma_x = \gamma_t^{1/2}$. Here $u, v \in (0, 1)$ are independent uniform random numbers [10].

4.4.1 Standard Random Walks

When $\beta = 1$, the particles move with exponentially distributed waiting times and Gaussian distributed jump lengths. This standard random walk model describes particles undergoing Brownian motion and it asymptotes to the pdf (4.7) in the long-time limit. We carried out a Monte Carlo simulation for the standard random walk. A straightforward approach to check the asymptotic behavior of the random walk model is to simulate the process for a long time and compare the histogram of particle positions with the exact distribution. In order to more efficiently compare the asymptotic behavior of the random walk process with the exact distribution in a small time window, we rescale the process by letting $\gamma_t = 0.001$. The jump lengths are then rescaled so that $\gamma_x = \gamma_t^{1/2}$. This allows a choice of a short time period, for example $0 < t < 2$ for the observation. Samples of such particle trajectories are shown in Figure 4.2 *left*. The mean-squared displacement $\langle x^2(t) \rangle$ is then computed by taking the ensemble average of the square of $N = 2 \times 10^4$ particle positions, i.e. $\langle x^2(t) \rangle = \sum_{i=1}^N x_i^2(t)/N$ and is compared with the analytical form $\langle x^2(t) \rangle = 2K_1 t/\Gamma(2)$ (Figure 4.2 *right*). The simulation results match well with the analytical form. The histogram of the particle positions produced from stochastic simulations at $t = 2$ matches closely to the exact Gaussian distribution (4.7) (Figure 4.3).

4.4.2 CTRW with Infinite Mean Waiting Time

Simulations of CTRW with waiting times generated using (4.22) and jumps generated using (4.23) weakly asymptote to the exact pdf (4.6) [10]. Sample trajectories of particles for $0 < t < 2$ are produced in Figure 4.4 *left*. The jump lengths scale follows $\gamma_x = \gamma_t^{\beta/2}$, with $\gamma_t = 0.001$. The mean-squared displacement of the particle motions is computed and power-law dependence, $\langle x^2(t) \rangle \sim t^\beta$, is observed (Figure 4.4 *right*). For systems in which particles follow a waiting time distribution with a divergent mean between successive jumps, the particle occasionally gets trapped so that the jumps happen less often as compared to those of exponentially distributed waiting times. The histogram of particle positions for $\beta = 0.6$ and $\gamma_t = 0.001$ is compared with the

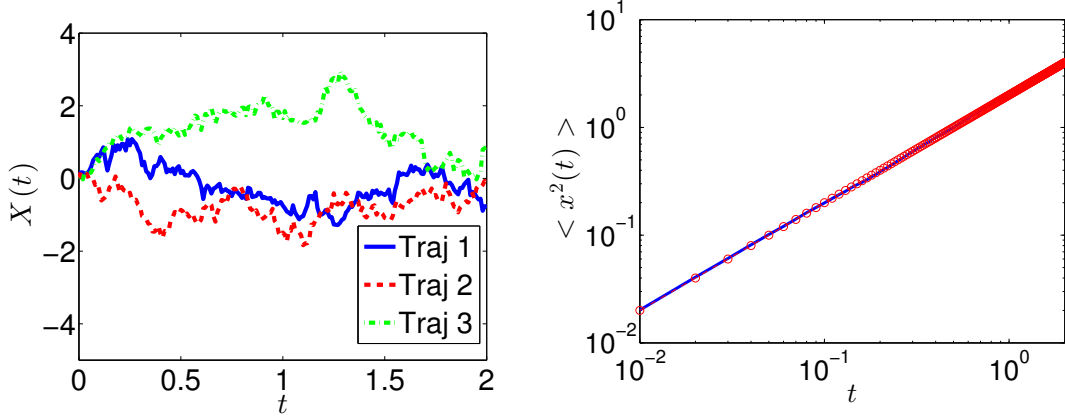


Figure 4.2: Left: Sample paths of random walks with exponentially distributed waiting times generated using (4.22) for $\beta = 1$ and Gaussian jumps generated using (4.23). Right: Comparison of simulation results of the ensemble average of the particle mean-squared displacements (*blue/solid curve*) with equation $\langle x^2(t) \rangle = 2K_1 t / \Gamma(2)$ formulated by taking the second moment of (4.2) (*red/circles*). Here $K_1 = 1$. The waiting times scale γ_t is set to 0.001, jump lengths are scaled by $\gamma_x = \gamma_t^{1/2}$.

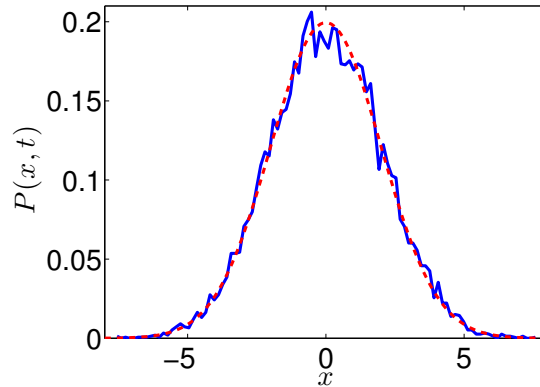


Figure 4.3: Comparison of the histogram of $N = 2 \times 10^4$ particle positions from a Monte Carlo simulation of random walks with $\gamma_t = 0.001$ (*blue/solid curve*), with the exact form (4.7), with $K_1 = 1$ (*red/dashed curve*) at $t = 2$.

exact result (equation (4.6)) in Figure 4.5. The simulation histogram matches well with that of the analytical form for $\gamma_t = 0.001$.

CTRW based models provide a more fundamental approach (than the fractional

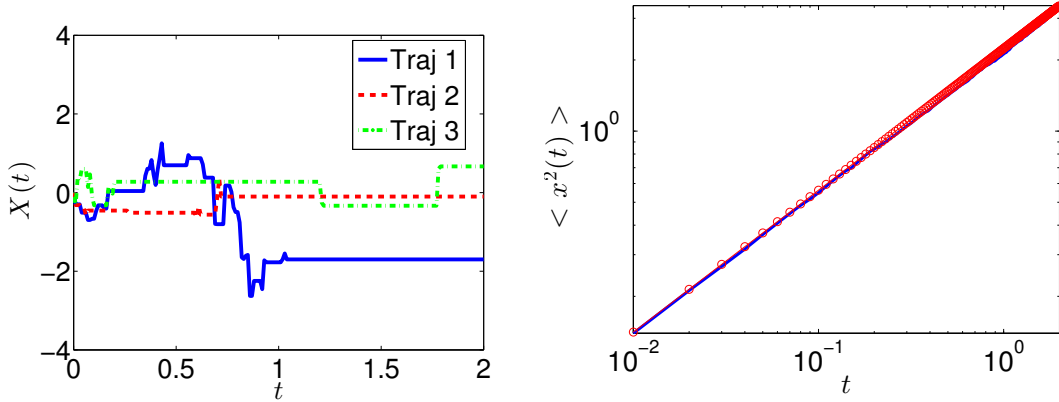


Figure 4.4: Left: Sample paths of CTRW with Mittag-Leffler distributed waiting times generated using (4.22) for $\beta = 0.6$ and Gaussian jumps generated using (4.23). Right: Comparison of simulation results of the ensemble average of the particle mean-squared displacements (*blue/solid curve*) with equation $\langle x^2(t) \rangle = 2K_\beta t^\beta / \Gamma(1 + \beta)$ formulated by taking the second moment of (4.2) (*red/circles*). Here $K_\beta = 1$. The waiting times scale γ_t is set to 0.001 and jump lengths are scaled by $\gamma_x = \gamma_t^{\beta/2}$.

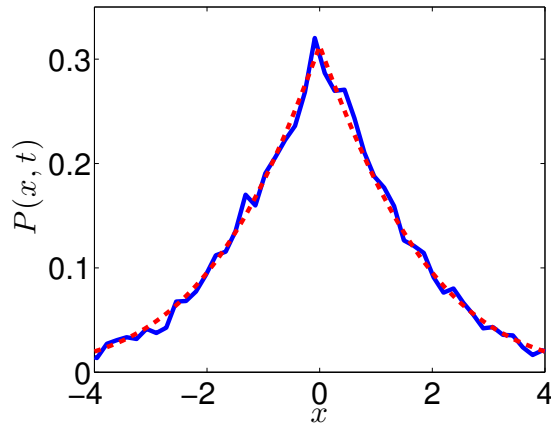


Figure 4.5: Comparison of the histogram of $N = 2 \times 10^4$ particle positions from a Monte Carlo simulation of CTRW for $\gamma_t = 0.001$ (*blue/solid curve*) with the exact form (4.6) (*red/dashed curve*) for $\beta = 0.6$, $K_\beta = 1$, at $t = 2$. The cusp shape of the pdf is a distinctive feature of a CTRW.

diffusion equation) to simulate subdiffusive processes and the resultant anomalous diffusion is then directly connected with the particle dynamics. By rescaling waiting times by a constant γ_t and jumps by a constant $\gamma_x = \gamma_t^{\beta/2}$ and letting γ_t vanish, it

can be shown that the histogram for the probability density $\psi(x, t)$ of finding position x at time t for the rescaled process converges to the exact pdf (4.6) of the fractional diffusion equation [10]. The histogram of particle positions exhibits a cusp shape for $0 < \beta < 1$ which is unique to the anomalous diffusion process [20]. The mean-squared displacement for particles whose trajectories are governed by a CTRW follows a power-law relation $\langle x^2(t) \rangle \sim t^\beta$. This simple CTRW model will be extended to three-dimensional models to capture the anomalous diffusion of soft material systems in the next chapter.

4.4.3 Galilean Invariant Case

In the previous section, we reported anomalous diffusion modeled by a CTRW. When the velocity field is present, for the Galilean invariant case, the jump length pdf $\lambda(x)$ is invariant under a transformation $x \rightarrow x - vt$. In this case, the CTRW consists of a sequence of independent random jumps ξ_i generated by (4.23) separated by random waiting times τ_i generated using (4.22). During the waiting time τ_i , the particle moves deterministically due to the velocity field. That is, during the time interval dt , the particles move according to the deterministic equation

$$dx = vdt. \quad (4.24)$$

The position of the particle at time $t \in [t_n, t_{n+1})$ is given by

$$x(t) = \sum_{i=1}^n \xi_i + vt_n, \quad (4.25)$$

where $t_n = \sum_{i=1}^n \tau_i$.

For $\beta = 1$ and $v = 10$ (Figure 4.6 left), the particles paths can be seen fluctuating randomly due to Brownian motion, and drifting with the velocity field. We use $v = 10$ in the simulation of sample particle trajectories to blow up the effect of the drift due to the external velocity field. Then we simulated $N = 10^4$ particle trajectories with random waiting times and jumps following (4.22) and (4.23) with motion described by equation (4.24). Here velocity $v = 1$. The mean-squared displacement was computed

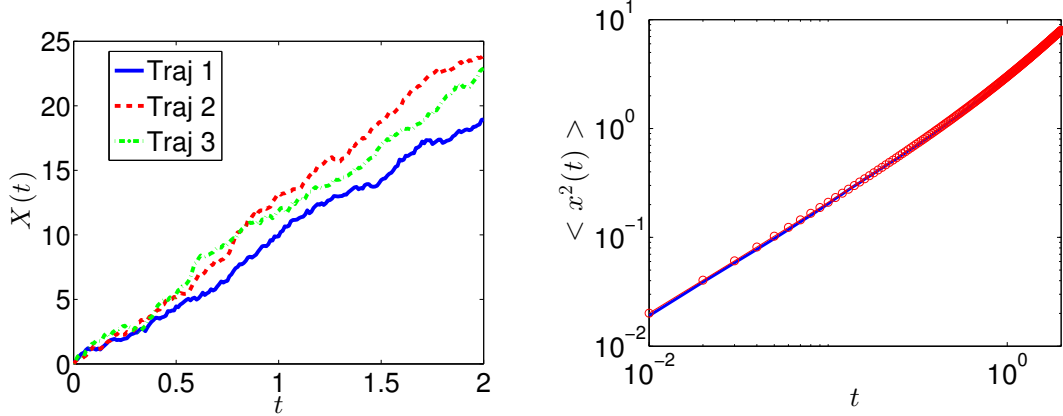


Figure 4.6: Left: Sample paths of particles experiencing Brownian motion and external velocity, where the particles move deterministically under an external velocity field and diffuse with Gaussian jumps generated using (4.23) and exponentially distributed waiting times generated using (4.22) for $\beta = 1$. Here with a $v = 10$, the particles drift under the influence of the velocity field. Right: Comparison of simulation results of the ensemble average of the particle mean-squared displacements (*blue/solid curve*) with equation $\langle x^2(t) \rangle = 2K_1t/\Gamma(2) + v^2t^2$ formulated by taking the second moment of (4.10) (*red/circles*). Here $\beta = 1$, $v = 1$ and $K_1 = 1$. The waiting times scale γ_t is set to 0.01 and jump lengths are scaled by $\gamma_x = \gamma_t^{1/2}$.

by taking the ensemble average of the square of all particle positions. That result is compared with the exact form $\langle x^2(t) \rangle = 2K_1t/\Gamma(2) + v^2t^2$ [20] (Figure 4.6 right). This mean-squared displacement of the particles consists of a linear contribution in time from the diffusion and a quadratic growth in time due to the velocity. The computed histogram of the particle positions produced from this stochastic process at $t = 2$ matches closely to the exact Gaussian distribution (4.9) as shown in Figure 4.7.

For a β in the range $0 < \beta < 1$, the particles drift deterministically with the velocity and subdiffuse with a Mittag-Leffler distributed waiting times. The particles exhibit Gaussian jumps less frequently than for $\beta = 1$ due to the heavy-tailed waiting time distribution (4.20) (Figure 4.8 left as compared with Figure 4.6 left). The mean-squared displacement of the particle motions $\langle x^2(t) \rangle = 2K_\beta t^\beta/\Gamma(1 + \beta) + v^2t^2$ has a power-law contribution from the subdiffusion and a quadratic contribution due to the velocity field (as in the previous case) (Figure 4.8 right). The histogram of particle

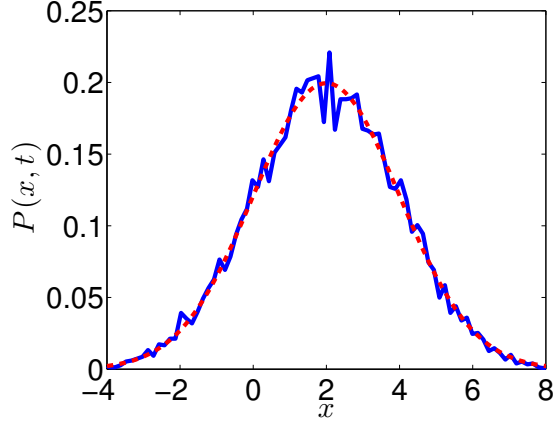


Figure 4.7: Comparison of the histogram of particle positions experiencing Brownian motion and drift, for $\gamma_t = 0.01$ (*blue/solid curve*) with the exact form (4.9) (*red/dashed curve*) for $\beta = 1$, $K_1 = 1$, $v = 1$, at $t = 2$.

positions at $t = 2$ exhibits a cusp shape (Figure 4.9) as opposed to the result for $\beta = 1$ (Figure 4.7).

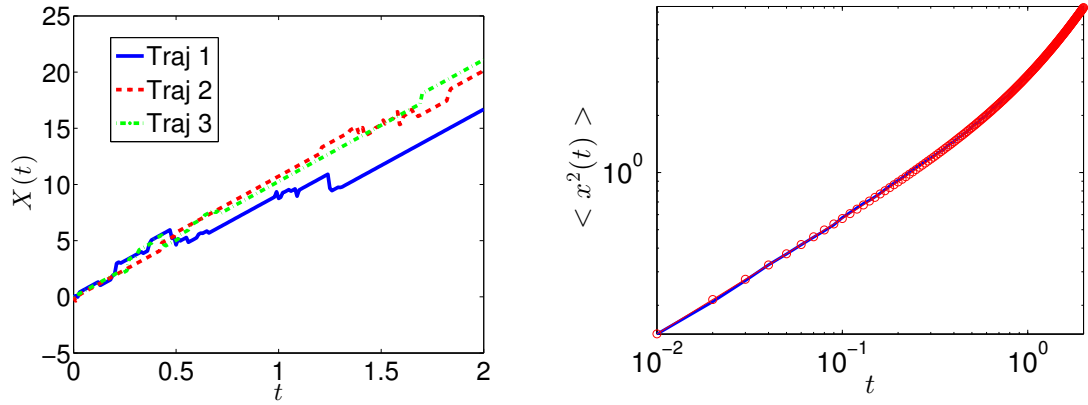


Figure 4.8: Left: Sample trajectories of particles moving on a CTRW under the influence of an external velocity field in the Galilean invariant case. Here $\beta = 0.6$, $v = 10$. Right: Comparison of simulation results of the ensemble average of the particle mean-squared displacements (*blue/solid curve*) with equation $\langle x^2(t) \rangle = 2K_\beta t^\beta / \Gamma(1+\beta) + v^2 t^2$ formulated by taking the second moment of (4.10) (*red/circles*). Here $\beta = 0.6$, $v = 1$ and $K_\beta = 1$. The waiting times scale γ_t is set to 0.01 and jump lengths are scaled by $\gamma_x = \gamma_t^{\beta/2}$.

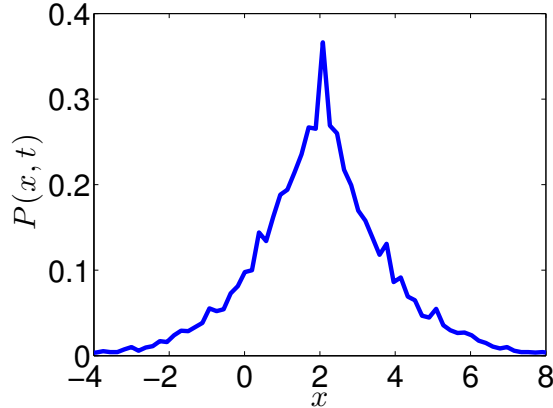


Figure 4.9: Plot of the histogram of particle positions experiencing subdiffusion and drift for the Galilean invariant case (*blue/solid curve*) for $\beta = 0.6$, $K_\beta = 1$, $v = 1$, $\gamma_t = 0.01$, at $t = 2$.

4.4.4 Non-Galilean Invariant Case

For a physical system in which the particle is repeatedly immobilized in the environment for a trapping time drawn from the waiting time pdf $w(t)$, before being dragged along with the velocity stream again, the resulting process is not Galilean invariant [20]. One way to envision this CTRW is to consider a sequence of independent random jumps ξ_i generated by (4.23) and shifting by distance $v\tau_i$ due to velocity field after a random waiting time τ_i generated using (4.22). In such a scenario, the particle gets trapped, and when it eventually jumps, it jumps forward to catch up with the moving fluid, i.e. the average jump length of the particles that were trapped for a time τ is $v\tau$. The position of the particle at time t_n is given by

$$x(t_n) = x(t_{n-1}) + \xi_n + v\tau_n, \quad (4.26)$$

where $t_n = \sum_{i=1}^n \tau_i$. This CTRW differs from that of the Galilean invariant case in that the particle, with position $x(t)$, does not move with the velocity during the waiting time τ_n for this proposed non-Galilean invariant case, while for the Galilean invariant case the particle continues moving deterministically during this waiting time with a velocity governed by the fluid.

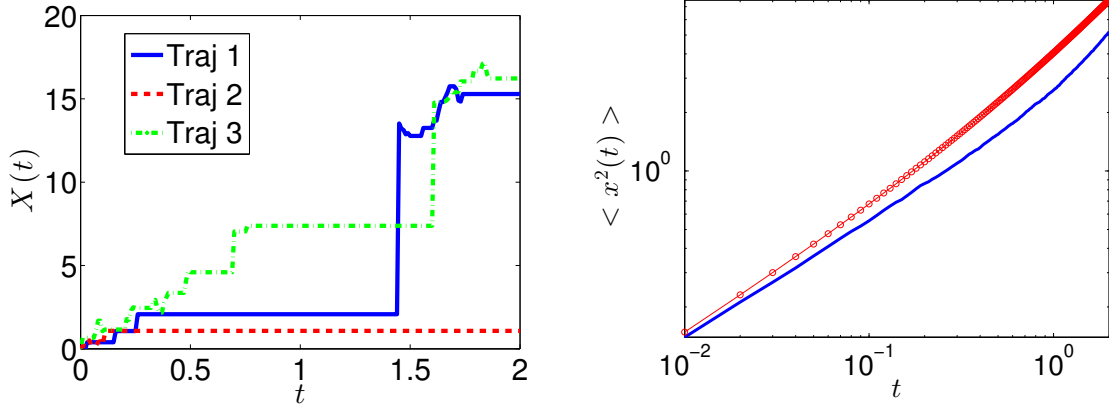


Figure 4.10: Left: Sample trajectories of particles moving on a CTRW under the influence of an external velocity field in the non-Galilean invariant case. Here $\beta = 0.6$, $v = 10$. Right: Comparison of simulation results of the ensemble average of the particle mean-squared displacements (*blue/solid curve*) with equation $\langle x^2(t) \rangle = \frac{2K_\beta t^\beta}{\Gamma(1+\beta)} + \frac{2v^2 t^{2\beta}}{\Gamma(1+2\beta)}$ formulated by taking the second moment of (4.12) (*red/circles*). Here $\beta = 0.6$, $v = 1$, and $K_\beta = 1$. The waiting time scale γ_t is set to 0.01 and jump lengths are scaled by $\gamma_x = \gamma_t^{\beta/2}$.

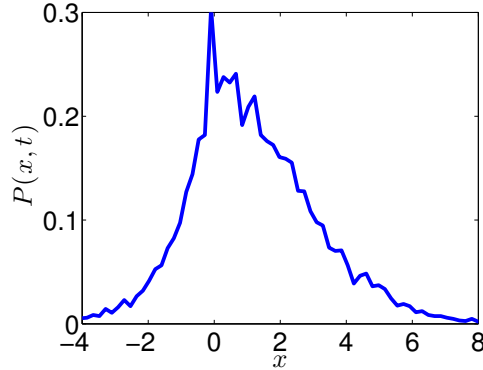


Figure 4.11: Plot of the histogram of the particle positions with a non-Galilean invariant velocity assumption from a simulation (*blue/solid curve*) for $\beta = 0.6$, $\gamma_t = 0.01$, $K_\beta = 1$, $v = 1$, at $t = 2$.

The particle trajectories for the proposed non-Galilean invariant case exhibit different dynamics than the Galilean invariant case (see Figure 4.10 left in which the velocity is $v = 10$ and $\beta = 0.6$). The simulated mean-squared displacement of particle

positions is compared with that of the equation $\langle x^2(t) \rangle = \frac{2K_\beta t^\beta}{\Gamma(1+\beta)} + \frac{2v^2 t^{2\beta}}{\Gamma(1+2\beta)}$ (which is equation (4.13) computed by taking the second moment of equation (4.12)) (Figure 4.10 *right*). This simulated particle mean-squared displacement has a slower growth in time as compared to that of equation (4.13). Further comparisons of the growth rate are shown in Figure 4.16, and the results are discussed in the next section. For the value $\beta = 0.6$, the histogram of particle positions exhibits a cusp shape as in the Galilean invariant case. As shown in Figure 4.11, the histogram is asymmetric with respect to the imposed velocity, $v = 1$. Equation (4.26) is one way to implement the non-Galilean invariant case using a CTRW and different algorithms can be developed to simulate the non-Galilean invariant model.

4.5 Subordination of Fractional Fokker-Planck Dynamics

Recent development of simulation techniques based on a Langevin equation in random subordinated time provides an efficient tool to study CTRW and the stochastic trajectories of anomalous diffusion [9]. In this section, this method, subordination, is introduced. The stochastic simulations are reproduced based on the algorithm developed in [17]. The subordination method has the advantage of being computationally efficient [17]. The resultant particle histograms from simulations match $\psi(x, t)$ from the fractional Fokker-Planck equation without the need to take the long-time limit as in the CTRW approach. In [17], it is shown that the stochastic process whose pdf obeys the dynamics of the fractional Fokker-Planck equation, can be identified as the subordination of two fundamental processes $X(S_t)$: the Langevin process $X(\tau)$ with an external force and standard Brownian motion formulated according to the Fokker-Planck equation, and the inverse-time β -stable subordinator S_t . Here τ is the internal time. The subordinator S_t is a new operational time of the system and relates the internal time τ and the observable time t . By allowing a random change of time of the system through the subordinator S_t , the subordination method captures the heavy-tailed characteristic of the waiting times between successive jumps of a particle. According to [17], the solution $\psi(x, t)$ of the fractional Fokker-Planck equation is equal

to the pdf $p(x, t)$ of the subordinated process $Y(t)$ obtained by a random change of time.

$$Y(t) = X(S_t). \quad (4.27)$$

The process $X(\tau)$ is the solution of the Langevin dynamics:

$$dX(\tau) = -V'(X(\tau))d\tau + \sqrt{2K_1}dW(\tau), \quad (4.28)$$

driven by standard Brownian motion $W(\tau)$. The subordinator S_t , called the inverse-time β -stable subordinator for $\beta \in (0, 1)$, is defined as

$$S_t = \inf\{\tau, U(\tau) > t\}, \quad (4.29)$$

where $U(\tau)$ denotes a strictly increasing α -stable Levy motion - i.e., an α -stable process with Laplace transform

$$\langle \exp(-kU(\tau)) \rangle = \exp(-\tau k^\alpha). \quad (4.30)$$

4.5.1 Subordination Simulation for Fractional Diffusion Equation

When the potential $V(x) = \text{const}$, the subordinated Langevin dynamics describe the anomalous diffusion. A sample trajectory $X(S_t)$ of this subordinated Langevin dynamics on the lattice $\{t_i = i\Delta t : i = 0, 1, \dots, N\}$ requires simulation of the standard Langevin process $X(\tau)$ and the values $S_{t_0}, S_{t_1}, \dots, S_{t_N}$ of the subordinator S_t . $X(\tau)$ is a sample trajectory of a particle undergoing normal diffusion and can be obtained by integrating (4.28) with $V(x) = \text{const}$ using an Euler scheme

$$X(\tau + \Delta\tau) = X(\tau) + \sqrt{2K_1}\Delta W(\tau). \quad (4.31)$$

The values $S_{t_0}, S_{t_1}, \dots, S_{t_N}$ of the subordinator S_t are approximated by the definition $S_t = \inf\{\tau : U(\tau) > t\}$, where $U(\tau)$ is a strictly increasing β -stable Levy motion [17]. We find for such an index k that the condition $\tau_k \leq S_{t_i} \leq \tau_{k+1}$ is satisfied. Applying the linear interpolation to approximate the position $X(S_{t_i})$ at t_i ,

$$X(S_{t_i}) = \frac{X(\tau_{k+1}) - X(\tau_k)}{\tau_{k+1} - \tau_k}(S_{t_i} - \tau_k) + X(\tau_k), \quad (4.32)$$

sample paths $X(S_{t_0}), X(S_{t_1}), \dots, X(S_{t_N})$ of the subordinated process can be obtained for $0 < \beta < 1$ and $V(x) = \text{const}$ [17]. The results are shown in Figure 4.12. The intervals with $X(S_t)$ being constant indicate the heavy-tailed waiting times of the underlying CTRW process.

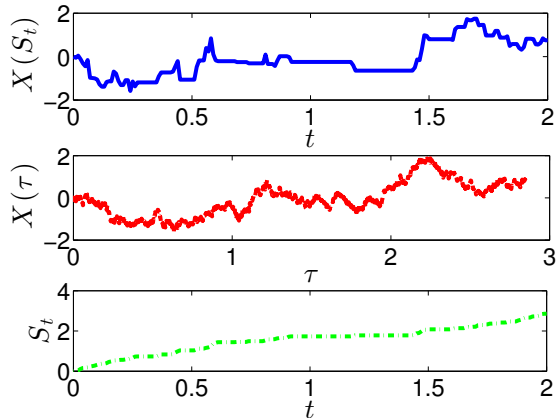


Figure 4.12: A sample realization of the subordinated Langevin dynamics $X(S_t)$ (blue/solid line), the standard Langevin dynamics $X(\tau)$ (red/dash-dot line), and the inverse-time β -stable subordinator S_t (green/dashed line), for simulating the anomalous diffusion in the presence of a constant potential $V(x) = \text{const}$. Here $\beta = 0.6$, $K_1 = 1$.

In Figure 4.13 left, the simulated mean-squared displacement of an ensemble of trajectories is compared with the exact formula (4.3). The time evolution of the histograms of $N = 10^4$ particle trajectories is plotted at different times $t = 0.02, 0.2$ and 20 for $\beta = 0.6$ (Figure 4.13 right). At $t = 0$, the pdf of the particle positions is a delta function $\psi_0(x) = \delta(x)$. Initially, the particles are diffusing slowly and the cusp singularity of the pdf of particle positions is observed. A more detailed description of the simulation algorithm can be found in [17].

4.5.2 Subordination Simulation for Fractional Diffusion-Advection Equation - Non-Galilean Invariant Case

With a linear potential $V(x) = -vx$, the subordinated Langevin dynamics describe the non-Galilean invariant case of the anomalous diffusion under the influence

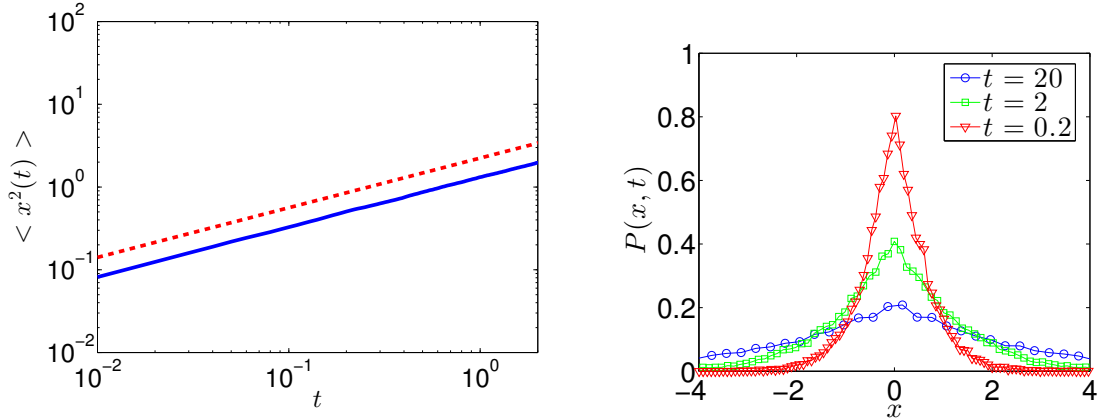


Figure 4.13: Left: The mean-squared displacement of an ensemble of the subordinated stochastic process $X(S_t)$ for describing anomalous diffusion with potential $V(x) = \text{const}$ (*blue/solid curve*) is compared with equation $\langle x^2(t) \rangle = 2K_\beta t^\beta / \Gamma(1+\beta)$ formulated by taking the second moment of (4.2) (*red/dashed curve*). Right: Evolution in time of the pdf of 10^4 subordinated sample path $X(S_t)$ with a constant potential $V(x) = \text{const}$. Here $\beta = 0.6$, $K_1 = 1$.

of an external velocity field (equation (4.12)). A sample path $X(\tau)$ of a particle experiencing Brownian motion and drift due to the external velocity is given by

$$X(\tau + \Delta\tau) = X(\tau) + v\Delta\tau + \sqrt{2K_1}\Delta W(\tau). \quad (4.33)$$

A sample trajectory $X(S_{t_0}), X(S_{t_1}), \dots, X(S_{t_N})$ can be obtained through the linear interpolation as in (4.32) [17]. In Figure 4.14, a sample realization of the subordinated process with $\beta = 0.6, v = 10$ is shown. The particle occasionally gets trapped and then drifts with the velocity again after a long time. This trajectory matches with the CTRW approach for simulating the non-Galilean invariant fractional diffusion-advection equation. In Figure 4.15 *left*, the mean-squared displacement computed by taking ensemble average of $N = 10^4$ trajectories is compared with the exact formula for the non-Galilean invariant model (4.13). The histograms of $N = 10^4$ particle trajectories are plotted at different times $t = 0.02, 0.2$ and 20 for $\beta = 0.6$ (Figure 4.15 *right*).

In Figure 4.16, the simulation results for the ensemble average of the particle

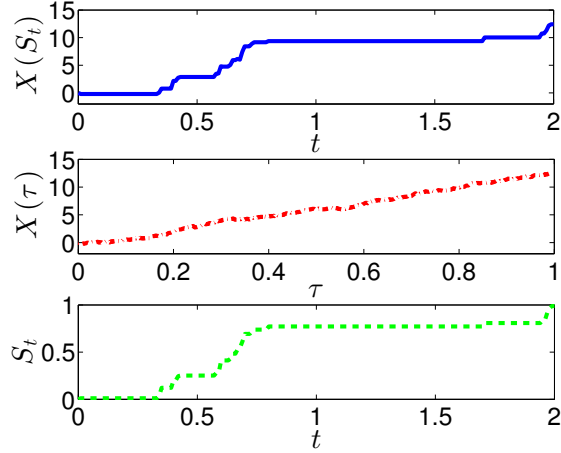


Figure 4.14: A sample realization of the anomalous diffusion $X(S_t)$ (blue/solid line), the standard Langevin dynamics $X(\tau)$ (red/dash-dot line), and the inverse-time β -stable subordinator S_t (green/dashed line), in the presence of a linear potential $V(x) = -vx$. Here $v = 10$, $K_1 = 1$, and $\beta = 0.6$.

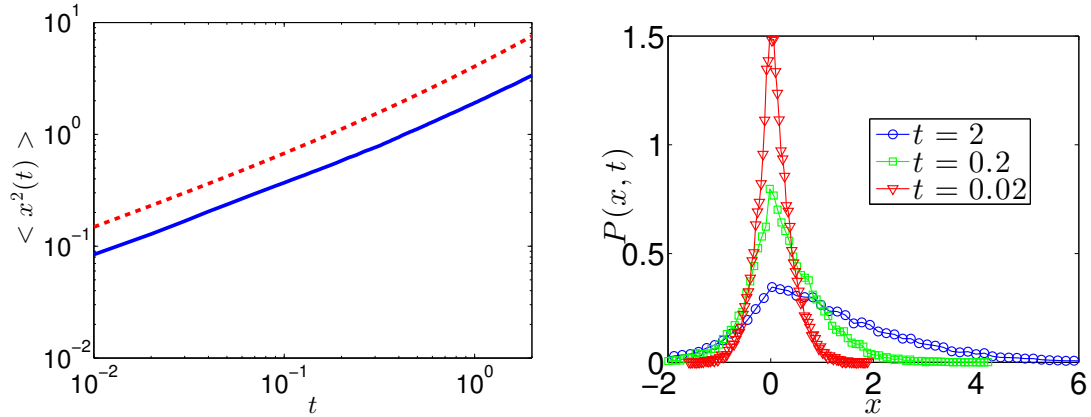


Figure 4.15: Left: The mean-squared displacement of an ensemble of the subordinated stochastic process $X(S_t)$ for describing anomalous diffusion with potential $V(x) = -vx$ (blue/solid curve) is compared with equation $\langle x^2(t) \rangle = \frac{2K_\beta t^\beta}{\Gamma(1+\beta)} + \frac{2v^2 t^{2\beta}}{\Gamma(1+2\beta)}$ formulated by taking the second moment of (4.12) (red/dashed curve). Right: Evolution in time of the pdf of 10^4 subordinated sample path $X(S_t)$ with a linear potential $V(x) = -vx$. Here $\beta = 0.6$, $K_1 = 1$.

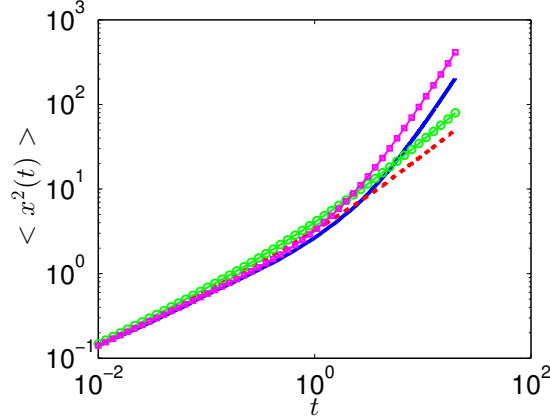


Figure 4.16: Comparison of the mean-squared displacement of an ensemble by: simulation of particles moving on a CTRW under the influence of an external velocity field in the non-Galilean invariant case (*blue/solid curve*), simulation of the subordinated stochastic process $X(S_t)$ for describing anomalous diffusion with potential $V(x) = -vx$ (*red/dashed curve*), the equation $\langle x^2(t) \rangle = \frac{2K_\beta t^\beta}{\Gamma(1+\beta)} + \frac{2v^2 t^{2\beta}}{\Gamma(1+2\beta)}$ formulated by taking the second moment of (4.12) (*green/circles*), and the equation $\langle x^2(t) \rangle = \frac{2K_\beta t^\beta}{\Gamma(1+\beta)} + v^2 t^2$ formulated by taking the second moment of (4.10) (*magenta/squares*). Here $\beta = 0.6$, and $K_\beta = 1$.

mean-squared displacements for the non-Galilean invariant case using a CTRW approach (*blue/solid curve*), and using the subordination method (*red/dashed curve*), are compared with the predictions of the equations $\langle x^2(t) \rangle = \frac{2K_\beta t^\beta}{\Gamma(1+\beta)} + \frac{2v^2 t^{2\beta}}{\Gamma(1+2\beta)}$ formulated by taking the second moment of (4.12) (*green/circles*) and the equation $\langle x^2(t) \rangle = \frac{2K_\beta t^\beta}{\Gamma(1+\beta)} + v^2 t^2$ formulated by taking the second moment of (4.10) (*magenta/squares*), for $0 < t < 20$. For the longer times the mean-squared displacement predicted by the CTRW model asymptotes t^2 similar to the predictions of the Galilean invariant model, while the mean-squared displacement for the non-Galilean invariant model as simulated by subordination method asymptotes $t^{2\beta}$ in the long-time limit similar to the second moment of the non-Galilean invariant prediction. Despite the fact that the CTRW simulation of the non-Galilean invariant model and that of the second moment prediction agree asymptotically at short and at long times, they do not agree in the mid-time range (near $t=1$). In this regime the CTRW process slows

down with the curve evidencing a pronounced elbow.

4.5.3 Subordination Simulation for Fractional Fokker-Planck Equation

With the potential $V(x) = \frac{1}{2}bx^2$, the subordinated Langevin dynamics describe the anomalous diffusion under the influence of an external force field $F(x) = -bx$. A sample realization of $X(\tau)$ for a particle experiencing Brownian motion and external force is given by

$$X(\tau + \Delta\tau) = X(\tau) - bX(\tau)\Delta\tau + \sqrt{2K_1}\Delta W(\tau). \quad (4.34)$$

A sample path $X(S_{t_0}), X(S_{t_1}), \dots, X(S_{t_N})$ of a particle for fractional Fokker-Planck equation with $V(x) = \frac{1}{2}bx^2$ is simulated [17] (Figure 4.17). In Figure 4.18 *left*, the mean-squared displacement of ensemble trajectories is plotted along with a power law $\langle x^2(t) \rangle = 2t^\beta/\Gamma(1 + \beta)$ (the mean-squared displacement of particles in the absence of the external force field) as a comparison. The time evolution of the histograms of $N = 10^4$ particle trajectories is plotted at different times $t = 0.02, 0.2$ and 20 for $V(x) = \frac{1}{2}bx^2$ and $\beta = 0.6$ (Figure 4.18 *right*).

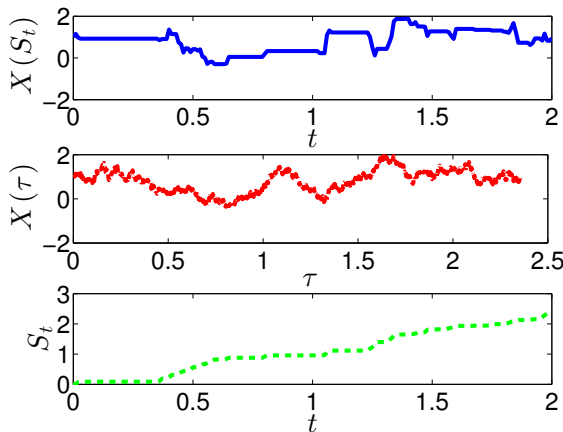


Figure 4.17: A sample realization of the anomalous diffusion $X(S_t)$ (*blue/solid line*), the standard Langevin dynamics $X(\tau)$ (*red/dash-dot line*), and the inverse-time β -stable subordinator S_t (*green/dashed line*), in the presence of a parabolic potential $V(x) = \frac{1}{2}bx^2$. Here $\beta = 0.6$, $b = 1$, $K_1 = 1$.

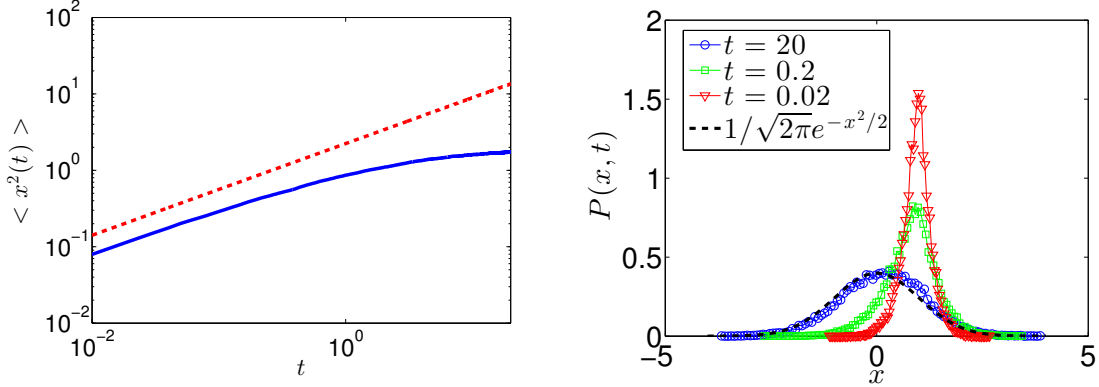


Figure 4.18: Left: The mean-squared displacement of an ensemble of the subordinated stochastic process $X(S_t)$ for describing anomalous diffusion with potential $V(x) = -\frac{1}{2}bx^2$ (*blue/solid curve*) is compared with a power law $\langle x^2(t) \rangle = 2K_\beta t^\beta / \Gamma(1 + \beta)$ (the mean-squared displacement of particles with subdiffusion) (*red/dashed curve*). Right: Evolution in time of the pdf of 10^4 subordinated sample path $X(S_t)$ with a linear potential $V(x) = -\frac{1}{2}bx^2$. The time evolution of the pdf of particle positions slowly relaxes towards the Boltzmann distribution $\psi_{st}(x) = 1/\sqrt{2\pi} \exp(-bx^2/2)$ black/dashed line. Here $\beta = 0.6$, $b = 1$, $K_1 = 1$.

4.6 Summary of Simulations Using CTRW and the Subordination Method

We have investigated subdiffusion under the influence of an external velocity field or force field. Fractional differential equations for the pdf $\psi(x, t)$ of finding a particle at position x at time t have been formulated in [20] for various cases, e.g. the Galilean invariant fractional diffusion-advection equation, the non-Galilean invariant fractional diffusion-advection equation, and the fractional Fokker-Planck equation. The above processes can be modeled using a CTRW approach or using a subordinated Langevin simulation. The CTRW models are simulated with a Gaussian distribution of jumps as well as velocity/force field and a one-parameter Mittag-Leffler distribution of waiting times. The CTRW model converges to the fractional equations in the long-time limit for the fractional diffusion equation in the Galilean invariant fractional diffusion-advection equation situation. The CTRW simulation of the non-Galilean invariant fractional diffusion-advection equation requires more investigation with regard to the

particle jump lengths, due to the external velocity. What we have simulated in equation (4.26) is an exemplar CTRW process which is not Galilean invariant, but it does show the same asymptotic behavior as the Galilean invariant prediction at long times. A subordination method to simulate the fractional Fokker-Planck equation based on a discretized form of a subordinated Langevin equation in which the physical time defined via the number of subsequent steps of motion is itself a random variable was presented. In this approach, one does not need to generate Mittag-Leffler random variables since the heavy-tailed waiting times between successive particle jumps are simulated by allowing a random change of time in the Langevin dynamics with the subordinator [17]. The subordination method has the limitation that it can only be used to simulate the non-Galilean invariant fractional diffusion-advection model. It remains a challenge to discover a subordination algorithm that would apply to a systems with separate waiting-time distributions for different dynamics, for example, the Galilean invariant fractional diffusion-advection equation.

In addition to the limitations of the subordination method, the comparison of these two approaches has been discussed in [9] in the absence of external velocity or force field. As suggested in [9], the method based on the subordinated Langevin equation leads to a higher accuracy of results, while the CTRW framework with a Mittag-Leffler distribution of waiting times provides efficiently an approximate fundamental solution to the fractional Fokker-Planck equation and converges to the pdf function of the subordinated process in a long-time limit. In that paper, the comparison between numerical results of a CTRW simulation and the subordination simulation and their analytical analogs is based on the analysis of the sum of squared deviations [9]. However, this analysis is limited to the fractional diffusion equation case, in which no external velocity or force field is added. The comparison of these two methods with inclusion of external velocity or force fields requires further research. These simulation algorithms developed for one-dimensional systems prepare for simulating anomalous transport in three-dimensional soft material systems. The investigation of particle

dynamics modeled through the CTRW approach and the subordination method suggests the possibilities of application of that scenario in stochastic modeling of the non-exponential phenomena observed in soft materials.

Chapter 5

TRANSIENT NETWORK MODELS

Soft materials self-organize into mesoscopic structures that are much larger than the microscopic scale (the atomic or molecular scale). The microstructure of a soft material system can form a network with either a transient or permanent character [28, 29]. These super-assemblies of molecules result in interesting physical properties of the bulk materials. Soft material systems are characterized by the presence of a broad range of microstructural time scales and this results in a broad power-law spectra during stress relaxation or small amplitude oscillatory tests. The multiscale microstructure of these materials is closely connected with the subdiffusive behavior of tracer particles seen in microrheology experiments and leads to power-law/stretched-exponential stress relaxation observed in bulk rheology experiments [22].

The mechanical models that are commonly used to describe the rheology of multiscale materials often require the introduction of a large number of fitting parameters. The number of parameters needed to fit the experimental data depends on the measurement time and therefore this modeling approach is unsatisfactory [15]. Transient network models provide a convenient way to coarse-grain the soft material system to a three-dimensional network and use bead-spring dumbbells as the basic elements of the network. Green and Tobolsky [12] developed a network model with temporary crosslinks formed as a result of reversible bonds and examined the model predictions under shearing flow. Lodge showed that under the assumption that the bonds break and reform at equal rates and that the networked chains move with the flow [3], this model results in a constitutive equation for stress which is identical to that of the upper-convected Maxwell (UCM) model. The aforementioned transient network model is a more fundamental model for simulating the networked systems and

a detailed description of the formulation of three-dimensional network models can be found in the book by Bird et al. [3].

Transient network models use bead-spring dumbbells to represent network components. The bead-spring dumbbell is one simple idealization of an aggregate. Within the network, the dumbbells can have different states, active (both ends of the dumbbell beads are attached to the network), dangling (one end of the dumbbell is attached and the other end is free), and free (both ends of the dumbbell are free). The network is transient in that the linkages are not permanent, beads can disconnect, or disconnected strands can re-connect to the network.

In this chapter, we begin with some exemplar network models, i.e. the transient network model with topology, the dumbbell model, the Lodge network model and a two-species network model. Stochastic versions of these models are presented and model predictions under homogeneous shear flows are investigated. To model anomalous transport as well as capture the multiscale microstructural characteristics of the soft material systems, we propose several new transient network models by combining CTRW or subordinated Langevin dynamics into the system. We show that the stress relaxation exhibits a non-exponential pattern if we model the breakage/recombination events and/or spring and elastic forces as CTRW processes. We will also present a subordinated two-species network model. By using a rescaling of time through the subordinator, this subordinated Langevin dynamic describes a network with convection, spring/elastic forces and breakage/recombination processes with dynamics slowed down, leading to non-exponential relaxation behaviors. We use the prime, (\prime), to denote all dimensional variables throughout this chapter.

5.1 Transient Network Model with Topology

5.1.1 Model Description

Transient network models have been examined by [5, 7, 32]. In [7], the topology of the network structure was carefully tracked and the number of elements allowed to connect at each junction is predetermined. The entire network reorganizes if an element

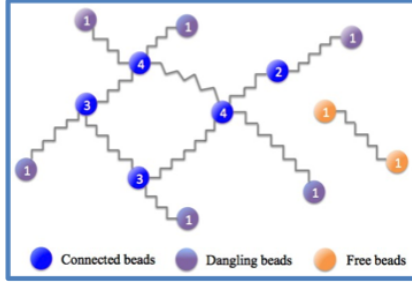


Figure 5.1: A reversible cross-linked network formed by bead-spring dumbbells and sticky nodes following [7]. In this example, the sticky nodes capture a maximum of $f_{\max} = 4$ beads to form junction points. Each node has a finite lifetime. The lifetimes follow an exponential distribution with mean τ . Thus, the network reorganizes as time passes by.

connects or disconnects from a junction. Thus, the network relaxation depends on the number of and topology of cross-links or entanglements. The disadvantage of this model is the computational complexity as the entire network and interactions are accounted for.

In [7], each bead experiences drag within the solvent solution, the elastic spring force, a Brownian force, and a repulsion force from neighboring dumbbells. By inserting sticky nodes into the box (nodes which can attract up to f_{\max} beads from within a distance d), a network is formed. The attached beads and the node move together. In their work [7], the lifetime of the nodes followed an exponential distribution $\lambda_i \sim \exp(-t'/\lambda_{Br})$, where λ_{Br} is the mean lifetime of the nodes. Once the lifetime of a node is reached, the node releases all its attached beads. The node then randomly jumps to another location inside the simulation domain and the released beads move separately. This process repeats continuously in time, thus, the nodes and attached beads form a reversible cross-linked network. In that paper, all spatial locations were tracked thus the topology of the network was captured.

The imposed velocity is $\mathbf{v}_s'(\mathbf{r}') = \mathbf{v}'_0 + \boldsymbol{\kappa}' \cdot \mathbf{r}'$, where \mathbf{v}'_0 is independent of the position vector \mathbf{r}' and $\boldsymbol{\kappa}'$ denotes the transpose of the velocity gradient, $\kappa'_{ij} = \partial v'_i / \partial x'_j$. The beads experience a viscous drag force $\mathbf{F}'_{drag} = -\zeta(\mathbf{v}' - \mathbf{v}'_s)$ when they move with

respect to the solvent, in which ζ is the drag coefficient. The elastic force between two beads connected by a spring is assumed linear, $\mathbf{F}'_{spring} = H\mathbf{Q}'$, where $\mathbf{Q}' = \mathbf{r}'_2 - \mathbf{r}'_1$ is the vector connecting the two beads of the dumbbell, located at positions $\mathbf{r}'_1, \mathbf{r}'_2$, and H is the Hookean spring constant. As suggested in [7], a repulsive force between the beads is required to avoid the gradual build-up of a concentration gradient in bead positions and to keep the system homogeneous. Each bead also moves randomly through Brownian motion.

Through the equation of motion for a bead of the dumbbell, the Langevin equation for the bead's velocity can be found and is

$$\mathbf{v}' = \mathbf{v}'_0 + \boldsymbol{\kappa}' \cdot \mathbf{r}' + (\mathbf{F}'_{repulsion} + \mathbf{F}'_{spring} + \mathbf{F}'_{stochastic})/\zeta. \quad (5.1)$$

By integrating the above Langevin equation over a time step $\delta t'$ using a first-order Euler scheme, the position vector \mathbf{r}' of the bead is determined by:

$$\mathbf{r}'(t' + \delta t') = \mathbf{r}'(t') + \mathbf{v}'_0 \delta t' + \boldsymbol{\kappa}' \cdot \mathbf{r}' \delta t' + \frac{1}{\zeta} \left[\mathbf{F}'_{spring}(t') + \sum \mathbf{F}'_{repulsion}(t') \right] \delta t' + \delta \mathbf{r}', \quad (5.2)$$

where the stochastic step $\delta \mathbf{r}'$ is given by

$$\delta \mathbf{r}' = \frac{1}{\zeta} \int_{t'}^{t'+\delta t'} \mathbf{F}'_{stochastic}(s) ds = \sqrt{2D\delta t'} \delta \mathbf{W}'(t'). \quad (5.3)$$

Here $\delta \mathbf{W}'(t')$ is the Wiener increment during a time step $\delta t'$ and the diffusion coefficient $D = k_B T / \zeta$, k_B is the Boltzmann's constant and T is the temperature. If the node captures more than one bead, then a junction is formed. The attached beads move cooperatively with the node/junction. The new configuration of node and attached beads can be obtained by summing up all the forces working on the beads attached to the node and then dividing by the number f of attached beads on the node,

$$\mathbf{r}'(t' + \delta t') = \mathbf{r}'(t') + \mathbf{v}'_0 \delta t' + \boldsymbol{\kappa}' \cdot \mathbf{r}' \delta t' + \frac{1}{f\zeta} \left[\sum \mathbf{F}'_{spring}(t') + \sum \mathbf{F}'_{repulsion}(t') \right] \delta t' + \delta \mathbf{r}'. \quad (5.4)$$

During each time step $\delta t'$, the probability of detachment for the node is taken to be constant, $P = 1 - \exp(-\delta t' / \lambda_{Br})$. Once a node is detached, it moves randomly inside the simulation box and the attached beads are freed. The node continues to capture

free beads within a given distance d of its new location. This process repeats during the simulation time period. We choose the relaxation time of a free dumbbell $\lambda_H = \zeta/4H$ as the time scale, and the equilibrium size of a dumbbell $l_H = \sqrt{k_B T/H}$ as the length scale. The dimensionless equation for a detached bead is thus

$$\mathbf{r}(t + \delta t) = \mathbf{r}(t) + \mathbf{v}_0 \cdot \delta t + \boldsymbol{\kappa} \cdot \mathbf{r} \delta t + \left[\frac{\mathbf{Q}}{4} + \frac{1}{4H} \sum_{d(\mathbf{r}, \mathbf{r}_i) < d} \mathbf{F}_{repulsion} \right] \delta t + \frac{\sqrt{2\delta t}}{2} \delta \mathbf{W}. \quad (5.5)$$

To investigate the flow behavior of soft materials, the calculation of the stress tensor is of special interest. The stress tensor $\boldsymbol{\tau}'_p$, which describes the force exerted across an oriented surface in a fluid, can be expressed in terms of bead-spring chain configurations as follows [3, 25]

$$\boldsymbol{\tau}'_p = -\boldsymbol{\sigma}' + nk_B T \mathbf{I}, \quad (5.6)$$

where n is the number density of dumbbells (number per unit volume) and \mathbf{I} is the 3×3 identity matrix. We define the configuration tensor $\boldsymbol{\sigma}' = nH \langle \mathbf{Q}'\mathbf{Q}' \rangle = nH \int \mathbf{Q}'\mathbf{Q}'\psi' d\mathbf{Q}'$, which is the second moment of the dumbbell configuration distribution $\psi'(\mathbf{Q}', t')$. The averaging $\langle \rangle$ is performed over the dumbbells present in the simulation domain. The stress tensor is scaled by $nk_B T$. The tensor $\boldsymbol{\sigma}$ results from the elastic spring forces and the non-dimensional form is $\boldsymbol{\sigma} = \langle \mathbf{Q}\mathbf{Q} \rangle$. Here σ_{ij} ($i, j = x, y, z$) are the components of the instantaneous stress tensor and $\boldsymbol{\sigma} = \mathbf{I} - \boldsymbol{\tau}_p$. For simplicity, we use the stress tensor $\boldsymbol{\sigma}$ in the following stochastic simulations.

5.1.2 Simulation Results

In order to simulate an infinite network in equilibrium and in shear flow conditions, periodic boundary conditions and Lees-Edwards boundary conditions are employed respectively [1, 7]. The advantage of this modeling is that the network topology is taken into account and the effect of the network reorganizations is considered. For a simple case in which the nodes are allowed to capture at most one bead $f_{\max} = 1$, this model predicts flow properties identical to those of the UCM model. Under equilibrium conditions, the beads move according to equation (5.5) with $\boldsymbol{\kappa} = \mathbf{0}$ and the

positions of two connected beads are subtracted to obtain the dumbbell vector \mathbf{Q} . A shear flow with velocity $v_x = \dot{\gamma}y$, $v_y = 0$, $v_z = 0$ is imposed on the system at $t = 0$. The shear stress σ_{yx} and first normal stress difference $N_1 = \sigma_{xx} - \sigma_{yy}$ are computed by taking the ensemble average of all the dumbbell vectors, i.e. $\sigma_{yx} = \sum Q_y Q_x / N$, $N_1 = \sum Q_x Q_x / N - \sum Q_y Q_y / N$. As shown in Figure 5.2, the dimensionless shear stress and first normal stress difference increase with time and eventually reach to a steady-state $\sigma_{yx_{ss}} = \dot{\gamma}$ and $N_{1_{ss}} = 2\dot{\gamma}^2$.

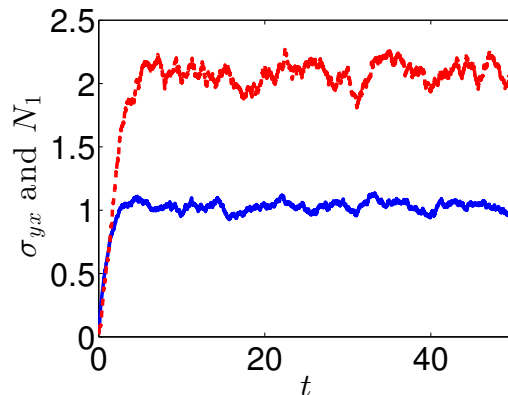


Figure 5.2: Under steady-shear flow with $v_0 = 0$, $\dot{\gamma} = 1$, the shear stress and first normal stress of the van den Brule and Hoogerbrugge [7] system with $f_{\max} = 1$ grow as a function of time and eventually reach steady-state values $\sigma_{yx_{ss}} = 1$ (*blue/solid curve*) and $N_{1_{ss}} = 2$ (*red/dashed curve*).

If the nodes are allowed to capture more than one bead, then a networked system may be formed. In this case, the simulation poses computational challenges due to the necessity of keeping track of the network topology. The challenges increase further if the model is extended to allow a non-exponential distribution of node lifetimes. As an alternative to this model, in the following sections, an ensemble of dumbbells without taking into account their physical locations is considered [3, 5, 32]. While these models are computationally efficient to simulate, the actual network structure and spatial distribution are lost.

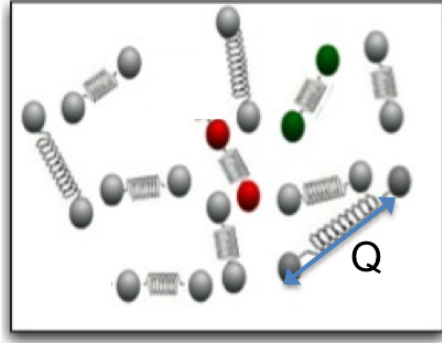


Figure 5.3: A phenomenological network system with bead-spring dumbbells which can attach or detach [5].

5.2 Dumbbell Model

5.2.1 Model Description

In a simplification of the network model described above, we follow a system of dumbbell vectors \mathbf{Q}' instead of keeping track of the physical location \mathbf{r}' of each dumbbell bead (Figure 5.3). First, we consider the dumbbell model, where breakage/recombination processes are not active. The forces that balance the end-to-end vector \mathbf{Q}' of the dumbbell are the difference of the solvent drag force on each of the beads, the Hookean spring force and the difference of the Brownian force caused by collisions between solvent molecules and the beads. The dimensional Langevin equation describing the dumbbell connector vector \mathbf{Q}' is thus [25]:

$$d\mathbf{Q}' = \left[\boldsymbol{\kappa}' \cdot \mathbf{Q}' - \frac{2H}{\zeta} \mathbf{Q}' \right] dt' + \sqrt{\frac{2k_B T}{\zeta}} d\mathbf{W}'. \quad (5.7)$$

The non-dimensional stochastic differential equation is:

$$d\mathbf{Q} = \left[\boldsymbol{\kappa} \cdot \mathbf{Q} - \frac{1}{2} \mathbf{Q} \right] dt + \sqrt{\frac{1}{2}} d\mathbf{W}. \quad (5.8)$$

Time has been made dimensionless in this equation by $\lambda_H = \zeta/(4H)$ and length by $l_H = \sqrt{k_B T/H}$. To solve this model, the stochastic differential equation (5.8) is integrated over an infinitesimal time step Δt using the Euler scheme

$$\mathbf{Q}(t + \Delta t) = \mathbf{Q}(t) + \left[\boldsymbol{\kappa} \cdot \mathbf{Q}(t) - \frac{1}{2} \mathbf{Q}(t) \right] \Delta t + \Delta \mathbf{W}. \quad (5.9)$$

For a single dumbbell, its connector vector trajectory at each time step can be obtained through (5.9). A large number $N = 2 \times 10^4$ of independent chains are simulated and the resulting second moments are averaged to obtain stress tensor $\boldsymbol{\sigma}$. For this dumbbell model, there exists only one relaxation time scale λ_H .

5.2.2 Analytical Form of the Stress Tensor for the Dumbbell Model

For dumbbells following stochastic dynamics as in (5.8), the evolution of the configuration distribution function $\psi(\mathbf{Q}, t)$ of dumbbell connectors is governed by the partial differential equation

$$\frac{\partial \psi}{\partial t} = - \left(\frac{\partial}{\partial \mathbf{Q}} \cdot \left[\boldsymbol{\kappa} \cdot \mathbf{Q} \psi - \frac{1}{2} \mathbf{Q} \psi - \frac{1}{2} \frac{\partial \psi}{\partial \mathbf{Q}} \right] \right), \quad (5.10)$$

where $\psi(\mathbf{Q}, t)$ describes the probability of finding a dumbbell with connector vector \mathbf{Q} at time t . The left-hand side is the time rate change of the distribution function and the three terms on the right-hand side represent the change in the dumbbell connector vector due to the hydrodynamic drag force, the linear Hookean spring force and the Brownian motion, respectively [3]. The above PDE for $\psi(\mathbf{Q}, t)$ is a Fokker-Planck equation and the stochastic differential equation (5.8) characterizes a stochastic process with probability distributions equal to those obtained from the Fokker-Planck equation (5.10). This equivalence is mathematically rigorous and is proved in [25].

The equilibrium configuration distribution is obtained by solving (5.10) with $\partial \psi / \partial t = 0$, $\boldsymbol{\kappa} = \mathbf{0}$,

$$\psi_{eq}(\mathbf{Q}) = \left(\frac{1}{2\pi} \right)^{3/2} e^{-\mathbf{Q} \cdot \mathbf{Q} / 2}. \quad (5.11)$$

This is a Gaussian distribution of the end-to-end vector with zero mean and variance 1 [3]. The equilibrium length distribution is given by [3]

$$\psi_{eq}(Q) = 4\pi Q^2 \left(\frac{1}{2\pi} \right)^{3/2} e^{-Q^2 / 2}. \quad (5.12)$$

The exact form of the stress tensor for the bead-spring dumbbell model can be computed by taking the second moment of equation (5.10). This allows a way to check the stochastic simulation of the dumbbell model under shear flows and builds

a connection between the stochastic processes and the macroscale continuum fluid mechanics. Multiplying equation (5.10) by the second-order tensor $\mathbf{Q}\mathbf{Q}$ and integrating over configuration space gives:

$$\frac{d}{dt} \langle \mathbf{Q}\mathbf{Q} \rangle - \boldsymbol{\kappa} \cdot \langle \mathbf{Q}\mathbf{Q} \rangle - \langle \mathbf{Q}\mathbf{Q} \rangle \cdot \boldsymbol{\kappa}^t = \mathbf{I} - \langle \mathbf{Q}\mathbf{Q} \rangle. \quad (5.13)$$

The dumbbells' contribution to the stress $\boldsymbol{\tau}_p$ is thus:

$$\boldsymbol{\tau}_p + \boldsymbol{\tau}_{p(1)} = -\dot{\boldsymbol{\gamma}}, \quad (5.14)$$

where $\boldsymbol{\tau}_p = \mathbf{I} - \langle \mathbf{Q}\mathbf{Q} \rangle$, $\boldsymbol{\tau}_{p(1)}$ is the upper-convected derivative of $\boldsymbol{\tau}_p$ and $\dot{\boldsymbol{\gamma}}$ is the strain rate tensor (see Chapter 2). The constitutive equation (5.14), derived from the dumbbell model is exactly the UCM model of continuum mechanics. In a shear flow $v_x = \dot{\gamma}y$, $v_y = 0$, $v_z = 0$, as pointed out in chapter 2, the steady-state solution to equation (5.14) is

$$\tau_{p,xx} = -2\dot{\gamma}^2, \quad (5.15)$$

$$\tau_{p,yx} = -\dot{\gamma} = \tau_{p,xy}, \quad (5.16)$$

$\tau_{p,ij} = 0$ if $ij \neq xx, xy, \text{ or } yx$. Thus, this model predicts steady-state values of the stress tensor $N_1 = \sigma_{xx} - \sigma_{yy} = 2\dot{\gamma}^2$ and $\sigma_{yx} = \dot{\gamma}$ under steady-shear flow, where the stress tensor $\boldsymbol{\sigma} = \langle \mathbf{Q}\mathbf{Q} \rangle$.

5.2.3 Simulation Results

This stochastic process is investigated in equilibrium, and, in start-up and cessation of shear flow and allows a direct physical interpretation of bead-spring dumbbell dynamics. The simulation results are compared against the analytical form of the stress tensor obtained in the above section.

5.2.3.1 Equilibrium

Initially, a sample of $N = 2 \times 10^4$ dumbbells, with an equilibrium Gaussian distribution of end-to-end distances, is generated at random. In a given time step,

each dumbbell evolves according to the stochastic Langevin equation (5.9) with $\boldsymbol{\kappa} = \mathbf{0}$. The chain lengths stay Gaussian distributed as time evolves. The simulated histogram of dumbbell vector lengths is plotted against the exact distribution (5.12) at various times $t = 0, 5, 10$ as shown in Figure 5.4. The stress tensor $\boldsymbol{\sigma} = \mathbf{I}$ at equilibrium, i.e. $\sigma_{yx} = 0$, $N_1 = 0$.

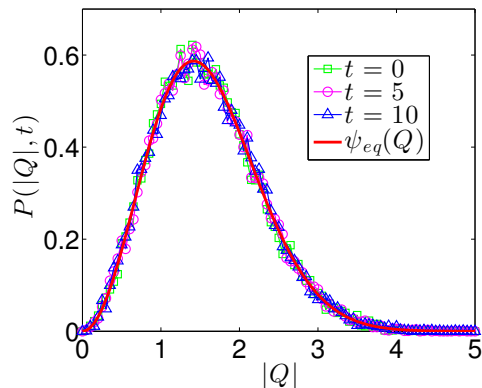


Figure 5.4: Starting from a Gaussian distribution, the probability distribution of dumbbell lengths at equilibrium for the dumbbell model at various times $t = 0$ (green/squares), $t = 5$ (magenta/circles), $t = 10$ (blue/triangles). The pdfs are compared with the equilibrium distribution (5.12) (red/solid curve).

5.2.3.2 Start-up and Cessation of Shear Flow

Under a shear flow $v_x = \dot{\gamma}y$, $v_y = 0$, $v_z = 0$ imposed at $t = 0$, the dumbbells experience stretching from convection, which is balanced by spring and Brownian forces. For a non-dimensional time t , $0 < t < 30$, a constant shear rate $\dot{\gamma} = 1$ is imposed on the system. For $30 < t < 35$, the shear flow is turned off and the stresses are allowed to relax. The pdfs of dumbbell lengths at different times $t = 0, t = 2, t = 5$ are shown in Figure 5.5 left; it can be seen that the distributions are shifting towards a higher percentage of more stretched connector vectors as time increases. Initially, the stresses grow until they reach steady-state values, those values match with the non-dimensional analytical predictions of this model at steady-state under shear flow

$\sigma_{xx} = 2\dot{\gamma}^2, \sigma_{yx} = \sigma_{xy} = \dot{\gamma}$ (Figure 5.5 right). This model predicts an exponential stress relaxation and this is consistent with the closed form solution of the macroscale constitutive model (5.14) under cessation of shear flow (Figure 5.5 right). In contrast to this model, we consider the Lodge network model in the next section, in which the dumbbells are allowed to break/reform.

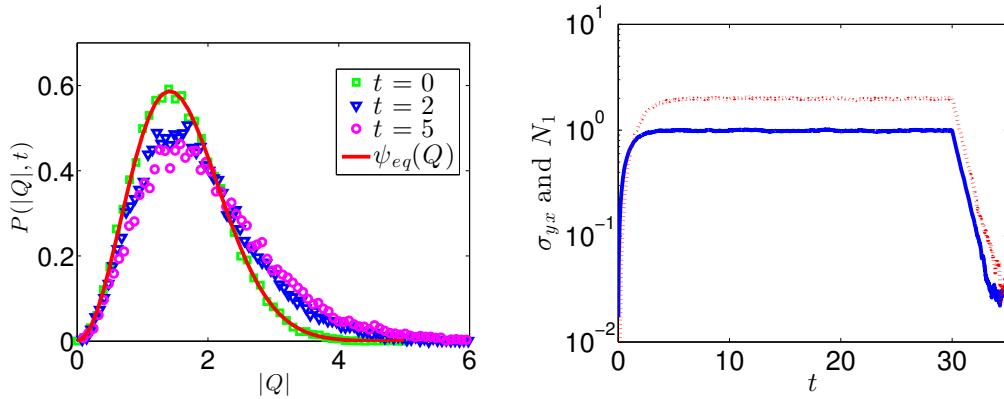


Figure 5.5: Stochastic simulation of the dumbbell model under shear flow with $\dot{\gamma} = 1$. Left: the probability distribution $P(|Q|, t)$ of all dumbbell lengths is plotted at various times $t = 0$ (green/squares), $t = 5$ (magenta/circles), $t = 10$ (blue/triangles). Right: The plot of the shear stress (blue/solid curve) and first normal stress difference (red/dashed curve) as a function of time. The imposed shear is turned off at $t = 30$ and the stress relaxes for $30 < t < 35$.

5.3 Lodge Network Model

5.3.1 Model Description

The Lodge network model only accounts for those chains connected to the network [3]. The network segments are assumed to be produced at a constant rate λ_{Br}^{-1} with a distribution of configuration identical to the Gaussian distribution (5.11), where λ_{Br} is the average breakage time. The destruction rate for the network chains is assumed to be a constant and equals λ_{Br}^{-1} . Also, the model assumes that the network strands move deterministically with the bulk flow (affine motion),

$$d\mathbf{Q}' = \boldsymbol{\kappa}' \cdot \mathbf{Q}' dt'. \quad (5.17)$$

In this model, we rescale time by λ_{Br} and length by $l_H = \sqrt{k_B T / H}$. The non-dimensional equation for (5.17) is:

$$d\mathbf{Q} = \boldsymbol{\kappa} \cdot \mathbf{Q} dt. \quad (5.18)$$

Integrating the equation (5.18) over a finite time step width, each network strand moves according to a discrete Euler approximation:

$$\mathbf{Q}(t + \Delta t) = \mathbf{Q}(t) + \boldsymbol{\kappa} \cdot \mathbf{Q}(t) \Delta t. \quad (5.19)$$

With the assumption that the breakage/recombination rates are constant, and equal, we simulate the breaking/reforming using a continuous time simulation in which the waiting times for the creation/destruction processes are exponentially distributed as

$$w'(t') = 1/\lambda_{Br} \exp(-t'/\lambda_{Br}). \quad (5.20)$$

The dimensionless waiting time distribution is $w(t) = \exp(-t)$. The simulation is carried out by generating random lifetimes for each of the attached chains and free chains. Random numbers following the exponential distribution $w(t) = \exp(-t)$ are generated using the inversion formula $t_i = -\ln u$ as in Chapter 4, where $u \in (0, 1)$ is a uniformly distributed random number. Once the lifetime of the network chain is reached, it detaches and joins the equilibrium ensemble. The stress carried by the detached segment relaxes instantly to zero. A new network segment drawn from the equilibrium distribution ψ_{eq} (5.11) is then created and this segment starts to move governed by equation (5.18), thus convecting with the bulk flow.

5.3.2 Analytical Form of the Stress Tensor for the Lodge Network Model

The time evolution of the configuration distribution of dumbbells following the stochastic process for the Lodge network model follows [3]

$$\frac{\partial \psi}{\partial t} = -\frac{\partial}{\partial \mathbf{Q}} \cdot [\boldsymbol{\kappa} \cdot \mathbf{Q}] \psi + \psi_{eq} - \psi, \quad (5.21)$$

where ψ_{eq} is the Gaussian distribution (5.11). Taking the second moment of equation (5.21), one obtains

$$\langle \mathbf{Q}\mathbf{Q} \rangle_{(1)} = \mathbf{I} - \langle \mathbf{Q}\mathbf{Q} \rangle. \quad (5.22)$$

The extra stress tensor $\boldsymbol{\tau}_p$ satisfies

$$\boldsymbol{\tau}_{p(1)} + \boldsymbol{\tau}_p = -\dot{\boldsymbol{\gamma}}. \quad (5.23)$$

Thus, the macroscopic stress equation (5.23) for the Lodge model is identical to that of the UCM model albeit with time scaled by $\lambda = \lambda_{Br}$ whereas the constitutive equation for the dumbbell model (5.14) with $\lambda = \lambda_H$. This equivalence seems surprising, since the Lodge model included neither spring force nor Brownian motion. Stochastic simulations for the Lodge network model show that the stochastic process under shear flow predicts the same results as the macroscopic Lodge/UCM model, in which the non-dimensional steady-state stresses satisfy $\sigma_{yx} = \dot{\gamma}$ and $N_1 = 2\dot{\gamma}^2$. The stress of this system relaxes exponentially (with relaxation time λ_{Br}), through the breakage and recombination processes, after cessation of shear flow.

5.4 Hybrid Lodge Network Model

5.4.1 Model Description

The dimensional convection equation for the ensemble distribution of dumbbells, $\psi'(\mathbf{Q}', t')$, for the Lodge network model with the addition of a spring force between connected beads and Brownian diffusion of beads, a hybrid Lodge/UCM equation, is

$$\frac{\partial \psi'}{\partial t'} = -\frac{\partial}{\partial \mathbf{Q}'} \cdot \left[\boldsymbol{\kappa}' \cdot \mathbf{Q}' \psi' - \frac{2k_B T}{\zeta} \frac{\partial \psi'}{\partial \mathbf{Q}'} - \frac{2H}{\zeta} \mathbf{Q}' \psi' \right] + \frac{\psi'_{eq}}{\lambda_{Br}} - \frac{\psi'}{\lambda_{Br}}, \quad (5.24)$$

where ψ'_{eq} is the equilibrium distribution as in (5.11). This model forces the use of this equilibrium Gaussian distribution. This hybrid model allows for two system time scales, the breakage time λ_{Br} and the relaxation time of a free dumbbell $\lambda_H = \zeta/(4H)$. The chains in this model experience two types of dynamics, they move under the influence of elastic forces, and Brownian motion, in addition to convection, while also undergoing breakage/reforming with constant rates λ_{Br}^{-1} . In this model, after cessation of shear, stress decay occurs by the diffusive and elastic properties as well as the through breakage/recombination processes. This is investigated below through a theoretical approach and by performing stochastic simulations.

5.4.2 Rheological Equation for Stress Tensor

The analytical form of the stress tensor for this model can be obtained by taking the second moment of the above PDE for the configuration distribution (5.24)

$$\boldsymbol{\sigma}'_{(1)'} = \frac{nk_B T \mathbf{I}}{\lambda_H} - \frac{\boldsymbol{\sigma}'}{\lambda_H} + \frac{nk_B T \mathbf{I}}{\lambda_{Br}} - \frac{\boldsymbol{\sigma}'}{\lambda_{Br}}. \quad (5.25)$$

Rewriting equation (5.25) using the stress tensor expression $\boldsymbol{\tau}'_p = -\boldsymbol{\sigma}' + nk_B T \mathbf{I}$, the rheological equation for the extra stress tensor gives

$$\boldsymbol{\tau}'_{p(1)'} + nk_B T \dot{\boldsymbol{\gamma}}' + \left(\frac{1}{\lambda_H} + \frac{1}{\lambda_{Br}} \right) \boldsymbol{\tau}'_p = \mathbf{0}. \quad (5.26)$$

When the shear flow is turned off, $\dot{\boldsymbol{\gamma}}' = \mathbf{0}$, the shear stress component from equation (5.26) follows

$$\frac{d\tau'_{p,yx}}{dt'} + \left(\frac{1}{\lambda_H} + \frac{1}{\lambda_{Br}} \right) \tau'_{p,yx} = 0. \quad (5.27)$$

The shear stress relaxes exponentially $\tau'_{p,yx} = \tau_0 \exp(-t'/\lambda_{sys})$ with a system relaxation time $\lambda_{sys} = \lambda_H \lambda_{Br} / (\lambda_H + \lambda_{Br})$ after cessation of shear flow. Here τ_0 is the shear stress value when we turn off the shear flow. In the limit $\lambda_H \gg 1, \lambda_{Br} \gg 1$, the parameter λ_{sys} goes to infinity and the system relaxes slowly. In this regime, the breakage/recombination process is slow with $\lambda_{Br} \gg 1$ and the dumbbells experience weak diffusional motion and spring force with $\lambda_H \gg 1$. When $\lambda_H \ll 1, \lambda_{Br} \ll 1$, the system relaxation time scale $\lambda_{sys} \rightarrow 0$ and the stress relaxes to zero immediately. If $\lambda_{Br} \ll \lambda_H, \lambda_H \sim 1$, the system is in the fast-breaking limit where the breaking and reforming happens on a much smaller time scale compared with the Brownian motion and elastic force. In this case, the system relaxation is dominant by the breakage/recombination $\lambda_{sys} \sim \lambda_{Br}$. If $\lambda_H \ll \lambda_{Br}, \lambda_{Br} \sim 1$, the breaking and reforming happens at a much slower time scale compared with the Brownian motion and elastic force and the stress relaxes mainly through diffusional and elastic motion $\lambda_{sys} \sim \lambda_H$. In the intermediate regime $\lambda_{Br} \sim 1$ and $\lambda_H \sim 1$, both breakage/recombination and diffusion/elasticity contribute equally to the system stress decay.

5.4.3 Simulation Results

This model is solved stochastically to examine the interplay of the two fundamental relaxation processes through the diffusional motion and spring force as well as the breakage and recombination. The breaking and reforming are simulated using a continuous time simulation as in the Lodge network model. In this simulation, the time scale is chosen to be λ_H and length $l_H = \sqrt{k_B T/H}$. Thus, the lifetimes of the breakage and recombination events are exponentially distributed according to $w(t) = 1/\lambda \exp(-t/\lambda)$ with mean $\lambda = \lambda_{Br}/\lambda_H$. Each of the network strands moves according to a discrete Euler approximation as in (5.9).

5.4.3.1 Inception and Cessation of Steady Shear Flow

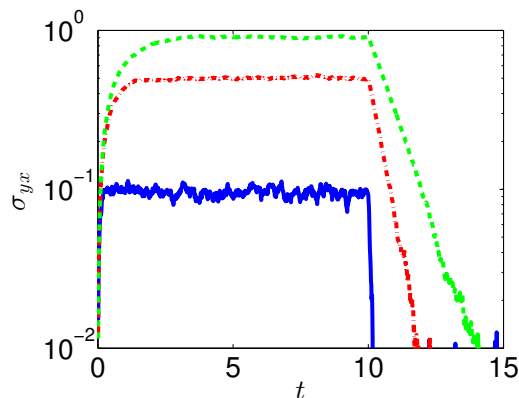


Figure 5.6: Stochastic simulation of the hybrid Lodge network model with spring force and diffusion, under shear flow, with $\dot{\gamma} = 1$ for $0 < t < 10$, and $\dot{\gamma} = 0$ for $t > 10$. The plot is stress versus time for simulations with $\lambda = 0.1$ (*blue/solid curve*), $\lambda = 1$ (*red/dash-dot curve*) and $\lambda = 10$ (*green/dashed curve*) is compared.

The above model is solved under steady homogeneous shear flow followed by cessation of the imposed shear. For $0 < t < 10$, $\mathbf{v} = (\dot{\gamma}y, 0, 0)$ with $\dot{\gamma} = 1$ and with $\lambda = 0.1, 1, 10$, the simulated shear stress is plotted in time (Figure 5.6). At $t = 10$, the flow is stopped and the stress relaxation is recorded for $t \geq 10$. With λ small, the attachment/detachment happens more frequently. The shear stress reaches a higher

steady-state value with a larger λ . The stress relaxation after cessation of the steady shear flow is exponential with a faster decay rate when λ is smaller, i.e. the shear stress relaxes rapidly to zero when $\lambda = 0.1$.

5.4.3.2 Step Strain Relaxation

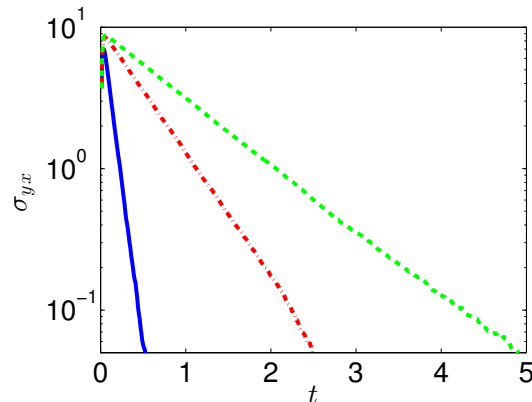


Figure 5.7: Stress relaxation following a step strain for the hybrid Lodge network model with spring force and diffusion with parameters $\lambda = 0.1$ (*blue/solid curve*), $\lambda = 1$ (*red/dash-dot curve*) and $\lambda = 10$ (*green/dashed curve*). Here $\gamma_0 = 10, b = 100$.

In a step strain experiment, the equilibrium state of the networked system is instantly disturbed, the relaxation is recorded. In practice, for a parallel plate geometry, the displacement of the top plate cannot be completed in zero time. Thus, a ramp in strain with the velocity $v_x = \gamma_0 b^2 t \exp(-bt)$ is employed in numerical simulation [39]. Letting $b \rightarrow \infty$ gives the ideal step strain flow. Following a step strain, the stress decays exponentially (Figure 5.7). Similar to the predictions of stress decay after cessation of shear flow, the stress relaxation under step strain is slower with a larger value of λ .

The stochastic simulation results agree/confirm with the analytical exact solution of the stress. The above model includes the bead-spring dumbbell dynamics and the breakage/recombination of network chains. Each process leads to an exponential

stress relaxation behavior when the shear flow is turned off. When breaking and reforming processes happens frequently within the time scale of the diffusive motion of the whole network, any applied shear stress relaxes through this process. The stress relaxation behavior predicted by this model can be characterized by a single time scale, the ratio of the breakage and diffusion time scale $\lambda = \lambda_{Br}/\lambda_H$. In the next section, a stochastic Lodge network model with a heavy-tailed waiting time distribution for breakage/recombination is presented.

5.5 Fractal Lodge Network Model

5.5.1 Model Description

By assuming that the lifetimes/waiting times of the association/dissociation processes follow an exponential distribution, the Lodge network model predicted an exponential stress relaxation behavior with a relaxation time scale determined by the breakage time λ_{Br} . It has been suggested that the non-exponential stress relaxation behavior is due to the slow breakage/recombination events which leads to a spectrum of relaxation time scales existing in the system. The slow breakage/recombination dynamics of soft materials has been studied theoretically and experimentally in many papers [4, 28, 29]. The complicated networked structure of soft materials can cause long time scale (non-local) effects that slow down the breakage/recombination processes. These linkages can be thought of as entrapments. As pointed out by Cates [4], for a system of polydisperse chains experiencing reptation motion, the slow breakage/recombination processes can lead to non-exponential stress relaxation behavior. In transient network models, a bead attached to the network can be considered to be residing in a parabolic potential well of depth U_0 [5]. The rate at which the bead overcomes the potential barrier to leave the well by thermal motion is described by an Arrhenius expression [5]. Thus, the lifetime of an attached bead λ_{Br} follows

$$\lambda_{Br} \propto \exp\left(\frac{U_0}{k_B T}\right). \quad (5.28)$$

The temporary decay of the probability of finding the particle within the potential well is given by an exponential function [20]

$$p(t') = \exp(-t'/\lambda_{Br}). \quad (5.29)$$

The waiting time for the bead to dissociate in this case follows the pdf $w'(t') = \lambda_{Br}^{-1} \exp(-t'/\lambda_{Br})$ as in the Lodge model. However, in gels and many soft materials, due to the entanglements, even though the thermal motion is large enough to drive the bead out of the potential well, the bead may remain stuck by other entrapments and unable to detach. The waiting time distribution $w(t)$ for the bead to overcome the barrier may stem from possible obstacles and traps that delay the particle's escape [33]. In order to capture this behavior, we model the association and dissociation process as a CTRW process so that association/dissociation lifetimes follow a heavy-tailed distribution. Specifically, we use the Mittag-Leffler waiting time distribution (4.20) for our breakage/recombination process

$$w'(t') = -\frac{d}{dt'} E_{\alpha}(-(t'/\lambda_{Br})^{\alpha}). \quad (5.30)$$

We start with an equilibrium distribution of strands following a Gaussian distribution (5.11). How long each network component will live in the ensemble is determined through the heavy-tailed Mittag-Leffler distribution (5.30). The lifetime λ_i for strand i is chosen according to the random number generator (4.22). When the simulation time is larger than λ_i , the network chain detaches and joins the equilibrium distribution. The stress carried by this chain relaxes instantly. During the lifetime λ_i , the network chains move deterministically as governed by equation (5.18). In the meantime, a new chain is created with equilibrium distribution (5.11) through the assumption that the creation and destruction have the same rates. The new chain is assigned a new random lifetime from distribution (5.30), and the chain convects with the flow as (5.18). We anticipate the configuration distribution of this stochastic process asymptotes to

$$\frac{\partial \psi'}{\partial t'} = -\frac{\partial}{\partial \mathbf{Q}'} \cdot [\boldsymbol{\kappa}' \cdot \mathbf{Q}'] \psi' + {}^C D_{t'}^{1-\alpha} \left(\frac{\psi'_{eq}}{\lambda_{Br}^{\alpha}} - \frac{\psi'}{\lambda_{Br}^{\alpha}} \right), \quad (5.31)$$

at long times. Thus, the analytical form of the stress tensor in this case is not immediately available. In the next section, stochastic simulations are performed on this model to investigate model predictions under shear flow. In the simulation, the time is scaled by λ_{Br} and length $l_H = \sqrt{k_B T / H}$.

5.5.2 Simulation Results

5.5.2.1 Inception and Cessation of Steady Shear Flow

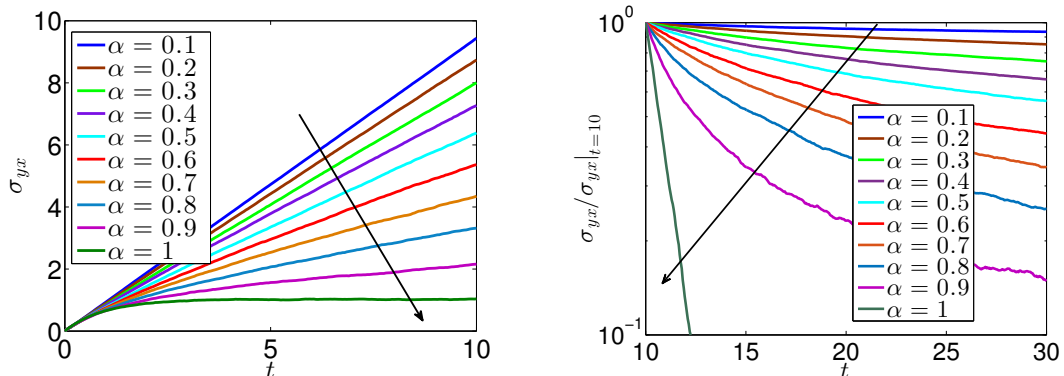


Figure 5.8: Left: The time evolution of the shear stress for the fractal Lodge network model after a constant shear rate $\dot{\gamma} = 1$ is imposed for $0 < t < 10$. The resultant stress growth for dumbbells with a Mittag-Leffler breakage/recombination processes for different α is compared. Right: The shear flow is turned off at $t = 10$. The stress relaxation is shown for simulations for different α , $0 < \alpha \leq 1$. The arrow points in the direction of increasing α values.

The stochastic simulation of network chains with a Mittag-Leffler distributed breakage/recombination processes is solved under steady homogeneous shear flow for a non-dimensional time t , $0 < t < 10$, followed by cessation of the imposed shear at $t = 10$. For $0 < t < 10$, $\mathbf{v} = (\dot{\gamma}y, 0, 0)$ and the stress growth is computed. At $t = 10$, the flow is stopped and the stress relaxation is recorded for $t \geq 10$. We compared simulations of the shear stress growth for different values α (Figure 5.8 left). Due to a heavy-tailed distribution for the waiting times of the association/dissociation processes, there exists a broad spectrum of waiting time scales thus a wide range of

relaxation time scales in the system. The attachment/detachment processes happen less frequently with a smaller α , thus, the network strands on average live longer and are stretched longer by the shear flow. This is reflected in the stress relaxation after cessation of the steady shear flow, in which the stress decay is slower with a smaller α . Specifically, when $\alpha = 1$, the model reduces to the Lodge model and predicts an exponential stress relaxation under cessation of shear flow. For $0 < \alpha < 1$, the stress relaxation is no longer exponential (Figure 5.8 right). This slower relaxation for $0 < \alpha < 1$ results because the network strands tend to stay attached for a longer time.

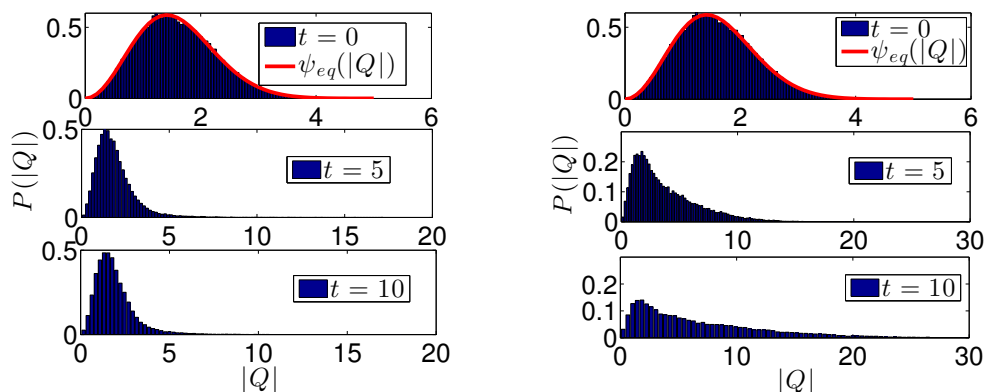


Figure 5.9: For stochastic simulation of the fractal Lodge network model with $\lambda_{Br} = 1$, the length distributions of network strands under steady shear flow for $\alpha = 1$ (left) and $\alpha = 0.3$ (right) at various times $t = 0, 5, 10$. Note the length distribution of dumbbell connector vectors is broader with $\alpha = 0.3$, in comparison with $\alpha = 1$.

In Figure 5.9, the length distribution of network strands is plotted for $\alpha = 1$, left, and $\alpha = 0.3$, right, at various times under steady shear flow. The length distribution is broader for $\alpha = 0.3$ than for $\alpha = 1$ at the same simulation time. Initially, both simulations with $\alpha = 1$ and $\alpha = 0.3$ start with the Gaussian equilibrium length distributions (5.11). At $t = 5$, the probability of finding network strands with length larger than 10 is about 2% for $\alpha = 0.3$ and 0.05% for $\alpha = 1$. At time $t = 10$, 12% of the strands have a length larger than 20 for $\alpha = 0.3$, while very few long strands

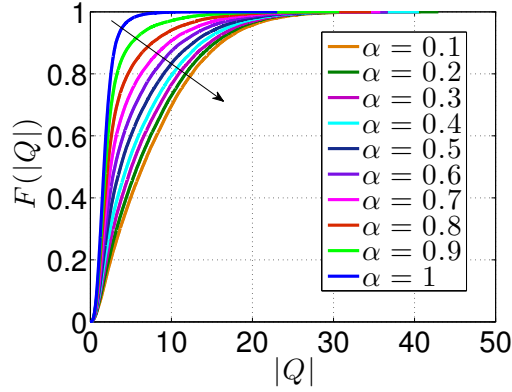


Figure 5.10: For stochastic simulation of the fractal Lodge network model with $\lambda_{Br} = 1$, the cumulative distribution $F(|Q|)$ of network strand lengths under steady shear flow for different α at $t = 10$. The arrow points in the direction of decreasing α values.

for $\alpha = 1$. The cumulative distributions of dumbbell lengths at $t = 10$ for different values of α are compared in Figure 5.10.

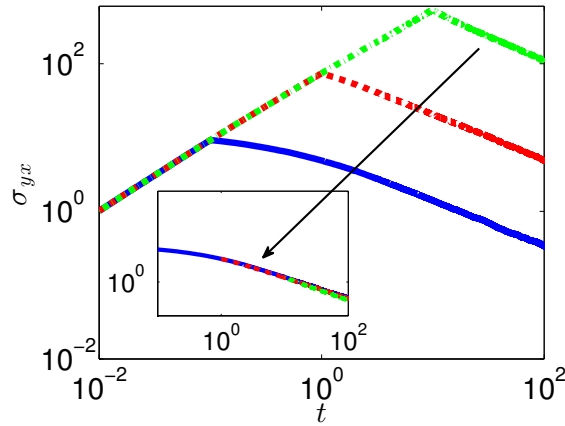


Figure 5.11: Stress evolution in time for the fractal Lodge network model after cessation of imposed shear at the various times $T_1 = 0.1$ (*blue/solid curve*), $T_1 = 1$, (*red/dashed curve*), and $T_1 = 10$ (*green/double dashed curve*). The stress relaxation of this fractal Lodge network model, can be rescaled to form a master curve. Here $\alpha = 0.6$ and $\lambda_{Br} = 1$.

A shear flow with $\dot{\gamma} = 1$ is imposed on the system for time $0 < t < T_1$. Then the system is allowed to relax with $\dot{\gamma} = 0$ for $T_1 < t < 100$. In Figure 5.11, the

time evolution of the shear stress is shown for $T_1 = 0.1$ (*blue/solid curve*), $T_1 = 1$, (*red/dashed curve*), and $T_1 = 10$ (*green/double dashed curve*). For $\alpha = 0.6$ and $\lambda_{Br} = 1$, the stress relaxation after cessation of shear flow during $0.1 < t < 100$, $1 < t < 100$ and $10 < t < 100$ falls under one master curve by shifting vertically (inset of Figure 5.11).

5.5.2.2 Step Strain Relaxation

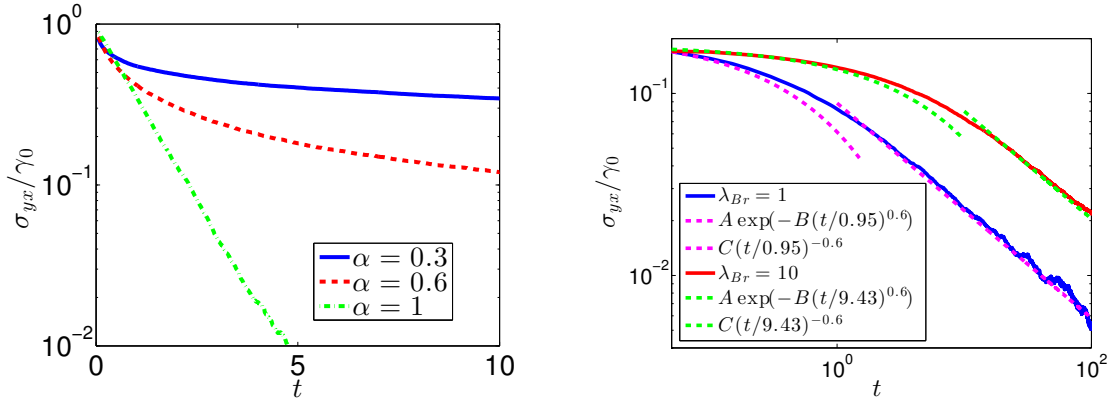


Figure 5.12: Left: Stress relaxation for the fractal Lodge network model following a step strain for parameters $\alpha = 0.3$, $\alpha = 0.6$ and $\alpha = 1$ with $\lambda_{Br} = 1$, $\gamma_0 = 10$, $b = 100$. Right: Stress relaxation following the same step strain for $\alpha = 0.6$ with $\lambda_{Br} = 1$ and $\lambda_{Br} = 10$. Both responses exhibit initial stretched-exponential behaviors for $t \ll \lambda_{Br}$ and then power-law patterns for $t \gg \lambda_{Br}$. Here, $A = 1$, $B = 1/\Gamma(\alpha + 1)$, $C = \Gamma(\alpha) \sin(\alpha\pi)/\pi$.

Following a step strain, for an α of 1, the stress decay is exponential, while for $0 < \alpha < 1$, we observe a much slower stress relaxation $\sigma_{yx} = E_\alpha(-(t/\lambda_{Br})^\alpha)$ (Figure 5.12 left). A data fitting program provided by Podlubny was used to fit the stress relaxation data with a one-parameter Mittag-Leffler function. The order of accuracy for this data fitting is 10^{-2} . When $\alpha = 1$ and $\lambda_{Br} = 1$, the relaxation modulus fit gives $G(t) = \sigma_{yx}/\gamma_0 \sim 0.95 \exp(-t)$. When $\alpha = 0.6$ and $\lambda_{Br} = 1$, $G(t) = \sigma_{yx}/\gamma_0 \sim 1.03E_{0.6}(-(t/0.95)^{0.6})$ (Figure 5.12 right). In general, the relaxation modulus $G(t)$ can

be well described by $E_\alpha(-(t/\lambda_{Br})^\alpha)$. In particular, for $t \ll \lambda_{Br}$, an initial stretched-exponential behavior is observed, and a power-law decay for $t \gg \lambda_{Br}$ is predicted.

$$G(t) = \begin{cases} \exp[-(t/\lambda_{Br})^\alpha/\Gamma(\alpha + 1)] & \text{if } t \ll \lambda_{Br} \\ \Gamma(\alpha) \sin(\alpha\pi)/\pi (t/\lambda_{Br})^{-\alpha} & \text{if } t \gg \lambda_{Br} \end{cases}$$

The solution of the Lodge network model with a heavy-tailed waiting time distribution for the breakage/recombination events naturally lead to a Mittag-Leffler function of stress relaxation. This relaxation modulus $G(t)$ agrees with the analytical form predicted by the fractional Maxwell model (FMM) with $\alpha = \beta$ as in Chapter 3. The stress decay obtained by this model can fit to power-law or stretched-exponential, or a combination of both, stress relaxation behaviors observed in experiments. This model captures a broad spectrum of different relaxation times by using a Mittag-Leffler waiting time distribution for breaking/recombination.

5.5.2.3 Small-Amplitude Oscillatory Shear

A power-law in time stress relaxation behavior implies a power-law behavior in the viscoelastic storage modulus, $G'(\omega)$, and loss modulus, $G''(\omega)$ [14]. That is, the complex modulus $G^*(\omega) = G'(\omega) + iG''(\omega)$, as a function of the driving frequency ω , is connected to the relaxation modulus through the relation [2]

$$G^*(\omega) = i\omega \int_0^\infty e^{-i\omega s} G(s) ds. \quad (5.32)$$

With $G(t) = E_\alpha(-(t/\lambda_{Br})^\alpha)$, the real part of $G^*(\omega)$ is

$$G'(\omega) = \frac{(\lambda_{Br}\omega)^\alpha \cos(\frac{\pi}{2}\alpha) + (\lambda_{Br}\omega)^{2\alpha}}{1 + 2(\lambda_{Br}\omega)^\alpha \cos(\frac{\pi}{2}\alpha) + (\lambda_{Br}\omega)^{2\alpha}}, \quad (5.33)$$

and the imaginary part

$$G''(\omega) = \frac{(\lambda_{Br}\omega)^\alpha \sin(\frac{\pi}{2}\alpha)}{1 + 2(\lambda_{Br}\omega)^\alpha \cos(\frac{\pi}{2}\alpha) + (\lambda_{Br}\omega)^{2\alpha}}. \quad (5.34)$$

This model prediction agrees with the FMM prediction with $\alpha = \beta$ under SAOS (see equation (3.20), (3.21)). When $\alpha = 1$, the storage $G'(\omega)$ and loss modulus $G''(\omega)$

intersect at $\lambda_{Br} = 1/\omega = 1$, the relaxation time of the fluid (Figure 5.13 left). As α decreases below 1, the intersection frequency of G' and G'' shifts to lower frequencies, representing an increase of the relaxation time (Figure 5.13 right). This rheological behavior has been observed in SAOS experiments of EDAB worms as the temperature is varied [28]. At low temperatures 20°C and 40°C , G' and G'' are nearly independent of ω and $G' > G''$ over the entire ω range. When $0 < \alpha < 1$, for low frequency, $G'(\omega) \sim G''(\omega) \sim \omega^\alpha$, with the ratio of $G''(\omega)/G'(\omega) \sim \tan(\pi\alpha/2)$, independent of ω . This is in contrast to the exponential relaxation obtained when $\alpha = 1$ where the ratio of $G'(\omega)$ and $G''(\omega)$ is ω (see Figure 1.3).

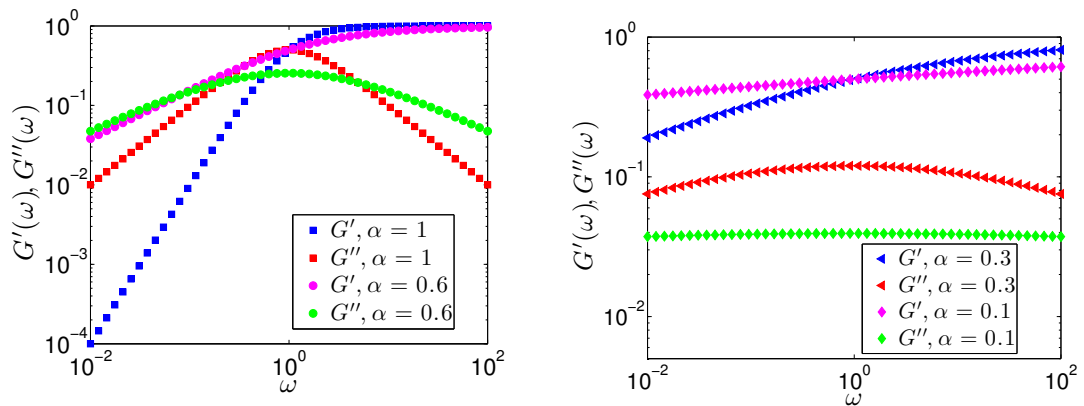


Figure 5.13: Storage modulus $G'(\omega)$ and loss modulus $G''(\omega)$ as a function of ω for different α and $\lambda_{Br} = 1$.

Figure 5.14 shows the Cole-Cole plot, which relates the behavior of the real and imaginary parts of the complex modulus, for several different values of α . For $\alpha = 1$, the Cole-Cole plot is a semicircle. This semicircle compresses vertically as α decreases. This Cole-Cole plot behavior, and the corresponding Mittag-Leffler relaxation function are the characteristic response patterns which stem from trapping simulated using the broad waiting time distribution $w(t) \sim t^{-1-\alpha}$ within the continuous time random walk scheme [19]. Cates [35] implemented a numerical simulation to study the stress relaxation in wormlike micelles governed by the interplay between simple reptation and the

breakage and recombination events. He showed that when $\lambda_{\text{break}} \ll \lambda_{\text{rep}}$, the Cole-Cole diagram approaches a semicircular shape. When $\lambda_{\text{break}} \sim \lambda_{\text{rep}}$, the Cole-Cole plot is markedly less semicircular. In the regime $\lambda_{\text{break}} \sim \lambda_{\text{rep}}$, the Cole-Cole plot behaves similarly to the curves in Figure 5.14 (away from $(G', G'') = (1, 0)$). A recent paper by Zou and Larson [40] used an innovative fast pointer simulation method to extend the model of Cates and captured experimental data of G', G'' over the entire frequency range. In their model, the simulated the Cole-Cole plot exhibited a vertically compressed shape, but simulations showed an upturn near $(G', G'') = (1, 0)$. This upturn of the Cole-Cole pattern has been observed in surfactant solutions [13]. Our simulations of the fractal Lodge network model do not include reptation or any dynamics other than breakage/recombination events.

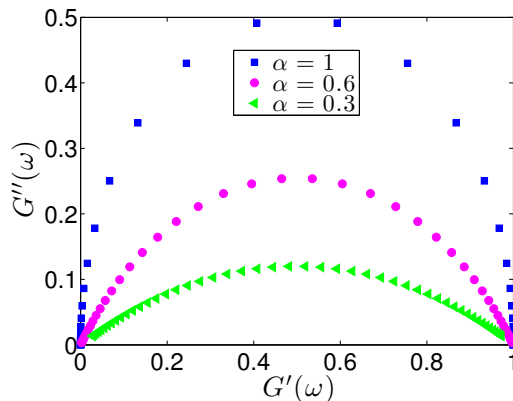


Figure 5.14: Cole-Cole plot of the storage modulus G' and loss modulus G'' associated with the fractal Lodge network model simulated stochastically for $\alpha = 0.3, 0.6$, in comparison to the semicircular shape corresponding to the exponential relaxation pattern, $\alpha = 1$.

5.6 Fractal Hybrid Lodge Network Model

5.6.1 Model Description

Considerable investigations have been carried out to model soft materials exhibiting anomalous diffusion, particularly in the subdiffusive domain where the transport is slower than that predicted by Brownian diffusion. Experimentally, Larsen and

Furst [16] used multiple particle tracking microrheology to probe the structure of soft gels by tracking the ensemble-averaged mean-squared displacement of tracer particles, $\langle \Delta r^2(t) \rangle$. That work showed that for certain soft gels the particles exhibited a power-law response $\langle \Delta r^2(t) \rangle \sim t^\beta, 0 < \beta < 1$, as opposed to a linear relation $\langle \Delta r^2(t) \rangle \sim t$. This mean-squared displacement behavior is related to a power-law relaxation modulus of the gel-like system, $G(t) \sim G_0 t^{-\beta}$, by the generalized Stokes-Einstein equation as discussed in [18]. In chapter 4, a one-dimensional subdiffusive process is derived asymptotically from a CTRW in which the waiting time distribution for particles exhibiting Gaussian jumps is heavy-tailed. To model anomalous diffusion behavior of three-dimensional fluids, we investigate CTRW processes for both the spring force and diffusion as well as breakage/recombination. The physical picture is that, in addition to convection, the microscopic structure of the materials not only can not respond smoothly to external forces or diffusive effects due to entanglements, but also can not break/reform frequently with this networked structure. In this composite model, the waiting time distributions for the spring force and the diffusion follow $w'_\beta(t') = -\frac{d}{dt'} E_\beta(-(t'/\lambda_H)^\beta)$, and the breakage and recombination events follow $w'_\alpha(t') = -\frac{d}{dt'} E_\alpha(-(t'/\lambda_{Br})^\alpha)$, respectively. The dumbbells convect with the shear flow deterministically. This model is referred as the fractional hybrid Lodge network model due to the inclusion of the CTRW processes for the spring force and Brownian motion dumbbell dynamics. The waiting times are generated using (4.22) as in Chapter 4. The time is scaled by $\lambda_H = \zeta/(4H)$ and length is scaled by $l_H = \sqrt{k_B T/H}$. The non-dimensional waiting time distributions for the elastic and diffusive motion as well as breakage/recombination are $w_\beta(t) = -\frac{d}{dt} E_\beta(-t^\beta)$ and $w_\alpha(t) = -\frac{d}{dt} E_\alpha(-t^\alpha)$, accordingly. Here $\lambda = \lambda_{Br}/\lambda_H$. The non-dimensional configuration distribution equation for this generalized hybrid Lodge network model is expected to follow

$$\frac{\partial \psi}{\partial t} = -\frac{\partial}{\partial \mathbf{Q}} \cdot [\boldsymbol{\kappa} \cdot \mathbf{Q}] \psi + {}_0^C D_t^{1-\beta} \left(\frac{1}{2} \frac{\partial}{\partial \mathbf{Q}} \mathbf{Q} \psi + \frac{1}{2} \frac{\partial^2 \psi}{\partial \mathbf{Q}^2} \right) + {}_0^C D_t^{1-\alpha} \left(\frac{\psi_{eq}}{\lambda_{Br}^\alpha / \lambda_H^\alpha} - \frac{\psi}{\lambda_{Br}^\alpha / \lambda_H^\alpha} \right), \quad (5.35)$$

in the long-time limit. Stochastic simulation of this CTRW process under shear flow is investigated below.

5.6.2 Simulation Results

Following the trajectory of one dumbbell, the dumbbell moves deterministically due to the shear flow

$$\mathbf{Q}(t + \Delta t) = \mathbf{Q}(t) + \boldsymbol{\kappa} \cdot \mathbf{Q}(t)\Delta t. \quad (5.36)$$

The CTRW processes for the spring force and diffusion requires random waiting times τ_i generated following the pdf $w_\beta(t)$. The Mittag-Leffler random number generator (4.22) was used (see Chapter 4). Once the waiting time τ_i is reached, the dumbbell connector vector makes a move due to the elastic spring force and Brownian force in addition to convecting with the flow,

$$\mathbf{Q}(t + \Delta t) = \mathbf{Q}(t) + \boldsymbol{\kappa} \cdot \mathbf{Q}(t)\Delta t + \mathbf{W} + \mathbf{Q}/2, \quad (5.37)$$

where \mathbf{W} is a random vector of normal distribution with zero mean and variance one caused by the Brownian motion and $\mathbf{Q}/2$ is the elastic spring force. In the meantime, the breaking/reforming process is simulated continuously in time as described in the fractal Lodge network model.

5.6.2.1 Equilibrium

With the addition of anomalous diffusion in this CTRW process, the mean-squared displacement is a quantity of interest. In equilibrium, the mean-squared displacement of the dumbbell vectors is measured, which is computed by averaging the dot product of vectors $\mathbf{Q}(t) - \mathbf{Q}(0)$,

$$\langle (\mathbf{Q}(t) - \mathbf{Q}(0))^2 \rangle = \frac{\sum_{i=1}^N (\mathbf{Q}_i(t) - \mathbf{Q}_i(0))^2}{N}. \quad (5.38)$$

In the force-free and no breakage/recombination limit, the dumbbells only experience diffusion and the mean-squared displacement follows $\langle (\mathbf{Q}(t) - \mathbf{Q}(0))^2 \rangle \sim t^\beta$ (Chapter 4). The inclusion of elastic forces as well as breakage/recombination processes leads to

a less significant mean-squared displacement behavior. In Figure 5.15 *left*, the mean-squared displacement of dumbbell connectors simulated with parameters $\alpha = \beta = 1$ for $\lambda = 0.1, 1, 10$ is compared. The mean-squared displacement approaches the limit $\langle (\mathbf{Q}(t) - \mathbf{Q}(0))^2 \rangle \sim t^\beta$ with a larger value of λ . In Figure 5.15 *right*, the mean-squared displacement of dumbbell connectors simulated with parameters $\alpha = \beta = 0.6$ for $\lambda = 0.1, 1, 10$ is compared. The mean-squared displacement approaches to the limit $\langle (\mathbf{Q}(t) - \mathbf{Q}(0))^2 \rangle \sim t^\beta$ with increasing λ .

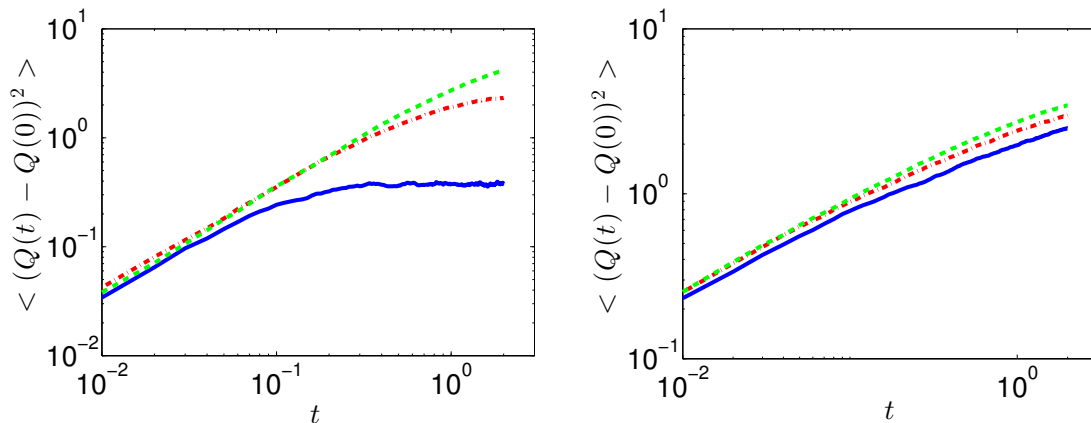


Figure 5.15: The simulation of the mean-squared displacement of bead-spring dumbbell connectors in equilibrium for $\lambda = 0.1$ (*blue/solid curve*), $\lambda = 1$ (*red/dash-dot curve*) and $\lambda = 10$ (*green/dashed curve*) for the fractal hybrid Lodge network model with CTRW processes for both breaking/reforming and spring/Brownian forces. In the left figure, $\alpha = \beta = 1$. In the right figure, $\alpha = \beta = 0.6$.

5.6.2.2 Step Strain Relaxation

Following a step strain, the stress relaxation for simulations with different values of α and β are compared. In Figure 5.16, the time scale is set to a unit value $\lambda = 1$. When $\alpha = \beta = 1$, the stress decay is mono-exponential as shown in Figure 5.16 (*blue/solid curve*). When $\alpha = \beta = 0.6$, the stress decay is non-exponential as shown in Figure 5.16 (*red/dashed curve*). This non-exponential decay is caused by the slowing down of both the spring/diffusion and breakage/recombination processes.

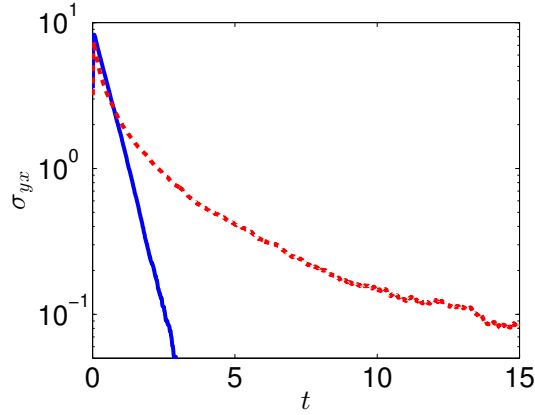


Figure 5.16: Stress relaxation following a step strain for parameters $\alpha = \beta = 1$ (blue/solid curve), and $\alpha = \beta = 0.6$ (red/dashed curve) for the fractal hybrid Lodge network model with CTRW processes for each of breakage/recombination and spring/Brownian force. Here, $\lambda = 1, \gamma_0 = 10, b = 100$.

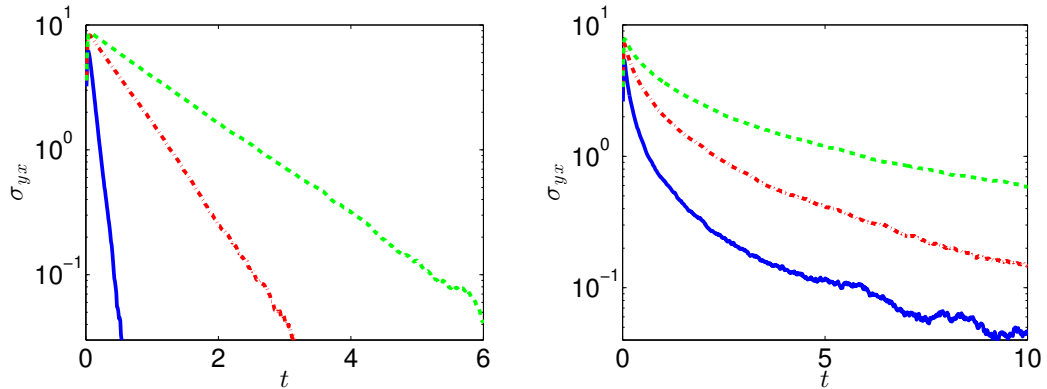


Figure 5.17: Stress relaxation following a step strain for the fractal hybrid Lodge network model with CTRW processes for each of breakage/recombination and spring/Brownian force. Left: $\alpha = \beta = 1$. The stress relaxation is exponential and the decay is compared for $\lambda = 0.1$ (blue/solid curve), $\lambda = 1$ (red/dash-dot curve), $\lambda = 10$ (green/dashed curve). Right: $\alpha = \beta = 0.6$. The stress relaxation is non-exponential and the decay is compared for $\lambda = 0.1$ (blue/solid curve), $\lambda = 1$ (red/dash-dot curve), $\lambda = 10$ (green/dashed curve).

With fixed values of α, β , stochastic simulations of stress relaxation for varying λ are presented (Figure 5.17). When $\alpha = \beta = 1$, the stress decay is exponential and the

decay rate is determined by the parameter λ (Figure 5.17 *left*). Also, when $\alpha = \beta = 0.6$, there exists subdiffusive behavior in the system as well as a slow breaking/reforming processes, the stress decay is non-exponential as shown in Figure 5.17 *right*.

5.6.2.3 Inception and Cessation of Steady Shear Flow

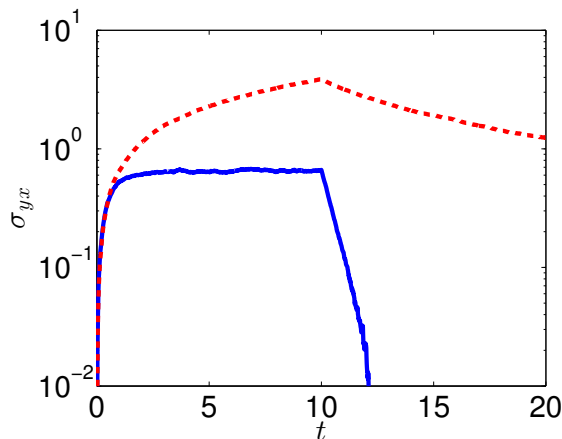


Figure 5.18: Time evolution of the shear stress after a constant shear rate $\dot{\gamma} = 1$ is imposed for $0 < t < 10$ for the fractal hybrid Lodge network model with CTRW processes for each of breakage/recombination and spring and Brownian forces. The resultant stress growth for $\alpha = \beta = 1$ (*blue/solid curve*) and $\alpha = \beta = 0.6$ (*red/dashed curve*) are compared. The shear flow is turned off at $t = 10$, the stress relaxation is shown for simulations with $\alpha = \beta = 1$ and $\alpha = \beta = 0.6$.

A shear flow with $\dot{\gamma} = 1$ is imposed for $0 \leq t \leq 10$ and then turned off with $\dot{\gamma} = 0$ for $10 \leq t \leq 20$. When $\alpha = \beta = 1$, the shear stress reaches a steady-state during $0 < t < 10$, see Figure 5.18 (*blue/solid curve*). When $\alpha = \beta = 0.6$, the shear stress is still rising as a function of time at $t = 10$, see Figure 5.18 (*red/dashed curve*). At $t = 10$, the shear rate is set to zero and the stress relaxes. For $\alpha = \beta = 1$, the stress decay is exponential and the stress relaxes instantly, see Figure 5.18 (*blue/solid curve*). For $\alpha = \beta = 0.6$, the stress relaxes much slower and exhibits a non-exponential behavior, see Figure 5.18 (*red/dashed curve*).

5.7 Two-species Network Model with Fractal Breakage and Recombination Processes

5.7.1 Model Description

In previous models, we only consider one type of chains (network chains with both ends attached) and ignore other chains, i.e. one end disconnected from the network contributing to the stress of the solution. In [7], it is suggested that dangling strands (only one end is attached and the other end is free) might also influence the stress. As a first step, we take into account two types of strands in the system: network strands and dangling strands. Let $\psi'(\mathbf{Q}'_a, t')$ be the distribution function describing the probability of finding an active dumbbell with connector vector \mathbf{Q}'_a at time t' , and $\phi'(\mathbf{Q}'_d, t')$ be the distribution function for dangling dumbbells with connector vectors \mathbf{Q}'_d . This approach has been investigated in [5, 32]. While their models are focused on examining nonlinear fluid dynamic problems, i.e. non-isotropic drag force and Q -dependent attachment/detachment rates, we want to investigate the fluid dynamics for this two-species model with a broad waiting time distribution for association/dissociation processes. The waiting time distribution for association follows:

$$w'_a(t') = -\frac{d}{dt'} E_\alpha(-(t'/\lambda_{Cr})^\alpha), \quad (5.39)$$

and the distribution for dissociation is given by:

$$w'_d(t') = -\frac{d}{dt'} E_\alpha(-(t'/\lambda_{Br})^\alpha). \quad (5.40)$$

Here λ_{Br} is the average lifetime for an associated bead and $\lambda_{Br} = \lambda_{fund} \exp(U_0/k_B T)$. λ_{fund} is the fundamental molecular time scale related to the thermal vibration and U_0 is the potential well depth[5]. Following Cifre et al [5], the average lifetime of a detached bead $\lambda_{Cr} = \lambda_H$ is assumed. The stochastic formulation for the network chains dynamics is governed by

$$\mathbf{Q}'_a(t' + \Delta t') = \mathbf{Q}'_a(t') + \boldsymbol{\kappa}' \cdot \mathbf{Q}'_a(t') \Delta t' - \frac{H D_a}{k_B T} \mathbf{Q}'_a(t') \Delta t' + \sqrt{D_a} \Delta \mathbf{W}'(t'). \quad (5.41)$$

The dangling chains move according to

$$\mathbf{Q}'_d(t' + \Delta t') = \mathbf{Q}'_d(t') + \boldsymbol{\kappa}' \cdot \mathbf{Q}'_d(t')\Delta t' - \frac{HD_d}{k_B T} \mathbf{Q}'_d(t')\Delta t' + \sqrt{D_d} \Delta \mathbf{W}'(t'). \quad (5.42)$$

Here $D_a = 2k_B T/\zeta_n$ is the diffusion constant for active dumbbells and ζ_n is the drag coefficient for attached beads. Also, $D_d = (\zeta_f + \zeta_n)k_B T/\zeta_f \zeta_n$ is the diffusion constant for dangling chains and ζ_f is the drag coefficient for the free bead. In the limit $\zeta_f \ll \zeta_n$, the network chains move affinely with the flow and $D_d = k_B T/\zeta_f$. We expect the evolution equation for the configuration distribution function of active dumbbells asymptotes to [5]:

$$\frac{\partial \psi'}{\partial t'} = - \left(\frac{\partial}{\partial \mathbf{Q}'_a} \cdot \left[(\mathbf{Q}'_a \cdot \nabla' \mathbf{v}') \psi' - \frac{D_a}{k_B T} \mathbf{F}'_s(\mathbf{Q}'_a) \psi' - D_a \frac{\partial \psi'}{\partial \mathbf{Q}'_a} \right] \right) + {}_0^C D_{t'}^{1-\alpha} \left(-\frac{\psi'}{\lambda_{Br}} + \frac{\phi'}{\lambda_{Cr}} \right), \quad (5.43)$$

and the distribution function of dangling segments asymptotes to

$$\frac{\partial \phi'}{\partial t'} = - \left(\frac{\partial}{\partial \mathbf{Q}'_d} \cdot \left[(\mathbf{Q}'_d \cdot \nabla' \mathbf{v}') \phi' - \frac{D_d}{k_B T} \mathbf{F}'_s(\mathbf{Q}'_d) \phi' - D_d \frac{\partial \phi'}{\partial \mathbf{Q}'_d} \right] \right) + {}_0^C D_{t'}^{1-\alpha} \left(\frac{\psi'}{\lambda_{Br}} - \frac{\phi'}{\lambda_{Cr}} \right), \quad (5.44)$$

in the long-time limit. Due to the complicated two-species modeling, it is difficult to obtain an analytical solution for the stress tensor. Stochastic simulations are employed to examine this model.

The time is scaled by $\lambda_H = \zeta_f/4H$ and length is scaled by $l_H = \sqrt{3k_B T/H}$. The stress is scaled by $nk_B T$. The dimensionless equation for network chains dynamics is:

$$\mathbf{Q}_a(t + \Delta t) = \mathbf{Q}_a(t) + \boldsymbol{\kappa} \cdot \mathbf{Q}_a(t)\Delta t - \frac{\zeta_f}{2\zeta_n} \mathbf{Q}_a(t)\Delta t + \sqrt{\frac{\zeta_f}{3\zeta_n}} \Delta \mathbf{W}(t). \quad (5.45)$$

The dimensionless equation for dangling chains is:

$$\mathbf{Q}_d(t + \Delta t) = \mathbf{Q}_d(t) + \boldsymbol{\kappa} \cdot \mathbf{Q}_d(t)\Delta t - \frac{\zeta_f + \zeta_n}{4\zeta_n} \mathbf{Q}_d(t)\Delta t + \sqrt{\frac{\zeta_f + \zeta_n}{6\zeta_n}} \Delta \mathbf{W}(t). \quad (5.46)$$

The non-dimensional waiting time distributions for association and dissociation are:

$$w_a(t) = -\frac{d}{dt} E_\alpha(-(t/(\lambda_{Cr} \lambda_H^{-1}))^\alpha), \quad (5.47)$$

and the distribution for dissociation is given by:

$$w_d(t) = -\frac{d}{dt}E_\alpha(-(t/(\lambda_{Br}\lambda_H^{-1}))^\alpha). \quad (5.48)$$

Association/dissociation is simulated by generating lifetimes λ_i following distribution (5.47) or (5.48) depending on the dumbbell being attached or detached. The dumbbell will switch states between attached and detached once its lifetime is reached. For a networked chain, it moves according to equation (5.45) until it detaches (the simulation time passes its lifetime). Once the networked chain detaches, it moves with dynamics following equation (5.46). In the meantime, a new lifetime following (5.48) is generated. The chain will reattach once its lifetime is reached and this whole process repeats.

5.7.2 Simulation Results

In this model, stress relaxation of network and dangling chains can happen through Brownian motion, elastic spring force and breakage/recombination. With the inclusion of the two-species, an additional dangling chain relaxation time scale is introduced into the system. We define a new parameter as suggested in [5], $Z = \lambda_n/\lambda_d = \zeta_n/\zeta_d$, where $\lambda_n = \zeta_n/(4H)$ is the relaxation time of the network chain and $\lambda_d = \zeta_d/(4H)$ is the relaxation time of the dangling chain.

5.7.2.1 Start-up and Cessation of the Steady-shear Flow

A constant shear rate $\dot{\gamma} = 1$ is imposed on the system for $0 < t < 200$ and the stress growth is computed. The shear stress growth for simulations with $Z = 10$ and $Z = 100$ is compared, for $\alpha = 1$ (Figure 5.19 *left*) and $\alpha = 0.6$ (Figure 5.20 *left*). The lifetimes for breakage and recombination are exponentially distributed when $\alpha = 1$ and heavy-tailed distributed when $\alpha = 0.6$. Both cases with $\alpha = 1$ and $\alpha = 0.6$, the shear stresses reach to steady-state with a higher steady-state value for $Z = 100$, compared with for $Z = 10$. When $Z = 100$, the network chains diffuse and experience elastic motion on a larger time scale (since $\lambda_n = \zeta_n/(4H) = Z\lambda_H$). At time $t = 200$, the imposed shear flow is turned off and the stress relaxes. The stress relaxation is faster for $Z = 10$ (Figure 5.19 *right* and Figure 5.20 *right*).

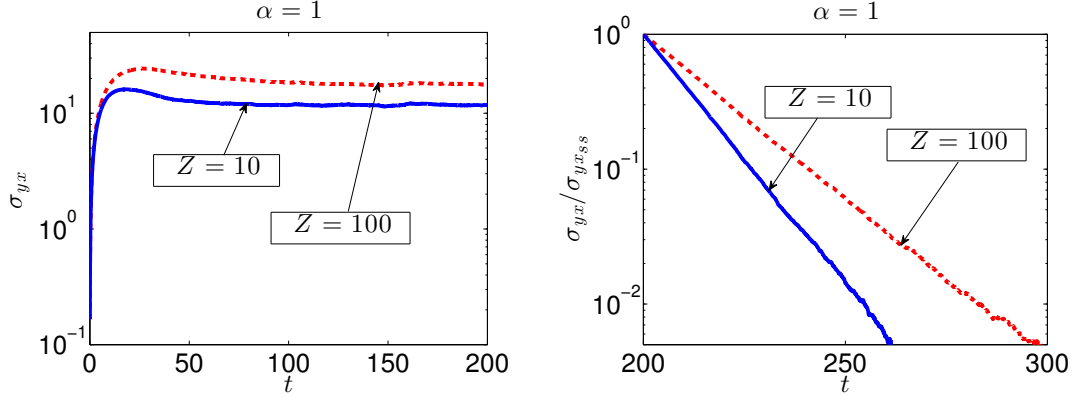


Figure 5.19: Simulations of shear stress evolution under start-up and cessation of shear flow with $\dot{\gamma} = 1$ for $0 < t < 200$ and $\dot{\gamma} = 0$ for $200 < t < 300$ for the two-species network model with fractal breakage/recombination processes. Here $\alpha = 1$. Left: The shear stress σ_{yx} grows as a function of time for $Z = 10$ (blue/solid curve) and $Z = 100$ (red/dashed curve). Right: The scaled shear stress $\sigma_{yx}/\sigma_{yx_{ss}}$ decays as a function of time for $Z = 10$ (blue/solid curve) and $Z = 100$ (red/dashed curve), where $\sigma_{yx_{ss}}$ is the steady-state value of the shear stress under start-up shear flow.

Also, the shear stress evolution is compared for $\alpha = 1$ and $\alpha = 0.6$ with fixed $Z = 10$. When $\alpha = 0.6$, the lifetimes for breakage and recombination are broadly distributed and there exists a spectrum of relaxation time scales for association/dissociation processes. This results in a slower stress relaxation due to breakage/recombination processes compared with $\alpha = 1$. The shear stress growth for simulations with $\alpha = 1$ and $\alpha = 0.6$ is compared (Figure 5.21 left). The shear stress reaches a higher steady-state value for $\alpha = 0.6$ due to less stress relaxation contribution from the breaking/reforming processes, compared with $\alpha = 1$. For $\alpha = 0.6$, we observe a slower stress decay compared to that with $\alpha = 1$ (Figure 5.21 right). However, for this long shearing process (the shear flow is turned off at $t = 100$), the stress relaxation for $\alpha = 0.6$ is dominated by the network and dangling chains relaxation and the decay exhibits an exponential behavior.

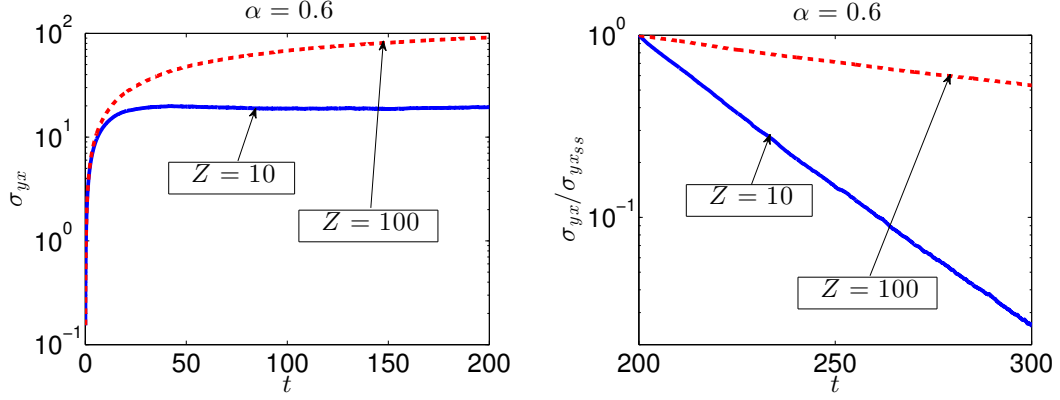


Figure 5.20: Simulations of shear stress evolution under start-up and cessation of shear flow with $\dot{\gamma} = 1$ for $0 < t < 200$ and $\dot{\gamma} = 0$ for $200 < t < 300$ for the two-species network model with fractal breakage/recombination processes. Here $\alpha = 0.6$. Left: The shear stress σ_{yx} grows as a function of time $Z = 10$ (blue/solid curve) and $Z = 100$ (red/dashed curve). Right: The scaled shear stress $\sigma_{yx}/\sigma_{yx_{ss}}$ decays as a function of time for $Z = 10$ (blue/solid curve) and $Z = 100$ (red/dashed curve), where $\sigma_{yx_{ss}}$ is the steady-state value of the shear stress under start-up shear flow.

5.7.2.2 Step Strain Experiment

Under a step strain experiment, the shear stress decay for simulations with $Z = 10$ and $Z = 100$ is compared, for $\alpha = 1$ (Figure 5.22 left) and $\alpha = 0.6$ (Figure 5.22 right). For $\alpha = 1$, the stress relaxation is exponential for both $Z = 10$ and $Z = 100$ and the decay rate is faster with $Z = 10$. For $\alpha = 0.6$, the simulated stress exhibits an initial non-exponential behavior and an exponential pattern for larger time. This initial non-exponential decay is resulted from the heavy-tailed waiting time distribution for the association/dissociation processes and the stress decay is taken over by the dumbbell relaxation of the network and dangling chains in the long time limit.

Also, the stress relaxation is compared for $\alpha = 0.6$ and $\alpha = 1$, with $Z = 10$ (Figure 5.23). A slower stress relaxation is observed for $\alpha = 0.6$, as compared with an exponential stress decay for $\alpha = 1$. The non-exponential relaxation behavior resulting from the Mittag-Leffler process for breakage/recombination is observed initially after applying a step strain for $\alpha = 0.6$. Then the relaxation due to diffusional and spring

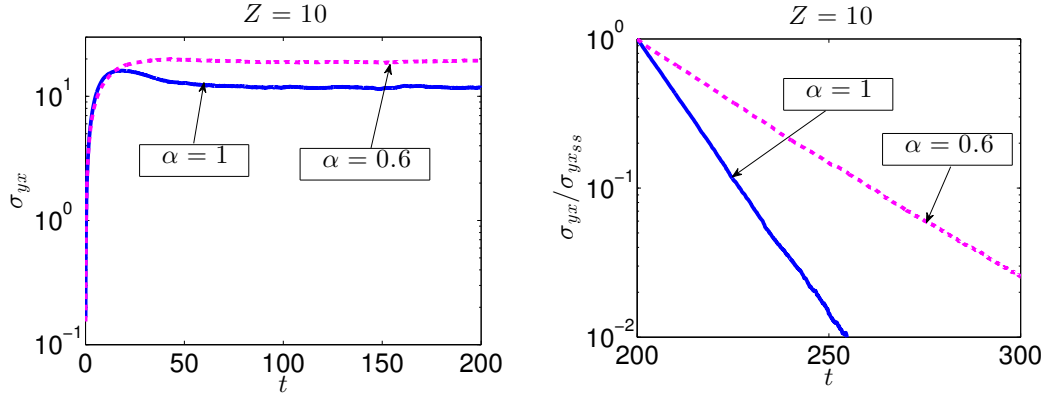


Figure 5.21: Simulations of shear stress evolution under start-up and cessation of shear flow with $\dot{\gamma} = 1$ for $0 < t < 200$ and $\dot{\gamma} = 0$ for $200 < t < 300$ for the two-species network model with fractal breakage/recombination processes. Here $Z = 10$. Left: The shear stress σ_{yx} grows as a function of time for $\alpha = 1$ (*blue/solid curve*) and $\alpha = 0.6$ (*magenta/dashed curve*). Right: The scaled shear stress $\sigma_{yx}/\sigma_{yx_{ss}}$ decays as a function of time for $\alpha = 1$ (*blue/solid curve*) and $\alpha = 0.6$ (*magenta/dashed curve*), where $\sigma_{yx_{ss}}$ is the steady-state value of the shear stress under start-up shear flow.

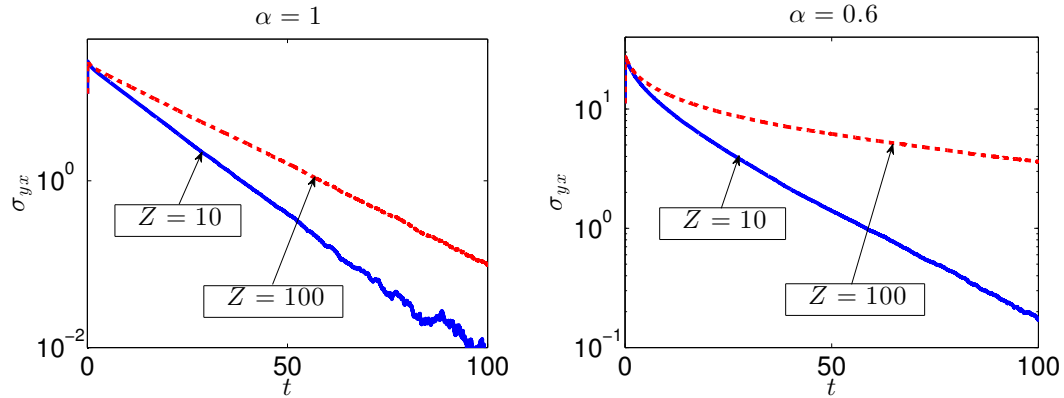


Figure 5.22: Stress relaxation under a step strain is plotted for the two-species network model with fractal breakage/recombination processes. Left: The stress decay is compared for $Z = 10$ (*blue/solid curve*) and $Z = 100$ (*red/dashed curve*) with $\alpha = 1$. Right: The stress decay is compared for $Z = 10$ (*blue/solid curve*) and $Z = 100$ (*red/dashed curve*) with $\alpha = 0.6$.

force of both network chains and dangling chains takes over at a longer time, thus, the

stress decay exhibits an exponential pattern at long times.

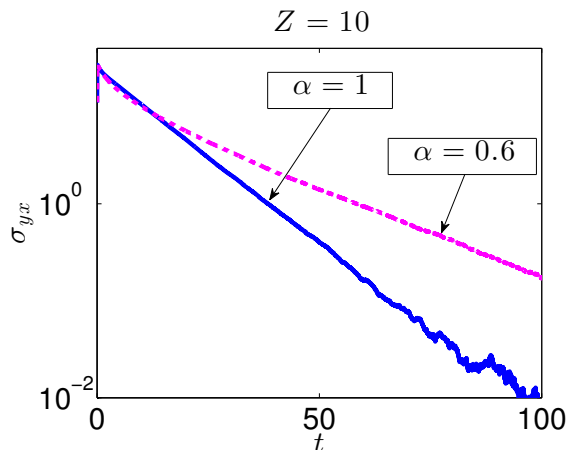


Figure 5.23: Stress relaxation under a step strain is plotted for the two-species network model with fractal breakage/recombination processes with $\alpha = 1$ (blue/solid curve) and $\alpha = 0.6$ (magenta/dashed curve). Here $Z = 10$.

In this two-species model, both networked chains and dangling chains contribute to the stress of the system. Both types of chains experience stress decay from diffusional motion as well as the breaking and recombination events. The Langevin dynamics of both dangling and active chains are formulated based on the Fokker-Planck equations. The effect of the Mittag-Leffler breakage/recombination processes in stress relaxation behavior is investigated for cessation of steady shear flow and step strain experiments. The breakage/recombination with a heavy-tailed distribution of waiting times leads to a slower stress decay. However, in this model, due to the dominance of the diffusion and spring force, the effect of the slower breakage/recombination process is relatively less apparent. A rescale of the process using the breakage/recombination time scale can separate out the stress relaxation resulted from spring force and diffusion motion or breakage/recombination. In the next section, a subordinated process for the two-species model is examined, in which the whole process is slowed down instead of only the breakage/recombination processes.

5.8 Two-species Network Model with Subordinated Langevin Process

For highly networked and concentrated soft material systems, the chains occasionally freeze and can not move or break/reform freely. For such systems, one can generalize the two-species network model to a fractional version. The evolution of the configuration distribution for the dangling chains follows

$$\frac{\partial \psi'}{\partial t'} = -{}_0^C D_{t'}^{1-\beta} \left\{ \left(\frac{\partial}{\partial \mathbf{Q}'_a} \cdot \left[(\mathbf{Q}'_a \cdot \nabla' \mathbf{v}') \psi' - \frac{D_a}{k_B T} \mathbf{F}'_s(\mathbf{Q}'_a) \psi' - D_a \frac{\partial \psi'}{\partial \mathbf{Q}'_a} \right] \right) - \frac{\psi'}{\lambda_{Br}} + \frac{\phi'}{\lambda_{Cr}} \right\}, \quad (5.49)$$

for the network strands,

$$\frac{\partial \phi'}{\partial t'} = -{}_0^C D_{t'}^{1-\beta} \left\{ \left(\frac{\partial}{\partial \mathbf{Q}'_d} \cdot \left[(\mathbf{Q}'_d \cdot \nabla' \mathbf{v}') \phi' - \frac{D_d}{k_B T} \mathbf{F}'_s(\mathbf{Q}'_d) \phi' - D_d \frac{\partial \phi'}{\partial \mathbf{Q}'_d} \right] \right) + \frac{\psi'}{\lambda_{Br}} - \frac{\phi'}{\lambda_{Cr}} \right\}. \quad (5.50)$$

This generalization is done by replacing the time derivative of the two-species model with a fractional order time derivative. This model is solved using subordination method as introduced in Chapter 4.

5.8.1 Model Description

This stochastic process for this subordinated two-species network model can be identified as the subordination of two fundamental processes $\mathbf{Q}(S_t)$, where $\mathbf{Q}(\tau)$ is the dumbbell trajectory following the Langevin dynamics for the two-species network model and S_t is the subordinator as in Chapter 4. A sample trajectory $\mathbf{Q}(S_t)$ of this subordinated Langevin dynamics on the lattice $\{t_i = i\Delta t : i = 0, 1, \dots, N\}$ requires simulation of the standard Langevin process $\mathbf{Q}(\tau)$ and the values $S_{t_0}, S_{t_1}, \dots, S_{t_N}$ of the subordinator S_t . The stochastic formulation for the network chains dynamics are governed by

$$\mathbf{Q}(\tau + \Delta\tau) = \mathbf{Q}(\tau) + \boldsymbol{\kappa} \cdot \mathbf{Q}(\tau) \Delta\tau - \frac{\zeta_f}{2\zeta_n} \mathbf{Q}(\tau) \Delta\tau + \sqrt{\frac{\zeta_f}{3\zeta_n}} \Delta \mathbf{W}(\tau), \quad (5.51)$$

for the dangling chains,

$$\mathbf{Q}(\tau + \Delta\tau) = \mathbf{Q}(\tau) + \boldsymbol{\kappa} \cdot \mathbf{Q}(\tau) \Delta\tau - \frac{\zeta_f + \zeta_n}{4\zeta_n} \mathbf{Q}(\tau) \Delta\tau + \sqrt{\frac{\zeta_f + \zeta_n}{6\zeta_n}} \Delta \mathbf{W}(\tau). \quad (5.52)$$

The association/dissociation process is simulated using the continuous time simulation. The waiting time distribution for association follows:

$$w_a(\tau) = 1/\lambda_{Cr} \exp(-\tau/\lambda_{Cr}) \quad (5.53)$$

and the distribution for dissociation is given by:

$$w_d(\tau) = 1/\lambda_{Br} \exp(-\tau/\lambda_{Br}). \quad (5.54)$$

An index k satisfying the condition $\tau_k \leq S_{t_i} \leq \tau_{k+1}$ can be found. Applying the linear interpolation to approximate the dumbbell connector vector $\mathbf{Q}(S_{t_i})$ at t_i ,

$$\mathbf{Q}(S_{t_i}) = \frac{\mathbf{Q}(\tau_{k+1}) - \mathbf{Q}(\tau_k)}{\tau_{k+1} - \tau_k} (S_{t_i} - \tau_k) + \mathbf{Q}(\tau_k) \quad (5.55)$$

A sample trajectory $\mathbf{Q}(S_{t_0}), \mathbf{Q}(S_{t_1}), \dots, \mathbf{Q}(S_{t_N})$ can be obtained through the above linear interpolation [17]. The equivalence of this subordinated Langevin process to the fractional two-species model requires more theoretical support. As mentioned in Chapter 4, for a one-dimensional fractional Fokker-Planck model, it has been suggested by [17] that the subordination method predicts a stochastic process equivalent to that of the FFPE. For a three-dimensional fluid dynamics model, we anticipate such equivalence holds true and numerical solutions for the stresses are presented below.

5.8.2 Simulation Results

In this model, both network chains and dangling chains relax their stress through Brownian motion, elastic spring force and breakage/recombination. Due to a rescale of the time scale using the subordinator S_t , the underlying stochastic processes of the dumbbells are heavy-tailed. The fractional derivative order β controls how slow the whole network dynamics are. When $\beta = 1$, this reduces to the standard two-species network model. When $0 < \beta < 1$, the chains get trapped occasionally and cannot move/break after a long time. The parameter Z controls the ratio of the network relaxation time and the dangling chain relaxation time, $Z = \lambda_n/\lambda_d = \zeta_n/\zeta_d$.

5.8.2.1 Inception and Cessation of Steady Shear Flow

The stochastic simulation of dumbbells with a subordinated Langevin dynamics is solved under start-up shear flow with $\dot{\gamma} = 1$ for $0 < t < 150$, followed by cessation of the imposed shear with $\dot{\gamma} = 0$ at $t = 150$. Here $\beta = 0.6$. The time evolution of shear stress is computed for $Z = 10$ and $Z = 100$. For both cases, the stress σ_{yx} reaches to steady-state, with a higher steady-state value for a larger Z (Figure 5.24 left). Also, the stress relaxation for the subordinated process after cessation of shear flow is non-exponential with a slower decay when Z is larger (Figure 5.24 right). This is due to the slower stress relaxation process resulted from the diffusional motion and the elastic spring response of the network chains when the bigger Z is chosen.

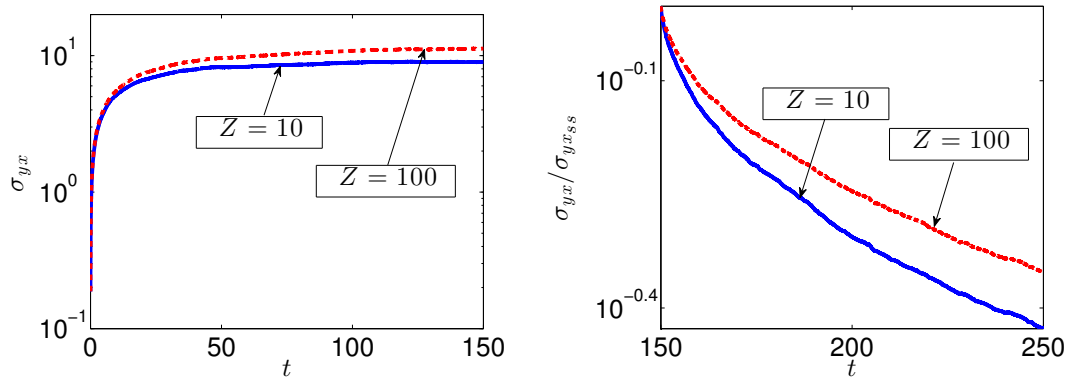


Figure 5.24: The evolution of the shear stress for the subordinated two-species network model under start-up and cessation of shear flow for $\dot{\gamma} = 1$ for $0 < t < 150$ and $\dot{\gamma} = 0$ for $150 < t < 250$. Here $\beta = 0.6$. Left: Stress growth is compared for $Z = 10$ (*blue/solid curve*) and $Z = 100$ (*red/dashed curve*). Right: Stress relaxation is compared for $Z = 10$ (*blue/solid curve*) and $Z = 100$ (*red/dashed curve*).

5.8.2.2 Step Strain Relaxation

Following a step strain, for $\beta = 0.6$, the simulated shear stress relaxation exhibits a non-exponential decay (Figure 5.25). When $Z = 100$, the network chains exhibit slow diffusional motion and elastic spring force, thus, it leads to a slower system relaxation behavior compared with $Z = 10$. When $Z \rightarrow \infty$, the network chains

move with the macro flow and only relax their stress through breaking/reforming. The subordinated two-species network model describes transient network models with highly concentrated structure, in which the segments/dumbbells become immobilized occasionally. The subordination method provides a convenient way to track the dumbbell connector vectors for networked systems with trapping events, and the simulated network/dangling chains dynamics are heavy-tailed with the composite of the standard Langevin dynamics and the subordinator.

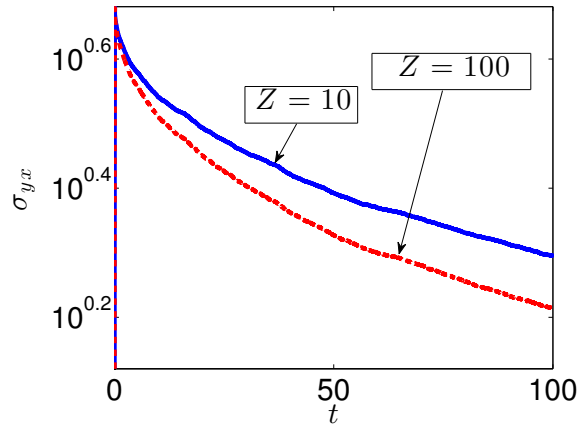


Figure 5.25: The shear stress relaxation for the subordinated two-species network model following a step strain for $Z = 10$ (blue/solid curve) and $Z = 100$ (red/dashed curve). Here $\beta = 0.6$.

Chapter 6

CONCLUSION

Rheological experiments have been carried out on soft material systems under various shear flows, e.g. step strain and small-amplitude oscillatory shear flows [22, 28]. Power-law/stretched-exponential stress relaxation dynamics were observed in these experiments for many of the soft material systems. Of particular interest to this thesis was the development of stochastic models that could capture the stress relaxation behavior of these materials in the small strain limit.

In this thesis, classical constitutive models developed for modeling materials exhibiting both viscous and elastic properties were reviewed, models such as the upper-convected Maxwell (UCM) model, the Giesekus model, and the Vasquez-Cook-McKinley (VCM) model. These classical models predict an exponential stress decay in the linear viscoelastic limit. One approach to describe non-exponential stress relaxation dynamics, e.g. power-law relaxation, is to generalize the classical constitutive models to fractional models, in which the time derivative is replaced by a fractional derivative [14]. This modeling approach lacks a direct connection to the underlying physics of the soft material system. Cates [4] proposed an equilibrium model for living polymers, in which the chains can reptate (a snake-like motion to diffuse from neighboring chains) as well as break/reform. That model predicted a transition from mono-exponential stress decay to a long-time stretched-exponential decay as the ratio of the two relaxation time scales, λ_{rep} and λ_{break} , varied. That model was an equilibrium model and thus difficult to formulate in nonequilibrium flow conditions.

For systems exhibiting non-exponential relaxation behavior or anomalous diffusion, continuous time random walk (CTRW) models and fractional Fokker-Planck equations have been considered [20]. An ensemble of particle trajectories simulated

using the CTRW approach, or the subordination method, was used to describe the particle dynamics modeled by a fractional Fokker-Planck equation for $\psi(x, t)$. Here $\psi(x, t)$ is the probability density distribution of finding a particle at position x at time t . The simulation algorithms for the CTRW approach and for the subordination method for the subdiffusion case are provided in [10] and [17], respectively. In this thesis, we extended the simulation methods of [10, 17] to describe particle dynamics with subdiffusion under the influence of the external velocity or force field (using a CTRW and a subordination simulation). The time evolution of the probability density distribution of particle positions simulated using a CTRW, or the subordination method, was presented and compared with that of the distribution described by the fractional equation [20]. The simulated mean-squared displacement of particle trajectories using these two approaches was compared with the analytical form, obtained by taking the second moment of the fractional Fokker-Planck equation [20]. Simulation methods using CTRW and subordination were tested for one-dimensional systems. The model predictions suggest that the internal dynamics of soft material systems with anomalous transport could be modeled as CTRW processes or subordinated Langevin dynamics.

We then reviewed a soft material system modeled as a three-dimensional network with elastically active connectors, in which Hookean bead-spring dumbbells were used as the fundamental units. Exemplar network models (without tracking the topology of the network) were simulated stochastically and analytically, e.g. the dumbbell model, the Lodge network model, and a hybrid network model combining the dynamics of the dumbbell model and the breakage/recombination processes. The time evolution of the configuration distributions, following stochastic processes described by these models, is equivalent to their Fokker-Planck equations. Thus, closed form constitutive equations for the stress tensor were considered by taking the second moment of the configuration distribution functions [3]. The associated constitutive equations for the dumbbell model and those for the Lodge network model both agree with the UCM model of continuum mechanics. The analytical form of the stress tensor allows us to check the simulated stress relaxation predictions for these models after cessation of

shear flow, or following a step strain, in which the stress relaxation decays exponentially $\sigma_{yx} = 1 - \exp(-t/\lambda)$, with $\lambda = \lambda_H$ for the dumbbell model and $\lambda = \lambda_{Br}$ for the Lodge network model. Here the two mesoscopic time scales are: λ_H (which is the relaxation time of a free dumbbell), and λ_{Br} (which is the breakage time scale). For the hybrid model, the system relaxes exponentially with a system relaxation time λ_{sys} , which depends on λ_{Br} and λ_H . The system relaxation can be dominated by either diffusional and elastic motion of the dumbbells, or breaking/reforming processes, depending on the size of the two time scales λ_H, λ_{Br} . The simulation results agree with the analytical prediction of the stress tensor.

On the basis of non-exponential stress relaxation and subdiffusion of tracer particles observed in soft material systems in experiments, in this thesis a new approach was taken by generalizing the transient network models to include CTRW, or subordinated Langevin, processes. In order to capture a broad spectrum of relaxation time scales in the soft material systems, we extended the Lodge network model to include a heavy-tailed waiting time distribution for the breakage/recombination processes. A Mittag-Leffler waiting time distribution was employed $w(t) = -\frac{d}{dt}E_\alpha(-(t/\lambda_{Br})^\alpha)$ as suggested in the one-dimensional CTRW process. The dumbbells convect with the bulk flow deterministically. We showed that a Mittag-Leffler stress relaxation following a step strain is predicted through stochastic simulation, in which the decay shows an initial stretched-exponential behavior for short time $t \ll \lambda_{Br}$ and a power-law pattern for large times $t \gg \lambda_{Br}$. This heavy-tailed distribution for breakage/recombination directly relates to a non-exponential stress relaxation behavior.

For the fractal Lodge network model, the network chains are assumed to move with the bulk flow and do not experience elastic spring force or Brownian motion. In order to capture the subdiffusion observed in soft gels through microrheology experiments, we added to the fractal Lodge network model a CTRW process for the elastic and Brownian chain dynamics. A heavy-tailed waiting time distribution $w(t) = -\frac{d}{dt}E_\beta(-(t/\lambda_H)^\beta)$ was used for the intramolecular and also for the intermolecular dynamics of the dumbbells. We anticipated the configuration distribution for this

stochastic process to be of a fractional Fokker-Planck type in the long-time limit. In equilibrium, the time evolution of ensemble-averaged mean-squared displacement of dumbbell connectors was subdiffusive with $0 < \beta < 1$ in the absence of the spring force term and the breakage/reforming processes. When the waiting times for both the elastic force/Brownian motion and breakage/recombination are both exponentially distributed ($\alpha = \beta = 1$), this model predicts an exponential stress relaxation under step strain or after cessation of shear flow. When the waiting times for both the elastic force/Brownian motion and breakage/recombination are heavy-tailed distributed (e.g. $\alpha = \beta = 0.6$), the shear stress decay is of a non-exponential pattern.

The above two new models are variants of the Lodge network model to enable simulation of non-exponential stress decay of soft gels. The Lodge network model is a one-species model and only takes into consideration the network components in the system. As pointed out in [7], the dangling chains with one end attached to the network and one end free carry a fair amount of stress. It is important to include both network chains and dangling chains in the model. We thus investigated the effect of a slow breakage/recombination process in a two-species transient network model [5]. With the addition of dangling chain dynamics, this model introduced an additional network relaxation time scale into the system, besides the breakage/recombination time scale and the free dumbbell relaxation time scale. The Mittag-Leffler breakage/recombination processes slow down the stress relaxation of the system described by this two-species model. Due to the dominance of the diffusional motion and elastic force relaxation of the dangling chains, the Mittag-Leffler stress relaxation resulting from a slow breakage/recombination process is only observed for a short time, then the stress decay is dominated by an exponential decay.

For a highly concentrated network system, in which the strands get trapped by the entanglements, we also considered a generalization of the two-species network model to a fractional version by replacing the time derivative with a fractional order time derivative. This model was simulated using subordinated Langevin dynamics. The composite of the standard Langevin dynamics for the two-species model and the

subordinator allows a rescale of the time axis and this reflects a heavy-tailed waiting time distributions for the underlying network dynamics. This model is simulated for start-up and cessation of shear flow as well as step strain experiment, a non-exponential stress relaxation behavior was discovered.

To conclude, we proposed generalizations of transient network models by including the CTRW process and by including subordinated Langevin dynamics. Stochastic simulation of the chain dynamics enabled us to investigate the influence of the CTRW, and of the subordinated Langevin processes, on stress relaxation following a step strain or cessation of shear flow. Our models successfully predicted non-exponential stress relaxation behavior of soft material systems. This stochastic modeling approach closely connects with the underlying physics of the microstructure of the networked system and captured the relaxation spectra of the networked system. Although in this work we focus on the phenomenological transient network models, it is of great interest to extend the physical transient network model developed by van den Brule and Hoogerbrugge [7] by including a heavy-tailed waiting time distribution for the association/dissociation processes. This approach may capture and predict soft materials' fluid dynamics under both homogeneous and non-homogeneous flow conditions. We anticipate that taking into account non-exponential breakage/recombination events, as quantified by our approach, could lead to non-exponential relaxation dynamics in van den Brule's model.

BIBLIOGRAPHY

- [1] M.P. Allen. *Computer Simulation of Liquids*. Oxford Science Publications, 1989.
- [2] R.B. Bird, C.F. Curtiss, R.C. Armstrong, and O. Hassager. *Dynamics of Polymeric Liquids: Volume 1, Fluid Mechanics*. John Wiley and Sons, New York, second edition edition, 1987.
- [3] R.B. Bird, C.F. Curtiss, R.C. Armstrong, and O. Hassager. *Dynamics of Polymeric Liquids: Volume 2, Kinetic Theory*. John Wiley and Sons, New York, second edition edition, 1987.
- [4] M.E. Cates. Reptation of living polymers: Dynamics of entangled polymers in the presence of reversible chain-scission reactions. *Macromolecules*, 20:2289–2296, 1987.
- [5] G.H. Cifre, Th.M.A.O.M. Barenbrug, J.D. Schieber, and B.H.A.A.van den Brule. Brownian dynamics simulation of reversible polymer networks under shear using a non-interacting dumbbell model. *J. Non-Newt. Fluid Mech*, 112:73–96, 2003.
- [6] P.G. de Gennes. *Scaling Concepts in Polymer Physics*. Cornell University Press, 1979.
- [7] B.H.A.A.van den Brule and P.J. Hoogerbrugge. Brownian dynamics simulation of reversible polymeric networks. *J. Non-Newt. Fluid Mech*, 60:303–334, 1995.
- [8] M. Doi and S.F. Edwards. *The Theory of Polymer Dynamics*. Oxford Science Publications, 1986.
- [9] B. Dybiec and E. Gudowska-Nowak. Subordinated diffusion and continuous time random walk asymptotics. *Chaos*, 20(043129), 2010.
- [10] D. Fulger, E. Scalas, and G. Germano. Monte Carlo simulation of uncoupled continuous-time random walks yielding a stochastic solution of the space-time fractional diffusion equation. *Phys. Rev. E.*, 77(021122), 2008.
- [11] H. Giesekus. A simple constitutive equation for polymer fluids based on the concept of deformation-dependent tensorial mobility. *J. Non-Newt. Fluid Mech*, 11:69–109, 1982.

- [12] M.S. Green and A.V. Tobolsky. A new approach to the theory of relaxing polymeric media. *J. Chem. Phys.*, 14:80–92, 1945.
- [13] S.J. Haward and G.H. McKinley. Stagnation point flow of wormlike micellar solutions in a microfluidic cross-slot device: Effects of surfactant concentration and ionic environment. *Phys. Rev. E*, 85(031502), 2012.
- [14] A. Jaishankar and G.H. McKinley. Power-law rheology in the bulk and at the interface: Quasi-properties and fractional constitutive equations. *Proc. R. Soc. A*, 469:2149–2168, 2013.
- [15] P. Kollmannsberger and B. Fabry. Linear and nonlinear rheology of living cells. *Annu. Rev. Mater. Res.*, 41:75–97, 2011.
- [16] T.H. Larsen and E.M. Furst. Microrheology of the liquid-solid transition during gelation. *Phys. Rev. Lett.*, 100:146001, Apr 2008.
- [17] M. Magdziarz and A. Weron. Fractional Fokker-Planck dynamics: Stochastic representation and computer simulation. *Phys. Rev. E.*, 75(016708), 2007.
- [18] T.G. Mason. Estimating the viscoelastic moduli of complex fluids using the generalized stokes-einstein equation. *Rheol. Acta*, 39:371–378, 2000.
- [19] R. Metzler and J. Klafter. From stretched-exponential to inverse power-law: fractional dynamics, Cole-Cole relaxation processes, and beyond. *J. Non-Crystalline Solids*, 305:81–87, 2002.
- [20] Ralf Metzler and Joseph Klafter. The random walk’s guide to anomalous diffusion: The random walk’s guide to anomalous diffusion: a fractional dynamics approach. *Phys. Reports*, 339:1–77, 2000.
- [21] F.A. Morrison. *Understanding Rheology*. Oxford University Press, 2001.
- [22] T.S.K. Ng and G.H. McKinley. Power law gels at finite strains: The nonlinear rheology of gluten gels. *J. Rheol.*, 52(2):417–449, 2008.
- [23] T. Nonnenmacher. Fractional relaxation equations for viscoelasticity and related phenomena. *Rheological Modeling: Thermodynamical and Statistical Approaches*, 7:309–320, 1991.
- [24] K.B. Oldham and J. Spanier. *The Fractional Calculus*. Dover publications, INC., 2002.
- [25] H.C. Ottinger. *Stochastic Processes in Polymeric Fluids*. Springer, 1996.
- [26] C.J. Pipe, N.J. Kim, P.A. Vasquez, L.P. Cook, and G.H. McKinley. Wormlike micellar solutions: II. comparison between experimental data and scission model predictions. *J. Rheol.*, 54:881–913, 2010.

- [27] I. Podlubny. *Fractional Differential Equations*. Academic Press, 1999.
- [28] S.R. Raghavan and J.F. Douglas. The conundrum of gel formation by molecular nano fibers, wormlike micelles, and filamentous proteins: gelation without cross-links? *Soft Matter*, 8:8539–8546, 2012.
- [29] H. Rehage and H. Hoffmann. Viscoelastic surfactant solutions: model systems for rheological research. *Molecular Physics*, 74(5):933–973, 1991.
- [30] H. Schiessel, R. Metzler, A. Blumen, and T.F. Nonnenmacher. Generalized viscoelastic models: their fractional equations with solutions. *J. Phys. A: Math. Gen.*, 28:6567–6584, 1995.
- [31] G.W. Scott-Blair. The role of psychophysics in rheology. *J. Colloid Science*, 2:21–32, 1947.
- [32] M. Seimenis and L. E. Wedgewood. A network model with free-strand dynamics for polymer melts. *Rheol. Acta*, 41:93–102, 2002.
- [33] I.M. Sokolov, J. Klafter, and A. Blumen. Fractional kinetics. *Phys. Today*, 2002.
- [34] B. Suki, A.L. Barabasi, and K.R. Lutchien. Lung tissue viscoelasticity: a mathematical framework and its molecular basis. *J. Appl. Physiol*, 76:2749–2759, 1994.
- [35] M.S. Turner and M.E. Cates. Linear viscoelasticity of living polymers: a quantitative probe of chemical relaxation times. *Langmuir*, 7:1590–1594, 1991.
- [36] P.A. Vasquez, G.H. McKinley, and L.P. Cook. A network scission model for wormlike micellar solutions: I. model formulation and viscometric flow predictions. *J. Non-Newton. Fluid Mech*, 144:122–139, 2007.
- [37] H.H. Winter and F. Chambon. Analysis of linear viscoelasticity of a crosslinking polymer at the gel point. *J. Rheol.*, 30:367–382, 1986.
- [38] P. Yang, Y.C. Lam, and K.Q. Zhu. Constitutive equation with fractional derivatives for the generalized UCM model. *J. Non-Newtonian Fluid Mech.*, 165:88–97, 2010.
- [39] L. Zhou, P.A. Vasquez, L.P. Cook, and G.H. McKinley. Modeling the inhomogeneous response and formation of shear bands in steady and transient flows of entangled liquids. *J. Rheol.*, 52(2):591–623, 2007.
- [40] W. Zou and R.G. Larson. A mesoscopic simulation method for predicting the rheology of semidilute wormlike micellar solutions. *J. Rheol.*, 58:681–721, 2014.

Appendix
REPRINT PERMISSION LETTERS

**THE SOCIETY OF RHEOLOGY LICENSE
TERMS AND CONDITIONS**

Dec 07, 2014

This is a License Agreement between YUN ZENG ("You") and The Society of Rheology ("SoR") provided by Copyright Clearance Center ("CCC"). The license consists of your order details, the terms and conditions provided by The Society of Rheology , and the payment terms and conditions.

All payments must be made in full to CCC. For payment instructions, please see information listed at the bottom of this form.

License Number	3495060086360
Order Date	Oct 23, 2014
Publisher	AIP Publishing LLC
Publication	Journal of Rheology
Article Title	Wormlike micellar solutions: II. Comparison between experimental data and scission model predictions
Author	C. J. Pipe,N. J. Kim,P. A. Vasquez, et al.
Online Publication Date	Jul 7, 2010
Volume number	54
Issue number	4
Type of Use	Thesis/Dissertation
Requestor type	Student
Format	Print and electronic
Portion	Figure/Table
Number of figures/tables	1
Title of your thesis / dissertation	Mathematical Modeling and Stochastic Simulation of Soft Materials
Expected completion date	Dec 2014
Estimated size (number of pages)	120
Total	0.00 USD

Terms and Conditions

The Society of Rheology -- Terms and Conditions: Permissions Uses

The Society of Rheology ("SOR") hereby grants to you the non-exclusive right and license to use and/or distribute the Material according to the use specified in your order, on a one-time basis, for the specified term, with a maximum distribution equal to the number that you have ordered.

Any links or other content accompanying the Material are not the subject of this license.

1. You agree to include the following copyright and permission notice with the reproduction of the Material: "Reprinted with permission from [FULL CITATION]. Copyright [PUBLICATION YEAR], The Society of Rheology." For an article, the copyright and permission notice must be printed on the first page of the article or book chapter. For photographs, covers, or tables, the copyright and permission notice may appear with the Material, in a footnote, or in the reference list.
2. If you have licensed reuse of a figure, photograph, cover, or table, it is your responsibility to ensure that the material is original to SOR and does not contain the copyright of another entity, and that the copyright notice of the figure, photograph, cover, or table does not indicate that it was reprinted by SOR, with permission, from another source. Under no circumstances does SOR, purport or intend to grant permission to reuse material to which it does not hold copyright.
3. You may not alter or modify the Material in any manner. You may translate the Material into another language only if you have licensed translation rights. You may not use the Material for promotional purposes. SOR reserves all rights not specifically granted herein.
4. The foregoing license shall not take effect unless and until SOR or its agent, Copyright Clearance Center, receives the Payment in accordance with Copyright Clearance Center Billing and Payment Terms and Conditions, which are incorporated herein by reference.
5. SOR or the Copyright Clearance Center may, within two business days of granting this license, revoke the license for any reason whatsoever, with a full refund payable to you. Should you violate the terms of this license at any time, SOR, The Society of Rheology, or Copyright Clearance Center may revoke the license with no refund to you. Notice of such revocation will be made using the contact information provided by you. Failure to receive such notice will not nullify the revocation.
6. SOR makes no representations or warranties with respect to the Material. You agree to indemnify and hold harmless SOR, The Society of Rheology, and their officers, directors, employees or agents from and against any and all claims arising out of your use of the Material other than as specifically authorized herein.
7. The permission granted herein is personal to you and is not transferable or assignable without the prior written permission of SOR. This license may not be amended except in a writing signed by the party to be charged.
8. If purchase orders, acknowledgments or check endorsements are issued on any forms containing terms and conditions which are inconsistent with these provisions, such inconsistent terms and conditions shall be of no force and effect. This document, including the CCC Billing and Payment Terms and Conditions, shall be the entire agreement between the parties relating to the subject matter hereof.

This Agreement shall be governed by and construed in accordance with the laws of the State of New York. Both parties hereby submit to the jurisdiction of the courts of New York County for purposes of resolving any disputes that may arise hereunder.

Questions? customercare@copyright.com or +1-855-239-3415 (toll free in the US) or +1-978-646-2777.

Gratis licenses (referencing \$0 in the Total field) are free. Please retain this printable license for your reference. No payment is required.

**ROYAL SOCIETY OF CHEMISTRY LICENSE
TERMS AND CONDITIONS**

Dec 07, 2014

This is a License Agreement between YUN ZENG ("You") and Royal Society of Chemistry ("Royal Society of Chemistry") provided by Copyright Clearance Center ("CCC"). The license consists of your order details, the terms and conditions provided by Royal Society of Chemistry, and the payment terms and conditions.

All payments must be made in full to CCC. For payment instructions, please see information listed at the bottom of this form.

License Number	3495070003521
License date	Oct 23, 2014
Licensed content publisher	Royal Society of Chemistry
Licensed content publication	Soft Matter
Licensed content title	The conundrum of gel formation by molecular nanofibers, wormlike micelles, and filamentous proteins: gelation without cross-links?
Licensed content author	Srinivasa R. Raghavan, Jack F. Douglas
Licensed content date	Jun 14, 2012
Volume number	8
Issue number	33
Type of Use	Thesis/Dissertation
Requestor type	academic/educational
Portion	figures/tables/images
Number of figures/tables /images	1
Format	print and electronic
Distribution quantity	6
Will you be translating?	no
Order reference number	None
Title of the thesis/dissertation	Mathematical Modeling and Stochastic Simulation of Soft Materials
Expected completion date	Dec 2014
Estimated size	120
Total	0.00 USD
Terms and Conditions	

This License Agreement is between {Requestor Name} ("You") and The Royal Society of Chemistry ("RSC") provided by the Copyright Clearance Center ("CCC"). The license consists of your order details, the terms and conditions provided by the Royal Society of Chemistry, and the payment terms and conditions.

RSC / TERMS AND CONDITIONS

INTRODUCTION

The publisher for this copyrighted material is The Royal Society of Chemistry. By clicking "accept" in connection with completing this licensing transaction, you agree that the following terms and conditions apply to this transaction (along with the Billing and Payment terms and conditions established by CCC, at the time that you opened your RightsLink account and that are available at any time at .

LICENSE GRANTED

The RSC hereby grants you a non-exclusive license to use the aforementioned material anywhere in the world subject to the terms and conditions indicated herein. Reproduction of the material is confined to the purpose and/or media for which permission is hereby given.

RESERVATION OF RIGHTS

The RSC reserves all rights not specifically granted in the combination of (i) the license details provided by you and accepted in the course of this licensing transaction; (ii) these terms and conditions; and (iii) CCC's Billing and Payment terms and conditions.

REVOCAION

The RSC reserves the right to revoke this license for any reason, including, but not limited to, advertising and promotional uses of RSC content, third party usage, and incorrect source figure attribution.

THIRD-PARTY MATERIAL DISCLAIMER

If part of the material to be used (for example, a figure) has appeared in the RSC publication with credit to another source, permission must also be sought from that source. If the other source is another RSC publication these details should be included in your RightsLink request. If the other source is a third party, permission must be obtained from the third party. The RSC disclaims any responsibility for the reproduction you make of items owned by a third party.

PAYMENT OF FEE

If the permission fee for the requested material is waived in this instance, please be advised that any future requests for the reproduction of RSC materials may attract a fee.

ACKNOWLEDGEMENT

The reproduction of the licensed material must be accompanied by the following acknowledgement:

Reproduced ("Adapted" or "in part") from {Reference Citation} (or Ref XX) with permission of The Royal Society of Chemistry.

If the licensed material is being reproduced from New Journal of Chemistry (NJC), Photochemical & Photobiological Sciences (PPS) or Physical Chemistry Chemical Physics (PCCP) you must include one of the following acknowledgements:

For figures originally published in NJC:

Reproduced (“Adapted” or “in part”) from {Reference Citation} (or Ref XX) with permission of The Royal Society of Chemistry (RSC) on behalf of the European Society for Photobiology, the European Photochemistry Association and the RSC.

For figures originally published in PPS:

Reproduced (“Adapted” or “in part”) from {Reference Citation} (or Ref XX) with permission of The Royal Society of Chemistry (RSC) on behalf of the Centre National de la Recherche Scientifique (CNRS) and the RSC.

For figures originally published in PCCP:

Reproduced (“Adapted” or “in part”) from {Reference Citation} (or Ref XX) with permission of the PCCP Owner Societies.

HYPERTEXT LINKS

With any material which is being reproduced in electronic form, you must include a hypertext link to the original RSC article on the RSC’s website. The recommended form for the hyperlink is <http://dx.doi.org/10.1039/DOI> suffix, for example in the link <http://dx.doi.org/10.1039/b110420a> the DOI suffix is ‘b110420a’. To find the relevant DOI suffix for the RSC article in question, go to the Journals section of the website and locate the article in the list of papers for the volume and issue of your specific journal. You will find the DOI suffix quoted there.

LICENSE CONTINGENT ON PAYMENT

While you may exercise the rights licensed immediately upon issuance of the license at the end of the licensing process for the transaction, provided that you have disclosed complete and accurate details of your proposed use, no license is finally effective unless and until full payment is received from you (by CCC) as provided in CCC's Billing and Payment terms and conditions. If full payment is not received on a timely basis, then any license preliminarily granted shall be deemed automatically revoked and shall be void as if never granted. Further, in the event that you breach any of these terms and conditions or any of CCC's Billing and Payment terms and conditions, the license is automatically revoked and shall be void as if never granted. Use of materials as described in a revoked license, as well as any use of the materials beyond the scope of an unrevoked license, may constitute copyright infringement and the RSC reserves the right to take any and all action to protect its copyright in the materials.

WARRANTIES

The RSC makes no representations or warranties with respect to the licensed material.

INDEMNITY

You hereby indemnify and agree to hold harmless the RSC and the CCC, and their respective officers, directors, trustees, employees and agents, from and against any and all claims arising out of your use of the licensed material other than as specifically authorized pursuant to this licence.

NO TRANSFER OF LICENSE

This license is personal to you or your publisher and may not be sublicensed, assigned, or transferred by you to any other person without the RSC's written permission.

NO AMENDMENT EXCEPT IN WRITING

This license may not be amended except in a writing signed by both parties (or, in the case of "Other Conditions, v1.2", by CCC on the RSC's behalf).

OBJECTION TO CONTRARY TERMS

You hereby acknowledge and agree that these terms and conditions, together with CCC's Billing and Payment terms and conditions (which are incorporated herein), comprise the entire agreement between you and the RSC (and CCC) concerning this licensing transaction, to the exclusion of all other terms and conditions, written or verbal, express or implied (including any terms contained in any purchase order, acknowledgment, check endorsement or other writing prepared by you). In the event of any conflict between your obligations established by these terms and conditions and those established by CCC's Billing and Payment terms and conditions, these terms and conditions shall control.

JURISDICTION

This license transaction shall be governed by and construed in accordance with the laws of the District of Columbia. You hereby agree to submit to the jurisdiction of the courts located in the District of Columbia for purposes of resolving any disputes that may arise in connection with this licensing transaction.

LIMITED LICENSE

The following terms and conditions apply to specific license types:

Translation

This permission is granted for non-exclusive world English rights only unless your license was granted for translation rights. If you licensed translation rights you may only translate this content into the languages you requested. A professional translator must perform all translations and reproduce the content word for word preserving the integrity of the article.

Intranet

If the licensed material is being posted on an Intranet, the Intranet is to be password-protected and made available only to bona fide students or employees only. All content posted to the Intranet must maintain the copyright information line on the bottom of each image. You must also fully reference the material and include a hypertext link as specified above.

Copies of Whole Articles

All copies of whole articles must maintain, if available, the copyright information line on the bottom of each page.

Other Conditions

v1.2

Gratis licenses (referencing \$0 in the Total field) are free. Please retain this printable license for your reference. No payment is required.

If you would like to pay for this license now, please remit this license along with your payment made payable to "COPYRIGHT CLEARANCE CENTER" otherwise you will be invoiced within 48 hours of the license date. Payment should be in the form of a check or money order referencing your account number and this invoice number {Invoice Number}.

Once you receive your invoice for this order, you may pay your invoice by credit card.

Please follow instructions provided at that time.

Make Payment To:

Copyright Clearance Center
Dept 001
P.O. Box 843006
Boston, MA 02284-3006

For suggestions or comments regarding this order, contact Rightslink Customer Support: customercare@copyright.com or +1-855-239-3415 (toll free in the US) or +1-978-646-2777.

Questions? customercare@copyright.com or +1-855-239-3415 (toll free in the US) or +1-978-646-2777.

Gratis licenses (referencing \$0 in the Total field) are free. Please retain this printable license for your reference. No payment is required.
